UNIVERSITY OF SOUTHAMPTON

Efficient High Harmonic Generation Sources for Applications in X-Ray Imaging

by

Charlie Pooley

A thesis submitted in partial fulfillment for the degree of Doctor of Philosophy

in the

Faculty of Physical Sciences and Engineering

Optoelectronics Research Centre

October 2021

UNIVERSITY OF SOUTHAMPTON

ABSTRACT

FACULTY OF PHYSICAL SCIENCES AND ENGINEERING
OPTOELECTRONICS RESEARCH CENTRE

Doctor of Philosophy

by Charlie Pooley

The observation of structures on small scales is useful for a range of applications, particularly in biological studies where higher resolution images allow examination of more intricate organic architectures. The development of coherent, high brightness sources at short wavelengths has driven a range of lensless imaging techniques that have been implemented successfully and pushed the resolution limit. However, such sources tend to be only available at large-scale, multi-user facilities. High harmonic generation (HHG) allows spatially coherent, short wavelength radiation to be available on a table-top set up, but with low beam stability due to the nonlinearity of the process.

The work in this thesis focuses on characterization and optimization of a HHG source at 29 nm (42 eV) specifically for use in coherent, lensless imaging. A model of the EUV beam is used to guide experimental efforts to empirically find the phase matching conditions for which the spatial coherence and flux properties are maximized whilst carefully controlling the source position and intensity stability. The resulting illumination is then put to the test in ptychographic imaging, where quantitative information about biological samples is obtained at an effective transverse resolution of 80 nm and axial sensitivity of 1 nm, with no observed radiation damage.

Finally, the images obtained with EUV ptychography are correlated with wide field and super resolution fluorescence images of the same sample region to provide direct comparison of our technique with more standard microscopy methods. A clear improvement in both resolution and contrast is observed. The fluorescence markers add information about sample composition that verifies our sample thickness measurements, and the object structure comparison motivates the use of EUV ptychography to complement fluorescence microscopy and assist in interpretation of features in the image.

Declaration of Authorship

I declare that this thesis and the work presented in it is my own. I confirm that:

1. This work was done wholly or mainly while in candidature for a research degree at this university
2. Where any part of this thesis has previously been submitted for a degree or any other qualification at this university or any other institution, this has been clearly stated
3. Where I have consulted the work of others, this is always clearly attributed
4. Where I have quoted from the work of others, the source is always given. With the exception of such quotations, this thesis is entirely my own work
5. I have acknowledged all main sources of help
6. Where the thesis is based on work done by myself jointly with others, I have made clear exactly what was done by others and what I have contributed myself

Signed: _____

Date: _____

Acknowledgements

I would like to thank my supervisors, in particular Dr Bill Brocklesby for continued encouragement and support throughout the project.

I would like to recognize everyone from the ultrafast x-ray group for being very easy to work with, in particular Dr Magdalena Miszczak for initial guidance and motivation when I was learning to work in the lab.

Thanks to Dr Peter Baksh and Dr Michal Odstrcil for continued advice in experimental and theoretical work as well as technical support long after moving on from the group.

Finally, special thanks to my colleague Haoyan Lu, for moral support, stimulating conversations and unfailing positivity even in the face of experimental catastrophe.

Contents

List of Figures

Chapter 1

Introduction

The ability to observe small scale structures is an extremely useful tool in a wide range of applications. This is particularly apparent in the field of biology; since the invention of the microscope in the 16th century new imaging techniques have routinely opened up new opportunities for biologists to visualize microscopic mechanisms and describe them more accurately. More recent advances have allowed further improvements in image quality, though every technique has its limitations.

Electron based techniques can provide sub-Ångstrom resolution, but can only image very thin samples or surfaces and require intense sample preparation and cryo-cooling. X-ray imaging allows for very high resolution due to short wavelengths, as well as depth of view to observe thick structures as a result of high sample penetration, though radiation damage can limit contrast and resolution if lower radiation doses must be used, and there is a lack of availability of usable optics. Super-resolution imaging allows inspection of objects smaller than allowed by the ordinary diffraction limit and can maintain a high depth of view; this is often beneficial for systems using optical illumination or fluorescence by chemical markers. However, these techniques cannot match the resolution capabilities of x-ray and electron imaging.

The development of high brightness, coherent sources at extreme ultraviolet and x-ray wavelengths has allowed lensless techniques to be implemented successfully, which provide unique advantages - no lens aberrations, a transverse resolution that is limited only by collection numerical aperture rather than focal spot or detector pixel size, and determination of the full electric field at the sample rather than intensity information alone. The cost of these advantages is a stringent set of requirements for the source coherence and stability to ensure the algorithms that recover the field will converge on an accurate solution.

Typically, short wavelength, coherent sources with high brightness and stability are only available at large-scale facilities such as synchrotrons and free electron lasers. However,

coherent soft x-ray and extreme ultraviolet sources are achievable using high harmonic generation. This highly nonlinear process requires high input intensity, but this may be reached with a femtosecond laser system that can be accommodated on a table-top set up in a standard lab, greatly increasing the accessibility of the source.

Though a high harmonic source is capable of meeting the spatial coherence requirement of a lensless imaging experiment, the extreme nonlinear nature of the process tends to greatly reduce the stability of the output, limiting the quality of the final image and potentially preventing the algorithm from finding a solution. Producing a functional lensless microscope using a high harmonic source means attacking the problem from two directions; the systematic errors during the data collection procedure must be reduced as much as possible, and the reconstruction algorithms must be sophisticated enough to correct any errors that can't be removed practically.

The aim of this project is to develop an efficient and coherent source of extreme ultraviolet radiation using high harmonic generation, which will then be tested by use in lensless imaging of biological samples. The resulting images will be compared with those obtained by other methods to show the effectiveness of imaging in this spectral region and its potential impact on other research.

In chapter 2, I will lay out the theory of high harmonic generation, from the simpler nonlinear process of second harmonic generation to a full picture of the high harmonic process, with a discussion of phase matching for maximizing flux and coherence, both being crucial components for a lensless imaging source.

In chapter 3, I will provide the background needed to understand the principles of different imaging techniques, from optical, fluorescence and super-resolution methods to coherent techniques, including the theory of electromagnetic propagation required for lensless algorithms. I will also give a brief account of some other imaging methods and their uses.

Chapter 4 will contain details of how the source was developed and characterized, from the femtosecond infrared laser input to the extreme ultraviolet output, with the emphasis on improving flux, spatial coherence and stability to optimize its use in imaging experiments.

Chapter 5 will give an account of the imaging experiments performed with the high harmonic source, with estimates of transverse and axial resolution and comparison with other imaging techniques used to look at the same sample regions.

Finally, chapter 6 will summarize our conclusions and provide an outlook for the future of the project.

1.1 Motivation

Visible wavelength microscopy has been a tool used by scientists for centuries, and x-ray microscopy has been a subject of inquiry for many decades. However, the use of extreme ultraviolet radiation as an illumination is a much more recent approach for imaging techniques. Since the first demonstrations of high harmonic generation [1, 2, 3], the possibility of a short wavelength coherent source that can fit on a standard lab bench has driven the development of sources of this type, as well as the state-of-the-art algorithms required for lensless imaging.

The first demonstration of lensless diffractive imaging using a source of this type reconstructed an image of a masked Carbon film with a spatial resolution of 214 nm using an illumination wavelength of 29 nm [4]. A number of studies since have shown significant improvements in the source and reconstruction algorithms, with the possibility of reflection geometry [5, 6, 7], 3D imaging and resolution down to 12 nm [8]. However, until recently, images taken with coherent table-top set-ups in the extreme ultraviolet regime have required fabricated samples with strong scattering to ensure successful reconstructions. Recent developments of the source and the algorithm, in particular increased coherence and stability as well as introduction of methods that can better handle source instability in post processing [9], have allowed reconstructions of real, weakly scattering biological samples with diffraction limited resolution of 80 nm [10]. This has increased the applicability of high harmonic sources to biological applications, and stimulated a motivation for further study.

Many other imaging methods are already well established and widely used in a variety of fields. Electron microscopes allow far better resolution than any microscope operating in the extreme ultraviolet due to far shorter wavelength illumination; transmission electron microscopes can provide sub-Ångstrom resolution for some samples [11]. Likewise, hard x-ray sources provide a better theoretical limit for resolution. Developments in super resolution fluorescence imaging, which is particularly popular for biological samples, have allowed details down to 10 nm to be resolved [12], which is comparable to the lowest resolution demonstrated using high harmonic sources.

However, coherent imaging in the extreme ultraviolet offers some unique advantages over other methods. Lensless imaging does not depend on the quality of any optics between the object and the camera, which means the final image is free of aberrations. Also, the final reconstruction contains amplitude and phase information about the sample, which is related to the thickness and composition. The final resolution is limited only by collection numerical aperture, and is not related to focal spot or the pixel size of the detector. Extreme ultraviolet radiation has a better penetration depth than electrons to probe beyond the sample surface, but is more strongly absorbed than hard x-rays, which allows far better image contrast with no sample damage [13]. Lastly, unlike super resolution fluorescence methods, coherent imaging does not require the addition

of fluorescent markers to produce an image, the use of which makes sample preparation more difficult, imposes a lifetime on the samples over which they may be imaged before bleaching occurs, and can be the cause of poor signal-to-noise ratio reducing imaging quality, particularly for thin specimens.

The primary goal of this project is to develop a table-top, coherent, extreme ultraviolet source specifically for use in coherent imaging by maximizing the coherence and stability. The resulting radiation will then be used as an illumination for coherent imaging experiments, with a particular focus on biological samples, to utilize the advantages of both lensless imaging and extreme ultraviolet illumination. The ultimate aim is to move this technique from a proof-of-concept to a useful microscope providing additional information about the sample, which may be used to compliment other techniques via correlative imaging.

Chapter 2

High Harmonic Generation

2.1 Introduction to Nonlinear Optics

When an electric field is incident on some medium, it induces a polarization response which generates its own electric field. Usually this is a first order effect whereby the response is directly proportional to the field amplitude; this generates a field at the same frequency with some delay, which when combined with the original wave determines the phase velocity of the propagation. However, particularly for strong input fields, higher orders in the response can be realized, resulting in the possibility of energy exchange to a number of higher frequencies. This is useful for applications in a number of areas [14].

2.1.1 Second Harmonic Generation

The polarization $\boldsymbol{P}$ of a material in which an electric field $\boldsymbol{E}$ is propagating can be written as an expansion [15]:

$$\boldsymbol{P} = \epsilon_0 \left(\chi^{(1)} \boldsymbol{E} + \chi^{(2)} \boldsymbol{E}^2 + \chi^{(3)} \boldsymbol{E}^3 + \cdots \right) \tag{2.1}$$

where ϵ_0 is the permittivity of free space and $\chi^{(n)}$ are the optical susceptibility tensors, which depend on the material. Here all nonlinear terms are considered as a perturbation with a comparatively small contribution to the polarization, which is valid provided the input field is weak compared to the atomic potential - this approach cannot be used to describe more extreme nonlinear phenomena such as high harmonic generation, as is discussed in section 2.2.

However, it may be used to describe second harmonic generation (SHG) for the class of noncentrosymmetric crystals that exhibit a strong term in the second order susceptibility. In this case, conversion efficiency depends on the strength of the nonlinearity,

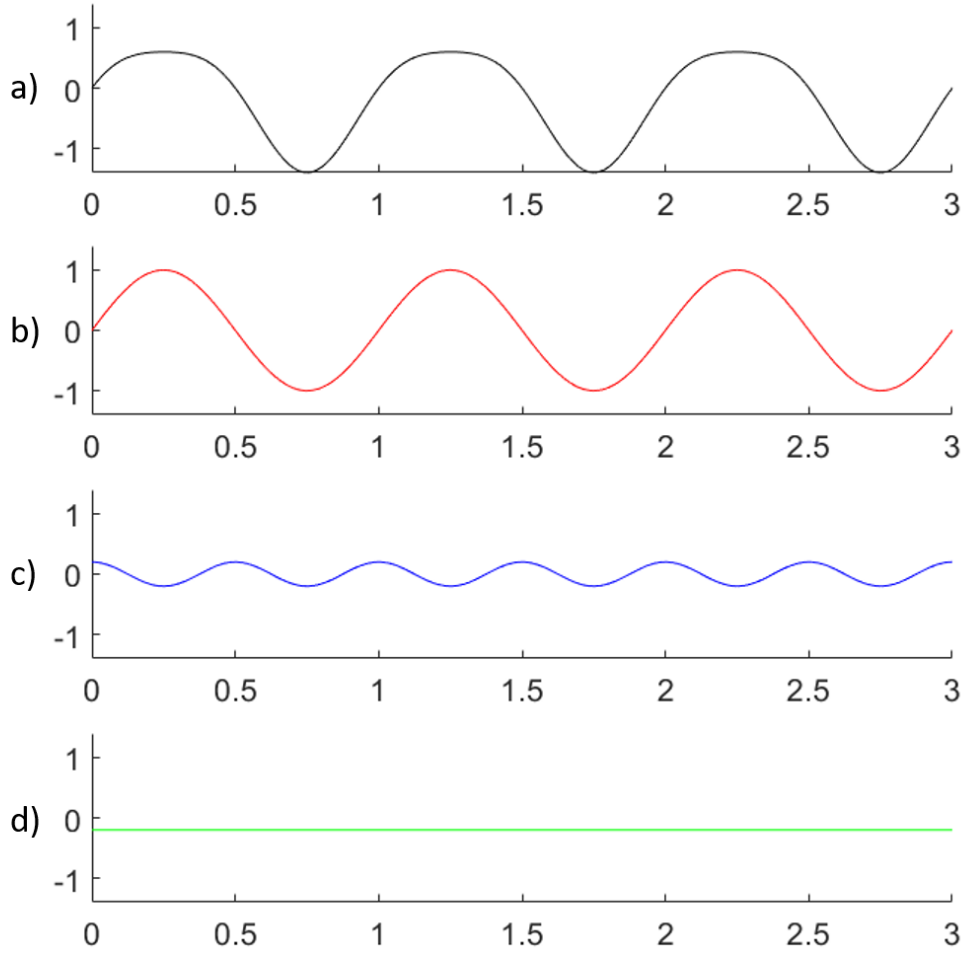

FIGURE 2.1: A nonlinear polarization (a) broken into its various frequency components; a first order component (b) of equal frequency to the driving field, a second harmonic component (c) and an average DC component (d)

and crucially on the phase matching condition between the fundamental and second harmonic wave vectors,

$$\Delta \boldsymbol{k} = \boldsymbol{k}^{2\omega} - 2\boldsymbol{k}^{\omega} = 0 \tag{2.2}$$

such that the generated light interferes constructively with the propagating second harmonic. Provided the two beams are co-linear, this is equivalent to matching the refractive indices, $n^{2\omega} = n^{\omega}$, which may be achieved by selecting a particular propagation angle if the crystal is birefringent (critical phase matching) or by choosing a temperature for which this criterion is met for the crystal that is used (noncritical phase matching). Figure 2.1 illustrates how a non-centrosymmetric crystal driven by an external field can exhibit a polarization response with a component at twice the frequency; this is a simple

demonstration of how higher order harmonics can be generated by a response to a single frequency excitation.

For a beam with negligible depletion propagating a length L in a crystal, the conversion efficiency follows a sinc^2 relationship in ΔkL, and quadratic in L:

$$\frac{P^{2\omega}}{P^{\omega}} \propto L^2 \cdot \frac{\sin^2\left(\frac{\Delta kL}{2}\right)}{\left(\frac{\Delta kL}{2}\right)^2} \tag{2.3}$$

The effect of this relationship is shown in figure 2.2, where for a given crystal length the wave vector mismatch $\Delta\boldsymbol{k}$ reduces the second harmonic intensity sharply, and in figure 2.3 where a given $\Delta\boldsymbol{k}$ causes a reduction in conversion efficiency after some propagation length. The fringe separation here gives rise to a coherence length $L_c = \frac{2\pi}{\Delta k}$, or equivalently

$$L_c = \frac{\lambda}{n^{\omega} - n^{2\omega}} \tag{2.4}$$

which determines the maximum useful crystal length for SHG.

2.1.2 Ultrafast Effects

Since the second harmonic term in the polarization depends on the square of the electric field, the conversion efficiency of the process increases linearly with power until the input beam is significantly depleted; this means pulsed sources allow for much higher efficiencies. However, a small delay between the input and second harmonic pulse can mean they no longer overlap in time. The increasing temporal walk-off as one pulse lags behind the other creates an output that is stretched in time. The group velocity mismatch is given by

$$\text{GVM} = \left| \frac{1}{v_{g1}} - \frac{1}{v_{g2}} \right| \tag{2.5}$$

This tells us the time difference per propagation length between the two pulse peaks, and imposes a new restriction on the maximum crystal length to prevent unwanted lengthening effects:

$$L_{\max} = \frac{\tau_p}{\text{GVM}} \tag{2.6}$$

which is the length of propagation in the crystal for which the pulses are separated by one input pulse length τ_p. Very thin crystals are often used to reduce this issue; around

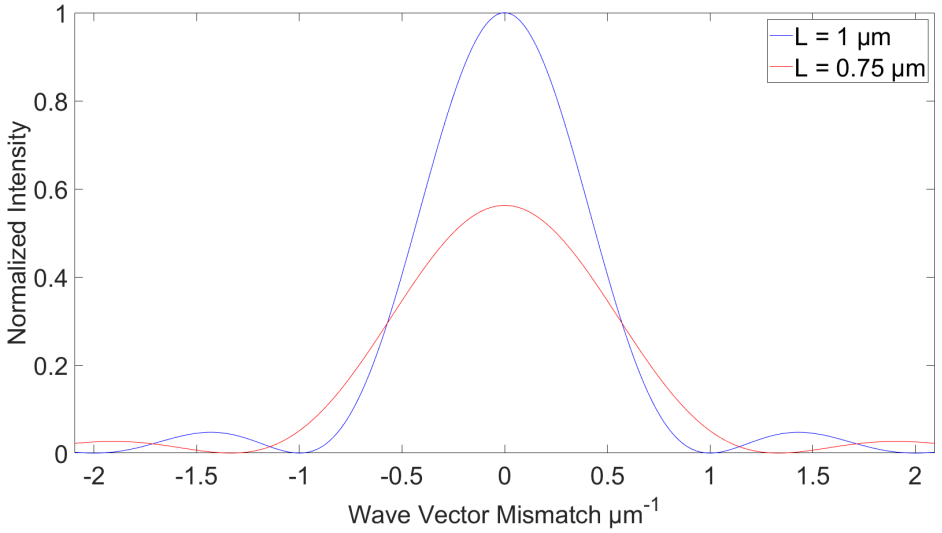

FIGURE 2.2: Normalized intensity vs wave vector mismatch for two different propagation lengths through a crystal. This shows the critical role of phase matching in second harmonic generation.

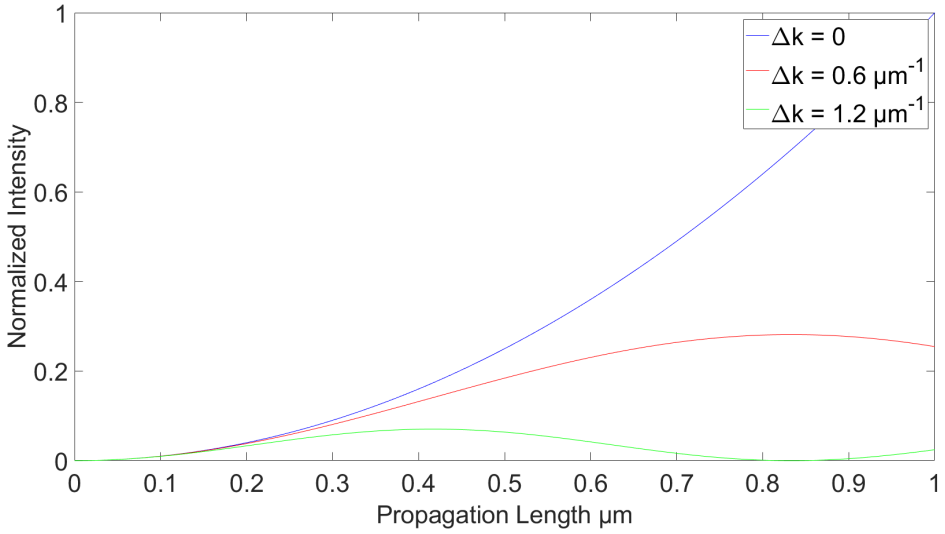

FIGURE 2.3: Normalized intensity vs propagation length through a crystal for three different wave vector mismatch values. Here we see that using a thicker crystal may be counterproductive if the phase matching condition is not satisfied.

100 µm thickness is common. Of course, the pulses are also stretched by dispersion due to the wavelength dependence on refractive index for most materials, though this may be corrected for after generation to re-compress the pulse.

2.2 High Harmonic Generation

High harmonic generation (HHG) [2, 3] is a highly nonlinear optical process with uses in a number of applications [16]. Extreme input intensities are required, on the order of 10^{14} W/cm^2. In this regime, the higher order terms in the atomic polarization from 2.1 are no longer small, and the perturbation model used to understand SHG is no longer valid; a more careful consideration of electron dynamics is required.

2.2.1 The Three Step Model

The three step model [17] can be considered as an initial, naive approach to figure out the origin of high frequency components in HHG. This model relies heavily on classical mechanics, which clearly cannot give an accurate description of single electron dynamics at the atomic scale; a full quantum model is ultimately necessary. However, it provides a simple visualization of a highly complex process.

The three steps of the model are as follows:

1. The electron begins bound to the nucleus in the ground state, and tunnels at some time t_0 due to a distortion of the atomic potential by an incident laser field.
2. After tunneling, the electron dynamics are dominated by the laser and it accelerates as a free charge.
3. As the oscillating field changes direction, the electron may return and recombine with the nucleus at some time t_f, whereby a photon with energy equal to the ionization energy plus the additional kinetic energy is produced.

Here the processes involved during tunneling and recombination are completely ignored and instead the path taken by the electron during the second step is calculated by solving the equations of motion. First, the laser field is described by $E = -E_0 \cos \omega t$. Then the acceleration of the free electron after tunneling is

$$\ddot{x}(t) = \frac{eE_0}{m} \cos \omega t \tag{2.7}$$

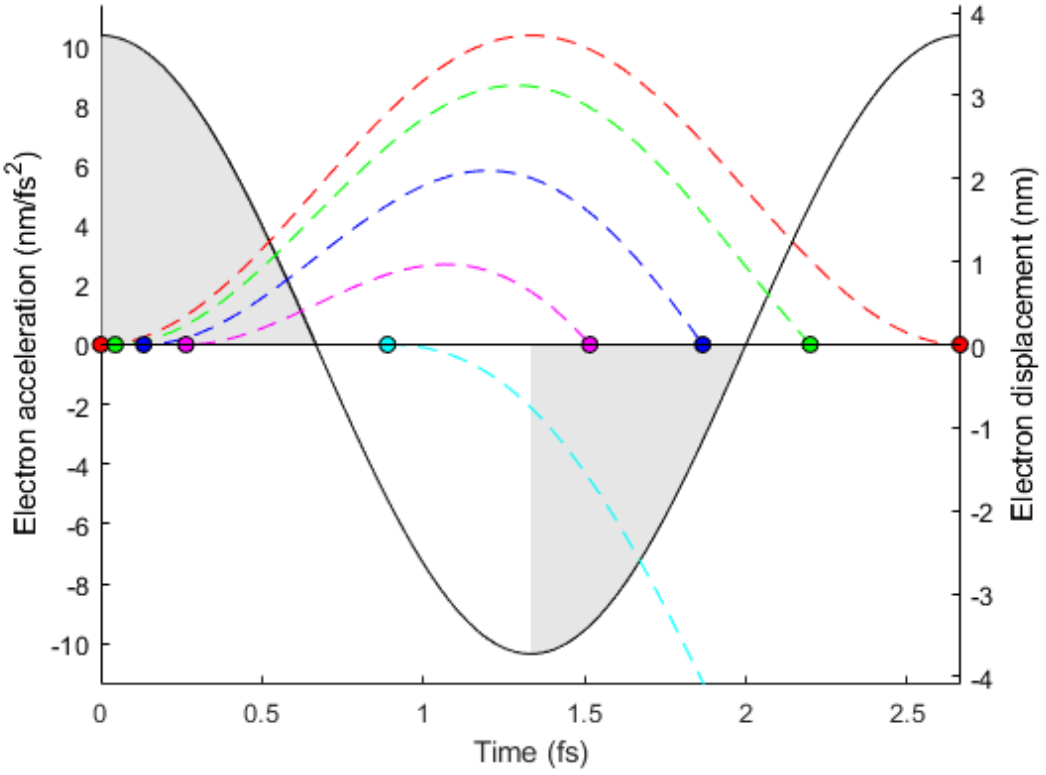

FIGURE 2.4: Some possible classical trajectories for electrons emitted at different values of t_0 as described by equation 2.9 (dashed lines; right y-axis) with acceleration described by equation 2.7 (solid black line) due to an intense laser field, plotted on the same time axis. The shaded regions indicate values of t_0 for which the electron will recombine with the atomic nucleus.

Assuming the electron starts at the nucleus with zero velocity at the tunneling time t_0, we can apply the initial condition $\dot{x}(t_0) = x(t_0) = 0$ to find the velocity and position by integrating:

$$\dot{x}(t, t_0) = \frac{eE_0}{m\omega} [\sin \omega t - \sin \omega t_0] \tag{2.8}$$

$$x(t, t_0) = \frac{eE_0}{m\omega^2} [\cos \omega t_0 - \cos \omega t + \omega(t_0 - t) \sin \omega t_0] \tag{2.9}$$

Some of the possible trajectories described by equation 2.9 are plotted in figure 2.4, where the different possible paths arise from different ionization times t_0, and several implications are quickly apparent.

Firstly, only electrons that tunnel during odd quarter cycles of the laser, indicated by the shaded regions, can provide radiation. This is because the electron will not return at other tunneling times; the cyan trajectory is one example. This suggests high harmonics will be emitted in bursts separated by half the laser period.

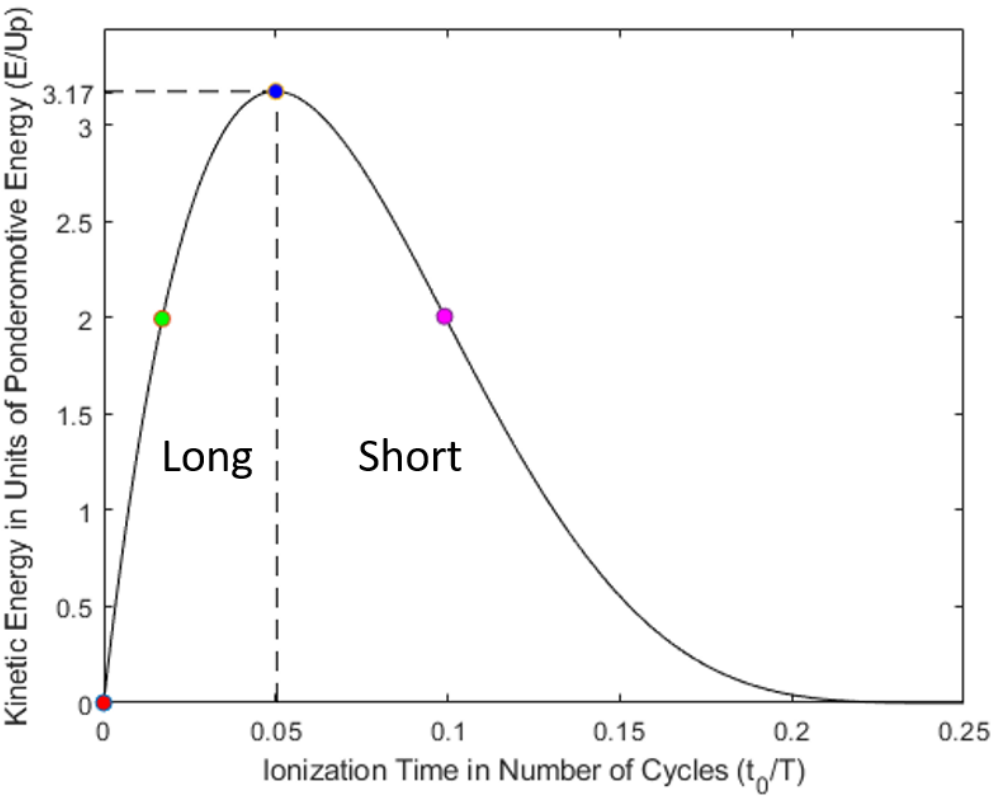

FIGURE 2.5: Kinetic energy of the returning electron as a function of ionization time for all possible values of t_0 within one quarter laser period. The coloured markers correspond to trajectories plotted with the same colour in figure 2.4.

Secondly, electrons ionized during successive quarter cycles will follow identical trajectories in the opposite direction, adding π to the phase of generated radiation. If the laser period is T, the relative phase between two consecutive bursts is $\delta\phi = \omega_g \frac{\mathrm{T}}{2} + \pi$, where ω_g is the generated frequency. For constructive interference, the phase difference should be some multiple of 2π; this applies to generated frequencies for which $\omega_g = \frac{2\pi}{\mathrm{T}}(2n-1)$. This tells us that HHG is only efficient for odd harmonics over many cycles.

Finally, the shape of the different paths in figure 2.4 suggest something about the photon energies that can be produced. For very small t_0, the electron begins to slow down before it recombines, and as t_0 approaches T/4, there is not much time to build speed. This implies an optimal t_0 that gives a trajectory with maximum kinetic energy on return. Furthermore, we can expect that every generated frequency (except the cutoff) will be produced by two electron paths; one long trajectory for electrons emitted before the optimal t_0, and one short trajectory for electrons emitted after.

The kinetic energy of a returning electron can be calculated using

$$\mathrm{K}_f = \frac{1}{2} m \dot{x}^2(t_f, t_0) \tag{2.10}$$

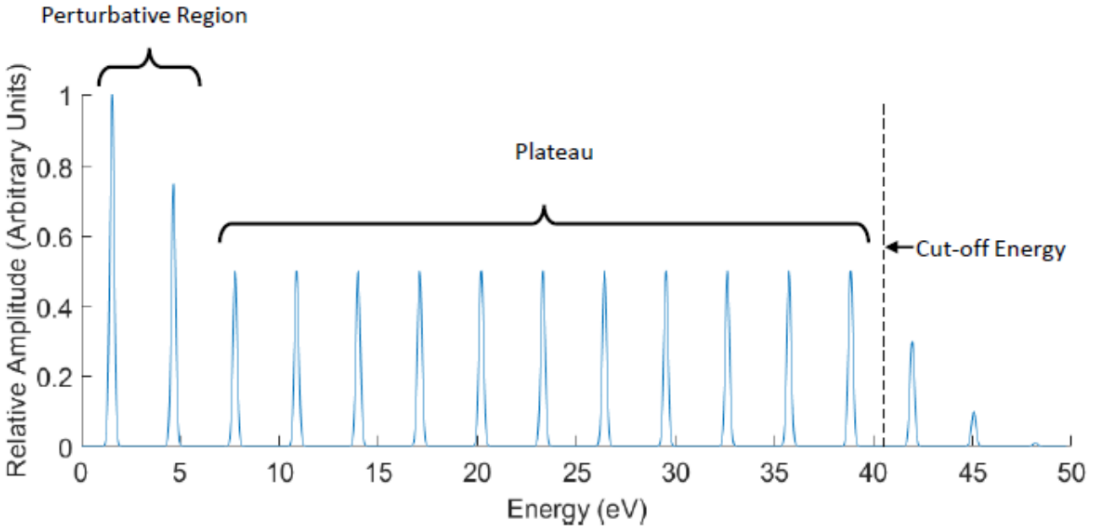

FIGURE 2.6: Representation of the shape of an HHG spectrum, indicating the perturbative region for low orders, the 'plateau' where successive harmonics have comparable amplitude, and the sharp decline after the cut-off energy.

where the values of t_0 and t_f are calculated for each trajectory. Figure 2.5 shows all possible values of return kinetic energy for an electron ionized during a single quarter cycle. Here it is clear that the optimal trajectory in figure 2.4 was the blue path, and the green and magenta markers are examples of long and short trajectories that produce the same photon energy. 2.5 gives energy in units of ponderomotive energy U_p

$$U_p = \frac{e^2 E_0^2}{4 m_e \omega_0^2} \tag{2.11}$$

where m_e is electron mass and ω_0 is the laser angular frequency. This is the average kinetic energy of an electron following simple harmonic motion in an oscillating field. It is now apparent that the maximum photon energy, or 'cut-off' [18], is

$$E_{co} \approx 3.17 U_p + I_p \tag{2.12}$$

where I_p is the atomic ionization potential.

These implications predict an output spectrum of odd harmonics, with a decreasing amplitude in the perturbative region, a 'plateau' of harmonics of comparable amplitude, and a sharp drop off after the cut-off energy; an idealized version of what this might look like is given in figure 2.6. In practice, the output varies greatly with the specifics of the laser system in use as well as the experimental geometry, but most harmonic spectra follow this characteristic shape.

2.2.2 A Quantum Model

Of course, to provide a more accurate description that follows a deeper understanding of these dynamics, a quantum model is required [19, 20]. Solving the time dependent Schrödinger equation (TDSE) numerically is one approach [21]. If we consider a strong laser field incident on a simple atom in one dimension, the TDSE for an electron is given by

$$i\hbar\frac{\partial\psi}{\partial t} = -\frac{\hbar^2}{2m_e}\frac{\partial^2\psi}{\partial x^2} + (V_{\text{Coulomb}} + V_{\text{Laser}})\psi \tag{2.13}$$

where $\hbar$ is the reduced Plank constant, ψ is the electron wave function, V_{Coulomb} is the static Coulomb potential due to the atomic nucleus and V_{Laser} is the contribution to potential from the oscillating laser field.

In this model, as the laser field increases, a small part of the electron wave function is swept away from the atom, which may then return to the core after the field reverses. The resulting interference between the returning tunnelled state and the ground state causes oscillations in the expectation of the electron position $\langle x\rangle$, which acts as an oscillating dipole generating an electric field proportional to acceleration a:

$$a(t) = \frac{d^2}{dt^2}\langle x\rangle \tag{2.14}$$

from which the field may be calculated.

2.2.3 Phase Matching

Similarly to SHG, the efficiency of generation of any given harmonic can be increased by matching the phase of the fundamental and high harmonic fields. The condition for the high harmonic case is given by

$$\Delta\boldsymbol{k} = \boldsymbol{k}_q - q\boldsymbol{k}_f = 0 \tag{2.15}$$

where $\boldsymbol{k}_q$ is the wave vector of the q^{th} harmonic and $\boldsymbol{k}_f$ is the fundamental wave vector. Here we can consider the various contributions to the phase of the fundamental and high harmonic waves in HHG.

2.2.3.1 Dispersion Effects

First, there will be some mismatch as a result of linear dispersion in the generation medium, which is caused by wavelength dependent refractive index. Typically the medium in HHG will be a gas, and the input pulse will necessarily cause some ionization over its duration; the effect of neutral gas atoms and plasma must both be considered. The contribution from neutral gas atoms to the wave vector mismatch is given by

$$\Delta k_{\text{gas}} = qp(1-\eta)\frac{2\pi}{\lambda_0}\delta n \tag{2.16}$$

where q is harmonic number, p is the gas pressure as a fraction of atmospheric pressure, η is the fraction of ionized gas particles, λ_0 is input laser wavelength and $\delta n = n_f - n_q$ is the difference between the refractive indices at the fundamental and high harmonic wavelengths. The effect of extreme intensity may also be considered by including the nonlinear refractive index n_2, such that the fundamental index is modified by $n_2 I$.

The contribution from free electrons can be calculated by considering plasma refractive index; for an input wave with angular frequency ω_0, the plasma index is given by

$$n_p = \sqrt{1 - \frac{\omega_p^2}{\omega_0^2}} \approx 1 - \frac{\omega_p^2}{2\omega_0^2} \tag{2.17}$$

where we have approximated with a Taylor expansion with the assumption that the fundamental frequency is fast compared to the plasma response ω_p, defined by

$$\omega_p = \sqrt{\frac{e^2 N_e}{m_e \epsilon_0}} \tag{2.18}$$

where e and m_e are electron charge and mass, ϵ_0 is permittivity of free space and N_e is the density of free electrons, which may be calculated from the ionization fraction η and neutral gas density N_g as $N_e = \eta N_g$. Putting these together,

$$\Delta k_{\text{electrons}} = -q\frac{\pi}{\lambda_0}\eta N_g \frac{e^2}{m_e \epsilon_0 \omega_0^2} \tag{2.19}$$

$$= -q\eta N_g r_e \lambda_0 \tag{2.20}$$

where r_e is the classical electron radius.

Since both of these phase contributions depend on number density of gas particles, the dispersion effects are much less significant in low pressure HHG set ups.

2.2.3.2 Geometric Effects

Getting a input laser intensity sufficient to generate high harmonics requires focusing, from which an additional phase shift arises. The solution most commonly used to approximate the field distribution for a laser is the Gaussian beam, which may be derived from Maxwell's equations with the assumptions that the field propagates mainly parallel to the z axis and that the shape of the envelope varies slowly on the scale of the wavelength. The solution for the electric field may be written as

$$E(r,z) = E_0 \frac{w_0}{w(z)} \exp\left[-\frac{r^2}{w^2(z)}\right] \exp\left[-\frac{ikr^2}{2R(z)}\right] \exp\left[i\phi_g(z)\right] \exp(-ikz) \tag{2.21}$$

where E_0 is the field amplitude, w is the beam waist defined as the radial distance after which the beam amplitude drops by a factor of $1/e$ (with a minimum value of w_0), R is the radius of curvature of the wavefronts, k is the fundamental wave vector, and ϕ_g is the Gouy phase shift that varies through the beam focus:

$$\phi_g = \tan^{-1}\left(\frac{z}{z_R}\right) \tag{2.22}$$

where $z_R = \frac{\pi w_0^2}{\lambda}$ is the Rayleigh length, defined as the distance of propagation from the focus before the cross sectional beam area doubles. We can then calculate the phase of the beam at any position relative to that of a perfect planar wave at the same frequency:

$$\Delta\mathbf{k}_{\text{geometric}} = \nabla\left(\frac{kr^2}{2R(z)} + \phi_g\right) \tag{2.23}$$

The contribution from just the Gouy phase shift is

$$\begin{aligned}\Delta k_g &= \frac{d\phi_g}{dz} \\ &= \frac{z_R}{z^2 + z_R^2}\end{aligned} \tag{2.24}$$

Given the dependence on the minimum spot size, this allows tuning of the phase matching conditions by choice of the focusing geometry [22], and optimization during an

experiment by aperturing the laser beam before the focusing optic [23, 24, 25]; though aperturing will also change the shape of the mode and the intensity.

2.2.3.3 Atomic Phase

The atomic phase in HHG is the additional phase shift acquired during the time between ionization and recombination causing the generated wave to lag behind the fundamental wave, and is given by [22]

$$\phi_{\text{atom}} = q\omega_0 t_f - \frac{1}{\hbar} S\left(p_{st}, t_0, t_f\right) \tag{2.25}$$

where S is the quasi-classical action at the stationary value of electron momentum $p = p_{st}$,

$$S\left(p, t_0, t_f\right) = \int_{t_0}^{t_f} \left(\frac{p^2(t)}{2m_e} + I_p\right) dt \tag{2.26}$$

and the resulting change to the wave vector can then be found:

$$\Delta\mathbf{k}_{\text{atom}} = \nabla\phi_{\text{atom}} \tag{2.27}$$

The quasi-classical action at this value is a valid approximation to the full quantum description since the only electron trajectories that give a significant contribution to the dipole moment of the atom are those for which the action is stationary [26]. In this case, the action can be approximated by

$$S \approx -(t_f - t_i)U_p \tag{2.28}$$

which, from the definition for U_p (equation 2.11), implies a phase shift that depends on the input laser intensity and frequency.

2.2.3.4 Full Picture

The phase matching considerations may now be combined to find the magnitude of the total wave vector mismatch between the fundamental and high harmonic fields at any location within the generation volume:

$$\left|\Delta\mathbf{k}\right| = k_q - \left|q\Big[\left(k_f + \Delta k_{\text{gas}} + \Delta k_{\text{electrons}}\right)\hat{\mathbf{z}} + \Delta\mathbf{k}_{\text{geometric}}\Big] + \Delta\mathbf{k}_{\text{atom}}\right| \tag{2.29}$$

We can now use this expression to calculate the coherence length $L_c = \frac{1}{|\Delta \mathbf{k}|}$ to map the phase matching efficiency. Since there are two distinct intervals within a single laser cycle during which electrons may recombine with the same energy defined by the long and short trajectories, there is a different atomic phase contribution for each. This results in very different outcome for the regions over which generation can build up efficiently, as shown in figure 2.7. This shows the coherence length in mm between the fundamental and 27^{th} harmonic within a cross sectional area of the input laser beam through the focus. Here the parameters have been chosen to mirror those used for the majority of the experimental work in this thesis; an 800 nm, 1.5 mJ input pulse at 40 fs duration, with a minimum beam waist of 60 µm in Argon gas. The black areas at the outer edge indicate where the intensity is not sufficient to generate photons at this energy, consistent with equation 2.12. The contributions of neutral gas atoms and free electrons to $|\Delta \mathbf{k}|$ have been ignored. This is reasonable since in our low pressure geometry, $\Delta k_{electrons}$ and Δk_{gas} are at least two orders of magnitude smaller than k_f, regardless of the ionization fraction η.

2.2.4 Coherence

For an electric field E, coherence is a measure of correlation between the field measured at two different positions or times. A precise definition is given by the degree of first order coherence:

$$g^{(1)}(\boldsymbol{r}_1, t_1; \boldsymbol{r}_2, t_2) = \frac{\langle E^*(\boldsymbol{r}_1, t_1) E(\boldsymbol{r}_2, t_2) \rangle}{\sqrt{\langle |E(\boldsymbol{r}_1, t_1)|^2 \rangle \langle |E(\boldsymbol{r}_2, t_2)|^2 \rangle}} \tag{2.30}$$

where $\boldsymbol{r}_i$ are position vectors and t_i are times, and $\langle\rangle$ denotes a time average. For a laser beam propagating almost entirely in one direction, the coherence tells us how predictable the interference effects will be. It is useful to separate this general property into spatial and temporal coherence.

Temporal (or longitudinal) coherence is the average correlation between the field at the same position at two different times. With this restriction, and introducing a delay time $\tau = t_1 - t_2$, equation 2.30 can be simplified to

$$g^{(1)}(\tau) = \frac{\langle E^*(t) E(t+\tau) \rangle}{\langle |E(t)|^2 \rangle} \tag{2.31}$$

A perfect monochromatic source will always perfectly correlate at any time delay, but in practice all sources have some finite bandwidth which causes decorrelation after some delay. The coherence time is a useful parameter to determine how temporally coherent a source of bandwidth $\Delta\omega$ is:

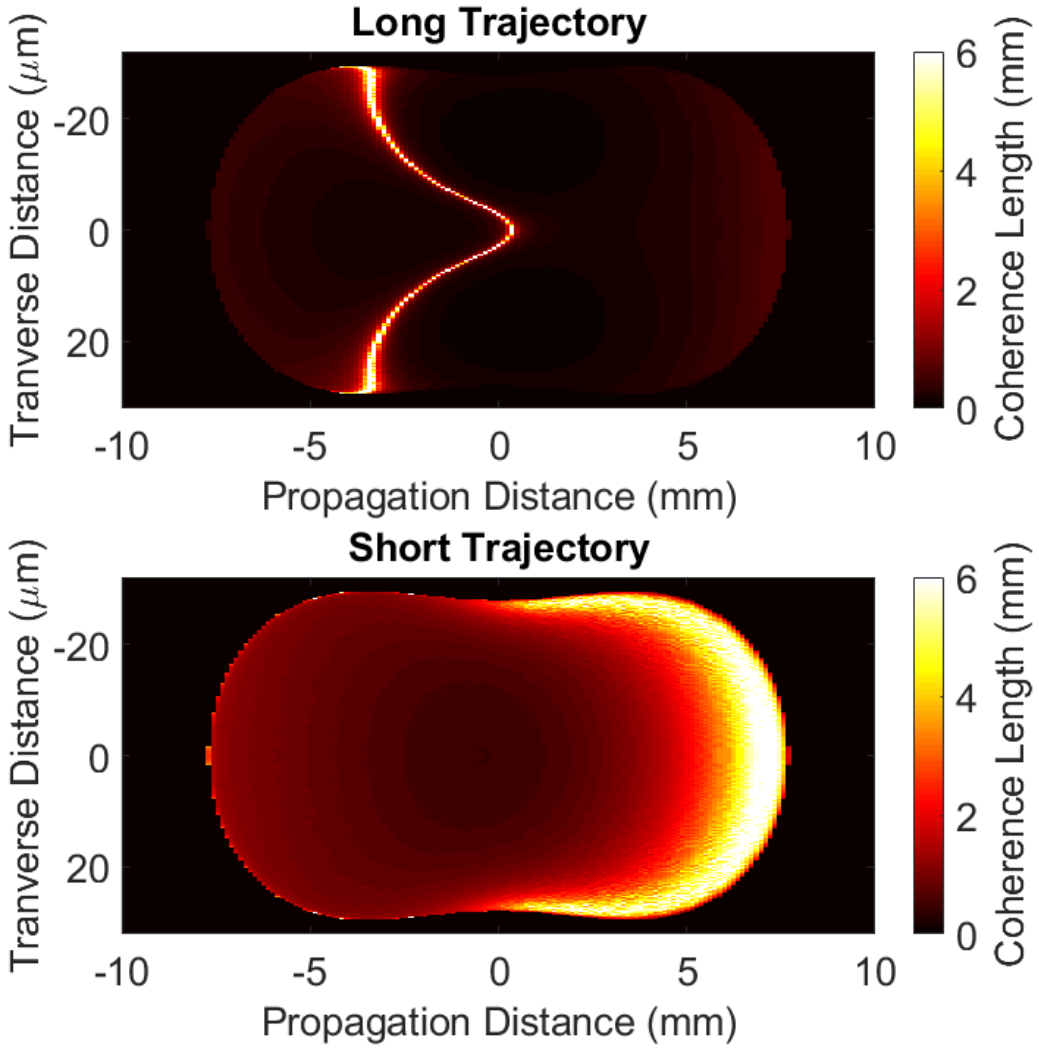

FIGURE 2.7: Coherence length in mm for long and short HHG trajectories at the 27^{th} harmonic for an 800 nm, 1.5 mJ input pulse with 40 fs duration focused to a minimum beam waist of 60 µm in Argon gas, selected to reflect the experimental parameters used for the majority of work in this Thesis.

$$t_c = \frac{1}{\Delta\omega} \tag{2.32}$$

This may be defined as the time after which two fields of frequency difference $\Delta\omega$ become 1 radian out of phase. Ultrashort pulses with a necessarily broad bandwidth have very short coherence time. This can also be expressed as a longitudinal coherence length, defined as the distance light travels during the coherence time:

$$L_c = \frac{ct_c}{\mathrm{n}} \tag{2.33}$$

where n is refractive index and c is the vacuum speed of light. This gives a length over which the field may be considered to be coherent.

Spatial (or transverse) coherence is the average correlation between the field measured at two positions across the beam profile at the same time. An ideal point source exhibits perfect spatial coherence since every point on the wave front is generated at the same time, so must correlate perfectly. In practice, lasers can exhibit high spatial coherence due to transverse resonator modes, and coherence can be improved by spatial filtering. For a wave propagating a distance z from a source of size d, the transverse coherence length is given by

$$L_t = \frac{z\lambda}{2\pi d} \tag{2.34}$$

A practical method for measuring coherence is by double slit interference, where the source is sampled at two transverse positions and combined to observe field correlation as in figure 2.8. A beam of peak intensity I_0 incident on a double slit will exhibit an intensity distribution in a plane a long way past the double slit

$$\mathrm{I} = \mathrm{I}_0 \cos^2\left(\frac{\phi_1}{2}\right) \mathrm{sinc}^2\left(\frac{\phi_2}{2}\right) \tag{2.35}$$

with

$$\phi_1 = \frac{2\pi dx}{z\lambda}$$

$$\phi_2 = \frac{2\pi ax}{z\lambda}$$

where we have used the small angle approximation $\tan(\theta) \approx \sin(\theta) = x/z$. By introducing a variable γ, we can modify equation 2.35 slightly to reflect the intensity from a partially coherent sum between fields from the two slits

$$\mathrm{I} = \frac{\mathrm{I}_0}{2}\left[1 + \gamma\cos\phi_1\right] \mathrm{sinc}^2\left(\frac{\phi_2}{2}\right) \tag{2.36}$$

where γ is the fringe visibility, which may also be determined from consecutive intensity maxima and minima:

$$\gamma = \frac{\mathrm{I}_{\max} - \mathrm{I}_{\min}}{\mathrm{I}_{\max} + \mathrm{I}_{\min}} \tag{2.37}$$

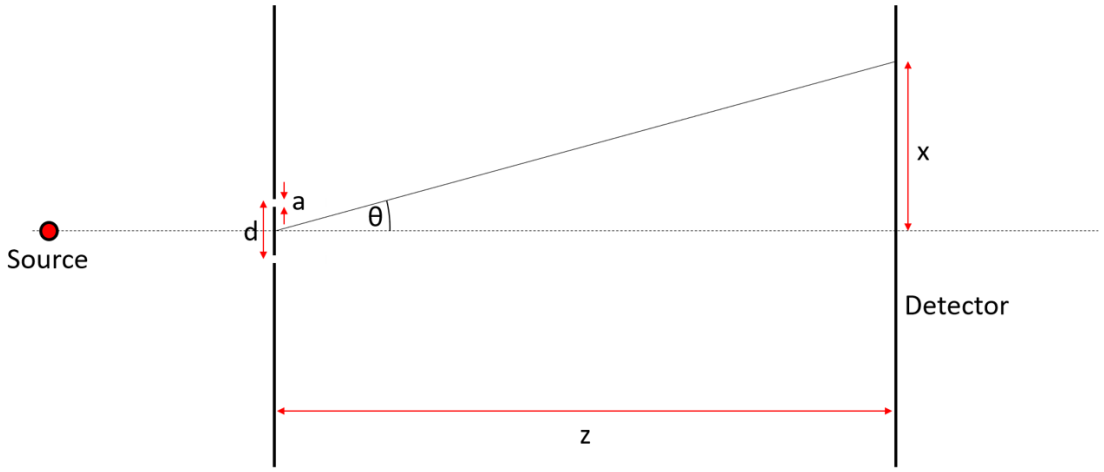

FIGURE 2.8: Basic set up for a two slit interference experiment.

allowing a straightforward experimental measurement which relates to the spatial coherence of a source. In fact, assuming that the intensity pattern comes from a mixture of coherent and incoherent sums from the fields E_1 and E_2 at the two slits, it can be shown that the visibility is the fraction of coherent intensity, i.e.

$$I \propto \gamma \left|E_1 + E_2\right|^2 + \alpha \left(|E_1|^2 + |E_2|^2\right) \tag{2.38}$$

with $\alpha+\gamma = 1$ The impact of these different types of coherence on the two slit diffraction pattern are shown in figure 2.9.

A full characterization of spatial coherence would require repeated measurements at a number of slit separations, but a single measurement can act as an indication of the source quality [27, 28].

2.2.4.1 Coherence in HHG

Since there are multiple frequencies produced by an HHG source, the temporal coherence is limited by the spectrum, which may be measured directly or determined via double slit measurements [29, 30]. This can be massively improved by spectral filtering to pick out a single harmonic, since the bandwidth of individual harmonics is typically very small, and is further reduced by using a longer pulse length of the input laser.

The spatial coherence of an HHG source is ultimately limited by the coherence of the driving laser, but also depends largely on the phase matching conditions [31]; the long and short trajectories can be considered as two independent sources that do not combine coherently, resulting in a competition between them that ultimately results in a loss of interference fringes. By optimizing a single trajectory and suppressing the other when phase matching, it is possible to improve the spatial coherence of the source at

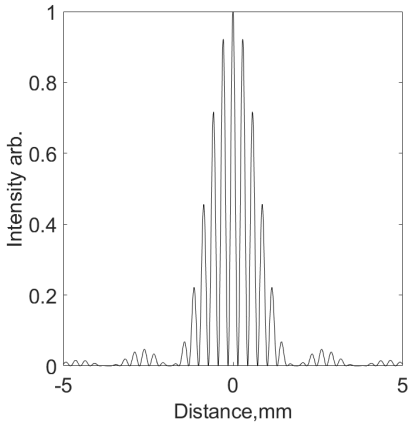

(a) Perfectly coherent source

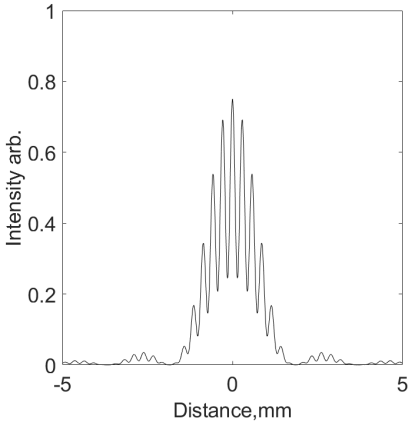

(b) Spatially incoherent source

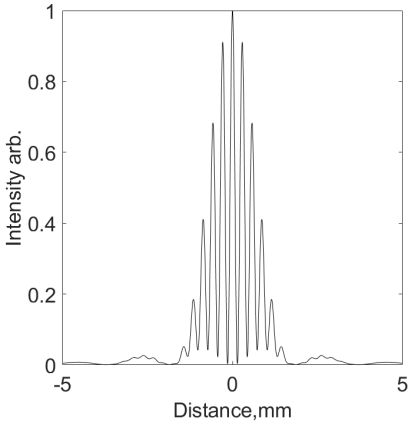

(c) Polychromatic source

FIGURE 2.9: The effect of different types of coherence on a double slit diffraction pattern.

the cost of reduced flux. Also, since the long trajectory is annular within some phase matching conditions as shown by the cross section in figure 2.7, the short trajectory may be isolated at the centre of the beam, allowing high coherence within a limited area. However, it is important to note that this is only possible close to the focus; after a large enough propagation distance the HHG beam will be an inseparable mixture of the two trajectories across its spatial profile.

2.3 Summary

In this chapter, an introduction to nonlinear optics was given, with SHG used as a simple example of a frequency conversion mechanism. The principles of phase matching were introduced, for which we have stressed its importance in conversion efficiency.

The process of HHG was described, beginning with the basic three step model and giving some brief details of how a full quantum model may be implemented. The concepts of

long and short trajectories and cut-off frequency was introduced, and the shape of the HHG spectrum explained by considering which frequencies interfere constructively in consecutive high harmonic bursts.

The various contributions to phase matching were described in detail, including the mechanisms that give rise to them and how they may be controlled experimentally, establishing that the most important factors for our system are geometric and atomic phase. The phase matching model was used to build a map of coherence length over a cross section of the generation volume to see where the most efficient generation occurs for each trajectory as a guide for experimental work.

The properties of spatial and temporal coherence of an electric field were discussed, with their effects on interference and how they might be measured experimentally. The mechanisms that limit the spatial and temporal coherence in HHG have been described, including how the coherence properties may be improved.

The understanding gained here is particularly important for the work in chapter 4, providing the theoretical basis to guide EUV characterization and optimization for use in imaging experiments.

Chapter 3

Imaging Techniques

3.1 Optical Imaging

3.1.1 Traditional Microscopy

Traditional optical microscopy uses the basic principle of magnification by a lens to form an enlarged image of an object. For a single convex lens, the magnification is

$$M = 1 - \frac{f}{d_o} \tag{3.1}$$

where f is the lens focal length and d_o is the object to lens distance. Most conventional microscopes are compound microscopes, which use an objective lens to form an image which is then further magnified by an objective lens, allowing for much higher magnification. Though based on these two simple elements, in practice higher quality microscopes have multiple optical elements to allow high magnification and correct for optical aberrations. Instruments with this setup also allow for more complex illumination configurations with filtering in the Fourier plane, such as phase contrast where the zero order in spatial frequency is phase shifted by π radians compared with the other components, or Schlieren imaging where it is blocked completely.

3.1.1.1 Diffraction Limit

At higher magnifications, small point-like features in the object appear as Airy disks in the image due to diffraction of the illuminating light. For this reason, there is a limit to the resolving power of any such imaging system, which is defined as its ability to reproduce two nearby point-like objects such that they are distinguishable in the image. This is known as the diffraction limit, and it provides a fundamental minimum for the possible resolution for many imaging methods.

The minimum resolvable distance for an optical microscope was first described by Abbe, who gave the limit as

$$d = \frac{\lambda}{2\mathrm{NA}} \tag{3.2}$$

where λ is the wavelength of the illumination and NA is the numerical aperture, which defines the maximum angle θ that light may be accepted

$$\mathrm{NA} = \mathrm{n}\sin\theta \tag{3.3}$$

with n the refractive index. This dimensionless quantity is determined by the geometry of the system.

In practice, the real resolving capability of a microscope is not so simple to define; a more rigorous definition involves the point spread function (PSF). The PSF is the resulting distribution in the image for a point source in the object; it describes how badly the image will be blurred. This is distinct for each imaging setup, and the final image is a convolution between the PSF and the object:

$$\mathrm{Image} = \mathrm{PSF} \circledast \mathrm{Object} \tag{3.4}$$

an example is given in figure 3.1, where the PSF is assumed to be an Airy Disk function.

Alternatively, we can consider the optical transfer function (OTF). This describes how a sine-wave pattern of some spatial frequency in the object is translated to the image, defining attenuation and phase shift for each frequency. This provides an equivalent description; since the object may be decomposed into its spatial frequencies via a Fourier transform, the OTF is also the Fourier transform of the PSF, and can be considered its reciprocal space counterpart. Both of these functions describe the range of shortcomings of the imaging system in reproducing the object, including effects from optical aberrations.

3.1.2 Fluorescence Microscopy

Fluorescence is the process by which a substance absorbs radiation before re-emitting after a short delay (microseconds), usually at a longer wavelength. In some applications, it is useful to image light emitted from fluorescing molecules in addition to/instead of transmitted or reflected light [32]. This is particularly useful in imaging biological specimens, where fluorescent markers called fluorophores may be used to stain cells and highlight particular materials such as proteins of interest to researchers. Some

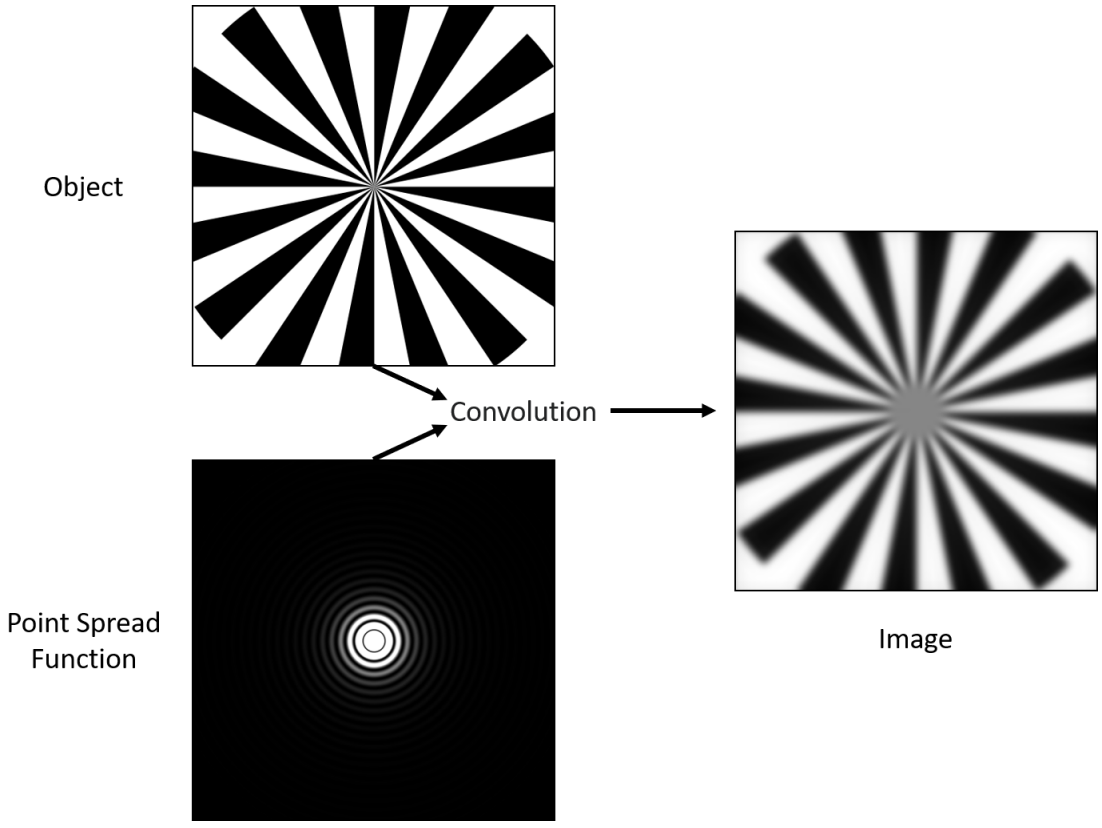

FIGURE 3.1: Simulated example of how the point spread function can cause blurring in the image, causing loss of resolution. The object here is a Siemens star, often used to estimate the resolution based on how close to the centre of the image the fringes are still visible.

biological materials will also re-emit light naturally by autofluorescence, which can allow identification of which proteins are present.

The most basic fluorescence microscope uses an excitation laser to illuminate the whole sample and an objective to image the fluorescence. Since this tends to be at a different wavelength, radiation from the laser can be filtered out to reduce noise from other light-matter interactions. The result is an easily obtainable wide-field image of fluorescing matter in the sample.

3.1.3 Super-Resolution Techniques

Based on the limit given in equation 3.2, there are two obvious routes to resolving smaller features: use a shorter illumination wavelength or increase the numerical aperture. The latter could mean using the refractive index dependence by immersing the system in a medium such as water or oil, or changing the geometry to increase the maximum acceptance angle. However, there are also numerous techniques that use different tricks to beat the ordinary diffraction limit, collectively known as super-resolution imaging

methods. Here I will summarize some of these techniques and outline their benefits and potential shortcomings.

Stimulated emission depletion (STED) fluorescence microscopy relies on reducing the size of the fluorescing region of the sample [33]. One beam hits a region of the sample to excite any fluorophores as in standard microscopy, and a second 'STED' beam with an annular profile is focused to the same region to stimulate emission within its spatial profile. This returns the fluorophores to their ground state and inhibits fluorescence, resulting in a smaller region within the hole of the STED beam that still contains excited molecules, the size of which is not diffraction limited. By scanning this spot across the sample, an image can be obtained with resolution that depends on the intensity of the STED beam; this has allowed images with a resolution of $<$50 nm [34]. However, the high intensity required for depletion means the technique is not suitable for more delicate samples prone to damage. Higher input intensity can also result in photobleaching, where light induced damage permanently removes the ability of a molecule to fluoresce, which limits the capability to image a sample multiple times.

Structured illumination microscopy (SIM) uses an illumination with a specific (and known) spatial pattern, for example a diffraction grating with a known period imaged onto the sample. Spatial frequencies in the object create interference fringes with the structure in the illumination due to the Moiré effect, the period of which depend on the orientation of the sample relative to the illumination structure, as demonstrated in figure 3.2. This allows information from higher spatial frequencies than can be accepted by the NA of the system to be encoded into features that can. By taking multiple images at different rotations and displacements of the illumination structure, deconvolution of the interference can be used to obtain an image with twofold improvement in resolution [35]. Images with a large field of view are possible with short acquisition times, and the low illumination intensity requirement allows for imaging of live cells [36], though the resolution enhancement is low compared with other techniques.

Stochastic optical reconstruction microscopy (STORM) relies on localization of individual fluorescent molecules [37]. The ability to distinguish two neighbouring fluorophores in a single image is limited by the diffraction limit; effectively they cannot be resolved as separate emitters if they are closer than the PSF of the system since they appear in the image as a spot of this size. However, this spot may be fitted to a spatial profile such as a Gaussian to obtain a value for its position. By taking a number of images with a low enough illumination intensity such that there is a low density of excited fluorophores, the positions of fluorescing molecules can be determined with much higher precision than allowed by the ordinary diffraction limit, down to 20nm [38]. The success of this technique relies heavily on correctly controlling the density of fluorescent markers during sample preparation; low enough to allow individual fluorophores to be identified and high enough to build a connected image of the sample structure.

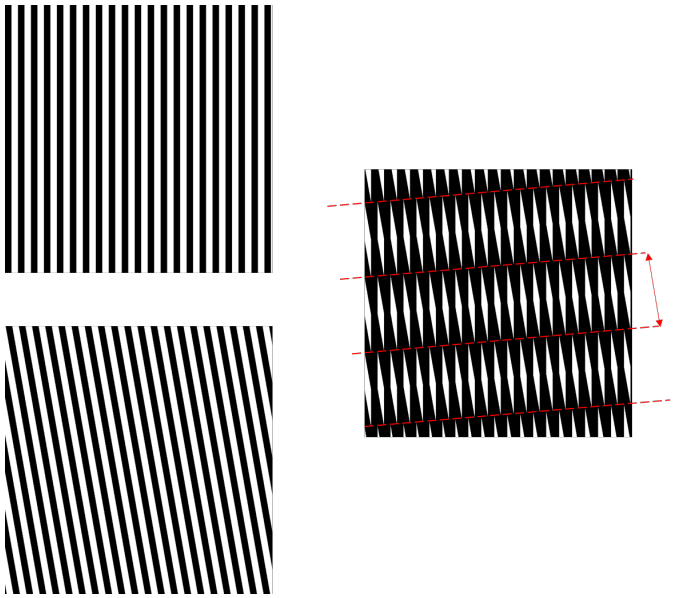

FIGURE 3.2: Demonstration of Moiré effect, where two identical periodic objects with a 10° difference in rotation combine to create fringes with a very different period when placed one in front of the other. The fringe period depends on the angle of their relative orientation

A similar method known as photoactivated location microscopy (PALM) also relies on excitation of a subset of fluorescent markers to localize their positions, but typically uses photoactivatable, photoconvertible or photoswitchable proteins as opposed to the organic dyes used in STORM. This means fluorescence from markers is confined to a short time window between photoactivation, where the protein emits radiation, and photobleaching, where the protein can no longer emit radiation. This is contrary to STORM, where the fluorophores blink on and off many times before photobleaching occurs. PALM has achieved similar resolution to STORM [39], and can also be combined with other methods to improve the signal-to-noise ratio of thinner samples [40], [41].

3.2 Lensless Imaging

3.2.1 Short Wavelength Optics

The brute force way to improve resolution on an optical imaging system is to use a shorter illumination wavelength. However, as the wavelengths decrease below the visible spectrum, there are issues with using the standard optical elements present in conventional microscopy. For a given material, the refractive index may be written as

$$n = 1 - \delta + i\beta \tag{3.5}$$

This is generally the form for refractive index used in x-ray applications, where δ is very small and positive for most materials. The real part describes a linear phase shift and the imaginary component dictates the magnitude of the attenuation. At extreme ultraviolet wavelengths of around 10-100 nm, the majority of materials have large values for β making them opaque in this regime, and for x-rays at 0.01-10 nm the value of δ approaches zero, such that refraction effects are minimal and the focal length of a conventional lens becomes unfeasibly long. For example, δ is $\sim 10^{-5}$ in Silica at a wavelength of 1 nm

There do exist solutions to overcome the issue for x-rays and enable more practical focal lengths. One example is a Fresnel zone plate (FZP), which is a structure of radially symmetric rings that alternate between transmitting and blocking radiation (or relative phase shifts of π radians between consecutive rings). The spacing of the rings is chosen such that radiation from a transmissive region of radius r_n will interfere constructively at the desired focal length f:

$$r_n^2 = n\lambda\left(f + \frac{n\lambda}{4}\right) \tag{3.6}$$

where n is an integer describing the ring number and λ is wavelength. This allows a focal length that is determined by the size of the features that can be fabricated on the FZP, and the performance of the optic is ultimately limited by the accuracy of the fabrication process. Also, this is sensitive to source bandwidth due to the wavelength dependence on focal length. For applications where preserving the signal level is important, FZPs may not be viable, as the typical power throughput is 10-20% for soft x-rays in the range of 100-2000 eV [42], largely due to the fraction of power diffracted to higher orders, and <10% for hard x-rays above 2 keV [43], where the vanishingly small features required in the FZP make accurate fabrication very difficult. However, sub 10 nm spot sizes are achievable by focusing x-rays with FZPs, which has allowed resolution in x-ray transmission scanning microscopy of 7 nm [44].

3.2.2 Propagation Techniques

Imaging without the use of focusing optics requires an understanding of how light propagates. In the case of free space propagation, starting from Maxwell's equations, we can arrive at the Helmholtz equation for an electric field E

$$\left(\nabla^2 + k^2\right) E = 0 \tag{3.7}$$

where ∇^2 is the Laplacian operator and $k = \omega/c$ is the vacuum wave number. This describes a monochromatic field with a single polarization; in general the field is a vector,

but provided the beam divergence is not so extreme, the polarization can be considered to be completely transverse to a single propagation axis such that we can write the field as a scalar function, and different polarizations can be considered separately provided there is no coupling between them. Also, a polychromatic source may be constructed as an incoherent sum of monochromatic fields, such that there is no loss of generality.

Light propagating through some aperture can be considered as a solution to the Helmholtz equation with some boundary conditions [45]. If we consider the situation of a monochromatic wave propagating from a source plane S_a (which represents the field exiting the aperture) and an incidence plane S_b (which might represent the field incident on a detector), the field in the incidence plane is related to the field in the source plane by the Huygens-Fresnel principle

$$E(x,y) = \frac{z}{i\lambda}\iint_{S_a} E(u,v)\frac{\exp(ikr)}{r}\,du\,dv \tag{3.8}$$

where u, v are spatial coordinates in the source plane, x,y are spatial coordinates in the incidence plane, z the perpendicular distance between the two planes and r the distance between a point on the source and a point on the incidence plane given by

$$r = \sqrt{z^2 + (x-u)^2 + (y-v)^2} \tag{3.9}$$

The integral in 3.8 is difficult to evaluate given the complicated dependence on the spatial coordinates. It is therefore useful to consider particular cases that allow some simplification of the propagation formula. We can expand our expression for r as a power series to allow separation of terms on the right hand side:

$$r = z\left[1 + \frac{1}{2}\left(\frac{x-u}{z}\right)^2 + \frac{1}{2}\left(\frac{y-v}{z}\right)^2 - \dots\right] \tag{3.10}$$

This result enables approximations to our scalar diffraction integral by taking as many terms as necessary for the desired accuracy - the larger the propagation distance, the fewer powers are required. Using only the terms written in 3.10 (up to those with z in the denominator), equation 3.8 can be expressed differently:

$$E(x,y) = \frac{1}{i\lambda z}e^{ik[z+\frac{1}{2z}(x^2+y^2)]}\iint_{S_a} E(u,v)e^{i\frac{k}{2z}(u^2+v^2)}e^{-i\frac{2\pi}{\lambda z}(xu+yv)}\,du\,dv \tag{3.11}$$

This is the Fresnel diffraction formula, and given the terms omitted from 3.10 it requires the condition

$$\frac{(x-u)^2+(y-v)^2}{4z^2} \ll 1 \tag{3.12}$$

Going to larger propagation distances, we can consider a further approximation in which the quadratic phase factor within the integral in 3.11 may be neglected and we can rewrite the diffraction formula as

$$E(x,y) = \frac{1}{i\lambda z} e^{ik[z+\frac{1}{2z}(x^2+y^2)]} \iint_{S_a} E(u,v) e^{-i\frac{2\pi}{\lambda z}(xu+yv)}\, du\, dv \tag{3.13}$$

which is the Fraunhofer diffraction approximation. The integral here is a direct Fourier transform of the field in the source plane with spatial frequencies $f_x = \frac{x}{\lambda z}$ and $f_y = \frac{y}{\lambda z}$; this approximation is particularly powerful given the availability of fast Fourier transform (FFT) algorithms to rapidly compute this numerically. Formally the condition for this regime is

$$\frac{k(u^2+v^2)_{max}}{2z} \ll 1 \tag{3.14}$$

However, for practical purposes it is useful to define the Fresnel number

$$N_F = \frac{D^2}{\lambda z} \tag{3.15}$$

where D is the extent of the aperture. We can then define a 'far field' regime $N_F \ll 1$ for which the Fraunhofer approximation is considered to be valid, and a 'near field' regime $N_F \gtrsim 1$ for which other techniques are required. The Fresnel diffraction formula in 3.11 works well when the Fresnel number is close to unity; at even shorter propagation lengths we require something else.

The angular spectrum method (ASM) is a very useful technique for propagation, since it may be used for any distance with sufficient sampling, provided the scalar approximation still holds, which means it can be extended to shorter distance propagation than other techniques. This method relies on the idea that taking a 2D Fourier transform of the field at S_a decomposes the field into a 2D 'angular spectrum', which may be considered as plane waves travelling in different directions away from the source plane. The angular spectrum in an incidence plane may be found by accounting for the phase shift each wave undergoes during propagation, then summing their contributions; the field in the incidence plane may then be determined via a 2D inverse Fourier transform. This propagation can be written as

$$E(x,y) = F^{-1}\Big\{H(u,v)\cdot F\big\{E(u,v)\big\}\Big\} \tag{3.16}$$

where $F\{\}$ denotes a Fourier transform and $F^{-1}\{\}$ its inverse, with H given by

$$H(u,v) = \exp\left[ikz\left(1 - \frac{u^2+v^2}{2k^2}\right)\right] \tag{3.17}$$

3.2.3 Coherent Diffraction Imaging

Coherent diffraction imaging (CDI) is a computational technique to image an object without the use of a lens. In 3.1.1, the lens was discussed as a means for magnification, however for any imaging system the magic of this optic is its ability to organize the phases of the scattered light to reproduce the object exit wave in the image plane. Given our understanding of radiation and the propagation techniques available, if we could measure the full electric field in some 2D plane after the object, image reconstruction would be a trivial problem. However, there is no direct way to measure the phase; though holography attempts to address this issue by encoding the phase information in the exit waves of the sample and a known reference object [46], the information is typically unattainable. The challenge is therefore to recover the half of the complex field that is lost, and is often referred to as the 'phase retrieval problem'.

In general, CDI methods are based on finding a solution to satisfy two sets of constraints, one in the object plane and one in the detector plane. If we place a sample in the object plane and illuminate it with a field P, the exit wave field ψ immediately after the sample is defined by the transmission properties of the object, and can be written as

$$\psi = P\exp\left[ik(\delta + i\beta)\Delta z\right] \tag{3.18}$$

where δ and β are the real and imaginary components of the material refractive index given in 3.5, and Δz is the sample thickness; all of these are defined at each transverse position in the object plane. This wave will propagate to the detector plane where its intensity is measured, from which an algorithm is implemented to reconstruct the exit wave. This outlines a key advantage of phase retrieval methods over standard microscopy - the full electric field is reconstructed, providing additional information related to the composition and thickness of the object.

The simplest version of CDI is the error reduction algorithm [47]; the basic steps are as follows:

1. The modulus of the field amplitude Ψ is obtained from the square root of the intensity distribution I measured in the detector plane. This amplitude is combined with randomly assigned phase information ϕ to use as an initial guess for

the electric field at the detector.

$$\Psi = \sqrt{I}\exp(i\phi) \tag{3.19}$$

2. The initial guess is numerically propagated to the object plane, where the random phases manifest in features that are not present in the original object.

3. Knowledge about the object is used to modify the guess for the exit wave, for example that the object is confined within a window of a known size outside of which no radiation is transmitted. This is the support constraint, written simply as

$$\psi \rightarrow \text{Support} \cdot \psi \tag{3.20}$$

4. The new guess for the object is projected into the detector plane by another numerical propagation. The amplitude information is replaced by the amplitude found in the first step to provide a new guess for the detector plane field. This is the modulus constraint, written as

$$\Psi \rightarrow \sqrt{\frac{\boldsymbol{I}}{\Psi}}\Psi \tag{3.21}$$

Steps 2 to 4 are repeated until a convergence is found. Optimally, there would only be a single solution that satisfies both constraints, but in practice there may be multiple solutions or none. In real applications, experimental errors and poor assumptions about the set up will generally mean that the constraints are too rigid and the algorithm will get stuck at a local minimum. To deal with this we can use relaxed constraints or allow the constraints to change during the reconstruction process, such as in the hybrid input output (HIO) algorithm [48]. Another issue that causes multiple solutions is 'twinning'; since the phase information is initially unknown, both the object exit wave and its complex conjugate can fulfill the modulus constraint. The result in the image is a second solution rotated by 180° with respect to the first. There are numerous variations to the described approach designed to make convergence more likely and improve the quality of the final object estimate.

It is important to note that the above approach is valid for optically thin samples $|k(1-n)\Delta z| \ll 1$, though thick samples may be modelled as a number of thin slices where the illumination of each is calculated by propagation of the exit wave of the previous slice by a short distance [49].

3.2.3.1 Oversampling Requirement

Invariably, the measured intensity will be an array of values determined by the pixels of a digital detector - if this is a grid of $N \times N$ points, the initial guess for the detector

field is the same size, and back-propagation to the object plane will yield an $N \times N$ grid for the exit wave. In the far field regime, the extent of the object D is inversely proportional to the detector pixel size p

$$D = \frac{\lambda z}{p} \tag{3.22}$$

As a result, we require a sufficient sampling rate in the detector plane to give us a large enough field of view in the object plane to implement the support constraint. This is equivalent to considering that the highest possible frequency in the diffraction pattern is determined by the physical size of the support in the object plane, as described by the Nyquist limit [50]. It is important to note that each frequency in the recorded intensity is doubled compared with the electric field, since it is proportional to the field squared. Therefore the oversampling requirement is that the support size is half the extent of the calculated object or smaller [51].

3.2.3.2 Coherence Requirement

Coherence in CDI is crucial; though post processing methods can allow some tolerance in the spatial and temporal coherence requirement, the principle of propagating the field back and forth between two planes requires that the phase of each wavefront follows a fixed relationship. The necessary transverse coherence length proposed in [52] is twice the object size, though this is a conservative estimate - in practice CDI is still possible with shorter coherence lengths.

3.2.4 Ptychography

Ptychography is a special version of CDI [53, 54] that uses a number of diffraction patterns to form an image rather than just one. Here, rather than choosing a sample confined within a support, we confine the illumination by an aperture of a known size placed close to the sample; this illumination is called the probe. Then by scanning the probe in two dimensions (or the sample relative to the probe), we can record diffraction patterns from a series of overlapping positions in the object plane. In this way, the support constraint may be replaced by an overlap constraint, where we know that areas within two overlapping probe positions must be identical. The main algorithms used for reconstructing images in this thesis are ePIE [55] and difference map [56].

The ePIE algorithm is as follows:

1. The exit wave ψ_j at scan position j is considered to be formed by transmission of the probe P through the object O, so an initial guess for the exit wave is made by estimates of the object transmission and probe amplitude at each scan position

$$\psi_j(\mathbf{r}) = O(\mathbf{r})P(\mathbf{r} - \mathbf{R}_j) \tag{3.23}$$

where $\mathbf{r}$ is the real space coordinate vector and $\mathbf{R}_j$ tells us the position of the j^{th} probe relative to the object.

2. The exit wave is propagated to the detector plane - in far field imaging, this is just a Fourier transform

$$\Psi_j = F(\psi_j) \tag{3.24}$$

3. The modulus constraint is applied to the detector plane wave using the measured intensity at the j^{th} scan position

$$\Psi_j = \sqrt{I_j}\frac{\Psi_j}{|\Psi_j|} \tag{3.25}$$

4. Propagation back to real space provides an updated exit wave

$$\psi'_j = F^{-1}(\Psi_j) \tag{3.26}$$

5. The exit wave is used to update the illumination and object function of the next scan position via

$$O_{j+1}(\mathbf{r}) = O_j(\mathbf{r}) + \alpha\frac{P_j^*(\mathbf{r} - \mathbf{R}_j)}{|P_j(\mathbf{r} - \mathbf{R}_j)|^2_{max}}(\psi'_j(\mathbf{r}) - \psi_j(\mathbf{r})) \tag{3.27}$$

$$P_{j+1}(\mathbf{r}) = P_j(\mathbf{r}) + \beta\frac{O_j^*(\mathbf{r} - \mathbf{R}_j)}{|O_j(\mathbf{r} - \mathbf{R}_j)|^2_{max}}(\psi_j(\mathbf{r})' - \psi_j(\mathbf{r})) \tag{3.28}$$

where α and β are coefficients that determine the step size of each iteration; this implements the overlap constraint on scan position $j + 1$.

6. These steps are taken for all scan positions, and the updated object and illumination functions provide an estimate for the exit waves to use in the next iteration.

To estimate the quality of the reconstruction at each step, an error metric is defined:

$$e = \frac{\sum_j \sum_u (\Psi_j(u) - \sqrt{I_j(u)})^2}{\left|\sum_j \sum_u I_j(u)\right|^2} \tag{3.29}$$

where u denotes detector pixel index. This is reduced as the algorithm approaches a solution, and is zero for a perfect solution. In practice, this method can still stagnate

at a sub-optimal, local solution; the difference map algorithm uses a similar procedure, but projects the solution using both constraints simultaneously in each iteration, and the updated exit wave function is based upon the difference between the two solutions. This can prevent the algorithm getting stuck with a high error function, but is more computationally intensive and is sensitive to experimental errors.

This mode of scanning CDI has some major advantages, some of them are listed below:

- Though the object estimate at each probe position is limited to an $N \times N$ array defined by the detector, the final reconstructed object can be any size, limited by the extent of the total scan area.
- The overlap constraint tends to be much more robust than the support constraint; the previous twinning problem in CDI is no longer present because the overlapping regions must have the same orientation, requiring a unique solution.
- The probe and object are both reconstructed, allowing for the illumination profile to be unknown.
- The oversampling and coherence requirements now only exist across the extent of the probe rather than the entire object.

The probe can be as small as we want, though a smaller probe requires more diffraction patterns to keep the same level of overlap. For a scan with a circular probe of diameter d_p and distance between adjacent scan positions L, the overlap ratio is

$$O = 1 - \frac{d_p}{L} \tag{3.30}$$

A suggested overlap ratio of 0.6-0.85 has been proposed [57] to yield high quality reconstructions; higher overlap provides a stronger constraint and makes convergence more likely at the cost of longer scan times, but may be recommended for systems with lower coherence or greater experimental errors.

These advantages are at the cost of additional time in acquiring and processing a large number of diffraction patterns, and investment in high quality stages such that the probe position is known to a high degree of accuracy. This method also assumes knowledge about the geometry, such as the distances from the probe to the sample and from the sample to the detector, though these quantities can be optimized during the reconstruction process.

3.2.4.1 Correcting Errors

There are a number of errors introduced in any imaging technique that affect the image quality. All optical methods deal with photon detection, for which there are limitations with detector sensitivity and noise - these issues are discussed in detail in 4.3.2.2. Many of the errors unique to ptychography can be corrected, either by pre-processing the data or during the reconstruction process.

Actuator errors when moving between each scan position add a random error to the probe position relative to the object, and incorrect geometry estimation can add global scaling errors to the probe position, for example if the stage is calibrated incorrectly, or if the stage coordinates are rotated relative to the detector plane coordinates. One method to correct for these errors is with an annealing algorithm [58]. The process is as follows:

1. For the j^{th} scan index, generate k random probe positions that lie on a circle of radius r around the original.
2. Propagate the exit wave ψ_k calculated by the probe-object overlap at each of the positions on the circle to generate k calculated intensities $|\Psi_k|^2$.
3. Find the error between the calculated intensities and the detected intensity at this scan position
$$e_k = \sum_u \left(I(u) - |\Psi_k(u)|^2\right)^2 \tag{3.31}$$
4. Compare the errors for the points on the circle with the original, then choose a position for which the error is a minimum.
5. Move to the next iteration and generate k new positions on a circle with a smaller radius.

This can be implemented at all scan positions to reduce the error metric in 3.29.

A number of factors can cause blurring in the diffraction plane, such as a broadband illumination spectrum, sample motion or vibration, and pointing stability of the source. Uncertainty in the intensity measurement due to the pixel size of the camera can have a similar effect. It has been shown that the intensity can be modelled as a convolution between a purely coherent source and some profile, from which some blurring of diffraction patterns can be corrected by deconvolution. Alternatively, the intensity can be modelled as the sum of a number of incoherent, orthogonal states [59]

$$I = \sum_k I_k \tag{3.32}$$

This method is particularly good for separating contributions from multiple wavelengths in the illumination.

Another correction is called orthogonal probe relaxation (OPR) [9], which is useful for dealing with an unstable illumination profile; this makes it particularly appropriate for coping with HHG sources, where the highly nonlinear process tends to amplify any instability in the input beam. In this method, the reconstructed probes from all of the positions are put into a single matrix, with each probe represented by a single row. A singular value decomposition (SVD) is implemented to produce a number of orthogonal, coherent modes, with weighting coefficients represented in the singular values. The probes can then be rebuilt with the first few of these modes; much of the random noise in the probe illumination is removed by ignoring the smaller singular values.

3.2.5 Resolution

Akin to conventional microscopy, the resolution of lensless techniques depends on the PSF of the system. For far field imaging, the diffraction limit in 3.2 still applies, where now the NA of the system depends on the size and proximity of the detector as well as the illumination wavelength. However, since measurement takes place in the Fourier plane, final image resolution is limited by the signal to noise ratio (SNR). Higher spatial frequencies tend to be lower in amplitude, and the smallest resolvable object is defined by the highest spatial frequency that the system can accept, therefore the resolution is limited by the highest spatial frequency that is distinguishable from noise.

3.3 Other Imaging Techniques

3.3.1 Electron Microscopy

Electron microscopy uses the wave-like properties of electrons to image a specimen in a similar way to optical microscopy, but using electrons in the illumination rather than photons. This yields some key advantages over conventional microscopy, the most obvious being the availability of extremely short wavelengths, following de Broglie's relation [60]

$$\lambda = \frac{h}{p} \tag{3.33}$$

where p is the electron momentum. The electron mass allows generation of high energy waves with relative ease compared with photon generation, and as a result extremely high resolution is achievable without the necessity of phase retrieval methods; electrons accelerated by a potential of just 1 volt already have a wavelength of 1.23 nm. Still,

techniques such as ptychography have been used for increased information about the sample and improved image quality.

Electron microscopy can operate in a number of configurations, using different types of electron interactions. The most common forms are transmission electron microscopy (TEM), which measures transmitted and diffracted electrons, and scanning electron microscopy (SEM), which can measure backscattered, secondary and Auger electrons. Due to the strong interactions of electrons with most materials, TEM requires extremely thin samples (∼100 nm), which makes sample preparation challenging, particularly for biological specimens. TEM can allow sub-Ångstrom resolution [11]; SEM cannot achieve the same level of resolution, and only images the surface of the object, but does not require such extreme sample preparation methods.

All electron microscopy methods can cause significant damage to biological samples, via heat or ionization events. The focused electron beam requires vacuum conditions to operate properly to avoid interactions with air, which causes dehydration, and at high enough beam energies the sample must be cooled to cryogenic temperatures. For every additional measure to prepare for imaging, the sample looks less like its natural state, which poses the question of what level of sample invasion is acceptable to achieve high resolution.

3.3.2 Scanning Tunneling Microscopy

Scanning tunneling microscopy (STM) is a contact technique which measures electrons that tunnel from the surface of an object to a conducting tip due to the presence of a bias voltage. The probability of an electron tunneling is highly dependent on the proximity of the tip and the object, which can produce a map of the surface with 0.01nm vertical and 0.1nm transverse resolution [61]. However, the operating mechanism requires the sample to be conducting, which limits the range of samples that may be imaged by this method.

3.3.3 Atomic Force Microscopy

Atomic force microscopy (AFM) is another contact technique, and similarly to STM it involves scanning a tip across the surface of a sample, but measures the height of the tip due to forces from the surface rather than tunneled electrons. This can be performed extremely close to the surface in which static repulsion is measured, or further away in which the lever on which the tip is mounted is oscillated and fluctuations in amplitude due to contact or van der Waals forces are measured; vertical resolution of 0.1 nm is possible with this technique, though interactions with the tip can cause sample degradation, and imaging wet samples is problematic as the tip can stick to the sample.

3.4 Summary

In this chapter, a brief introduction of traditional optical microscopy based on imaging with a lens has been given, introducing the diffraction limit as a restriction on available resolution.

The idea of using fluorescence to image markers in a sample was discussed, particularly as a means to highlight biological structures, and a number of super-resolution techniques that are capable of beating the diffraction limit described, with potential benefits and drawbacks for each and maximum resolution capability.

The motivation for lensless imaging has been described, with the lack of availability of efficient optics at short wavelengths discussed. The theory of light propagation required for coherent imaging techniques was described in detail, with the introduction of near and far field regimes determined by the Fresnel number, and which approximate propagation method should be used in each.

The background of CDI as a means to retrieve the phase information lost when measuring the diffracted intensity has been given, introducing the constraints in real and Fourier space as well as the oversampling and coherence requirements. This provided a basis to discuss ptychography as an extension to this method, where we have seen the working of the algorithm in more detail including some of the methods used to correct systematic errors in the experiment, along with the advantages of ptychography over standard CDI. The available resolution of lensless techniques and the connection with the SNR was also introduced as a limitation that does not exist in standard microscopy.

Finally, some other imaging techniques were discussed, in particular electron and contact based microscopy, with the resolution capability and limitations given for each.

The theoretical concepts examined here are important to understand why the coherence of the source and SNR are so crucial for our imaging technique, which provides a motivation for the source development work performed in chapter 4. The other imaging techniques that have been described give an idea of the current capabilities of a range of imaging methods, which provides some context for the ptychographic imaging results detailed in chapter 5.

Chapter 4

Extreme Ultraviolet Source

In this section, I will outline the steps taken to produce extreme ultraviolet illumination of sufficient brightness and quality for ptychographic imaging, as well as the process of characterizing the source.

4.1 Laser System

A schematic of the laser system is shown in figure 4.1; it consists of a Ti:Sapphire oscillator which is end pumped by a frequency doubled Nd:YVO_4 continuous wave laser. An acousto-optic modulator (AOM) is used to initiate mode locking; this is disabled after pulsed operation is achieved and the oscillator continues to emit pulses passively via Kerr

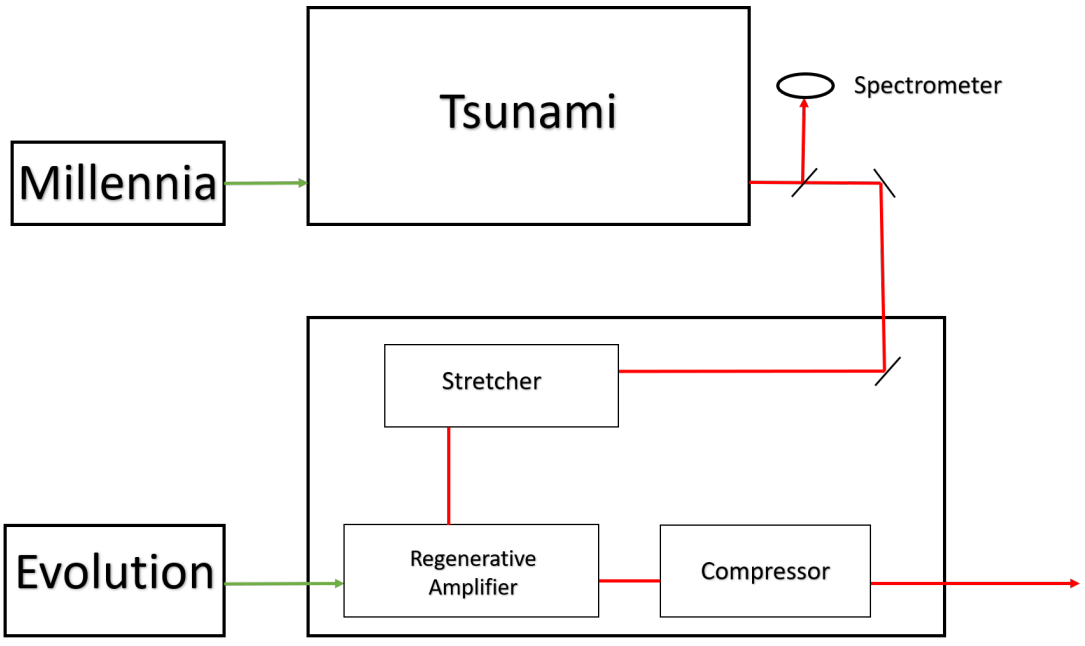

FIGURE 4.1: Schematic of the laser oscillator, amplifier and pump lasers.

lens mode locking. The positions of the four prisms that comprise the compressor in the cavity can then be adjusted to maximize the laser bandwidth (50 nm centred at 800 nm), corresponding to the shortest output pulse length. The output is measured by a spectrometer to ensure the largest available bandwidth. Assuming transform limited Gaussian pulses, the full width at half maximum pulse duration τ_p is given by

$$\tau_p \approx \frac{0.44}{\Delta\nu} \tag{4.1}$$

where $\Delta\nu$ is the frequency bandwidth. For a 50 nm bandwidth, this gives a pulse duration of around 20 fs. The average output power is 300 mW with a repetition rate of 80 MHz, so each pulse has an energy of about 4 nJ.

The output from the oscillator is sent to a regenerative amplifier system. This system consists of a stretcher, amplifier and compressor. The Ti:Sapphire gain medium in the amplifier cavity is pumped by a frequency doubled Nd:YLF laser with a 1 kHz repetition rate from both ends simultaneously. Pulses from the oscillator are first bounced off a grating/mirror pair repeatedly to add chirp, stretching them in time. Every 1ms a single pulse is switched into the cavity via a pair of Pockels cells, timed to coincide with a pulse from the pump laser. The pulse remains in the cavity for a number of round trips to maximize amplification, then is switched back out and sent to another grating/mirror pair to remove the chirp and compress the pulse. The final output from the amplifier is 2.5 mJ pulses at 1 kHz repetition rate, and 50 fs pulse duration, with a Gaussian beam radius of 5.5 mm.

4.2 Diagnostics

HHG is a complicated process that depends on a large number of variables. In order to produce a quality EUV source consistently, it is very important to well understand the ingredients that go into it. As a result, a series of tools were put in place to monitor the performance of the IR beam from the amplifier such that any variance in the EUV source might be diagnosed. The beam path out of the amplifier to the various diagnostics is shown in figure 4.2

4.2.1 Pulse Length Measurement

Since HHG is intensity dependent, the pulse duration is an important parameter to monitor. This was measured using a ‘grating-eliminated no-nonsense observation of ultrafast incident laser light e-fields’ (GRENOUILLE) device. This operates via the same principle as frequency resolved optical gating (FROG), but allows for a single shot measurement of the pulse length.

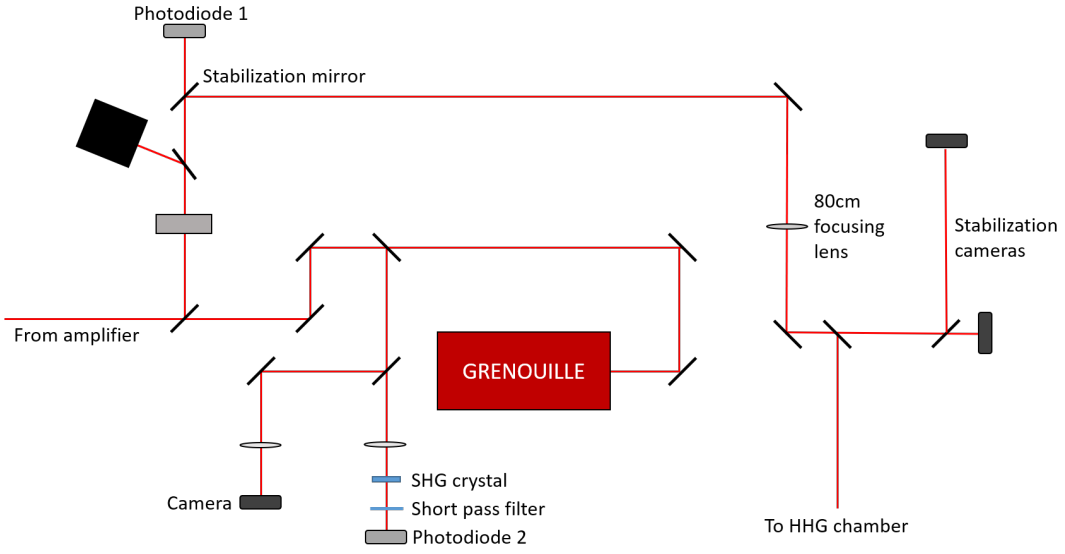

FIGURE 4.2: Beam path of the diagnostics. The stabilization mirror and 80 cm focusing lens are mounted on actuators to allow active stabilization, as described in 4.2.2. Photodiode 1 and 2 combine to get a simple pulse length measurement.

In the horizontal direction, a Fresnel biprism splits the pulse into two beams and focuses them into a thick SHG crystal, superimposing the two at the focus. This creates a dependence between position and delay time between the split pulses, due to the difference in path length of the two beams at the overlap in the crystal. This is imaged onto a camera via a cylindrical lens. In the vertical direction, the pulse is focused into the same crystal by a cylindrical lens. As the pulses propagate through the crystal, different wavelengths in the pulse are phase matched at specific k vectors. Another cylindrical lens projects this onto the camera.

The result is a second harmonic signal that depends on wavelength in the vertical direction and time delay in the horizontal direction, since SHG in this case depends on the intensity of the pulse overlap and on the critical phase matching condition. The resulting image is the pulse overlap function with wavelength and time as the vertical and horizontal axes, from which the original pulse duration is determined using an iterative algorithm.

4.2.2 Beam Position and Stability

The beam position and propagation angle is subject to short and long term drift as a result of different mechanisms. During any HHG experiment, it is important to reduce these effects as much as possible.

4.2.2.1 Passive Stabilization

The short term effects (less than a second) are as a result of fast fluctuations in air pressure caused by airflow across the beam, which is due to movement around the lab, air conditioning, etc. They can be reduced by sealing the beam path from the rest of the experimental environment.

Another source of rapid beam movements is from vibration of the lab bench, which can be negated by ensuring no vibrating equipment such as vacuum pumps comes into contact with it.

4.2.2.2 Active Stabilization

Beam position drift over long periods (a few hours) are caused by temperature changes in the lab, which can cause the bench to slightly change shape due to expansion/contraction. This also causes the length of the compressor in the amplifier to change, which causes pulse length drift over similar durations. Generally the pulse length is corrected manually during a long experiment, but the beam position is actively corrected during an experiment by an automated stabilization system.

The system consists of two pairs of Newport picomotors connected to a stabilization mirror and a focusing lens, and two CMOS cameras at separate locations along the beam path. The cameras measure the transverse beam profile, and the picomotors allow for the beam position and propagation direction to be adjusted to maintain the desired alignment. All of the hardware is controlled by a Raspberry Pi, with software developed by previous student Michal Odstrcil.

For each camera image, the desired beam position is first inputted into the system. The current beam position is then determined based on the centre of mass of each camera image, and the difference (or error) between the current and input position is computed for the horizontal and vertical directions. The software then uses a feedback loop based on a proportional-integral-derivative (PID) system to decide what the picomotor action should be. This system maintains the beam position whilst avoiding feedback oscillations that would reduce short term stability. The result of using this system is illustrated in figure 4.3.

4.2.3 M^2 Parameter

We can approximate the laser beam using the Gaussian solution given in equation 2.21. However, this only describes a fundamental transverse mode. Higher order transverse electromagnetic (TEM) modes also exist, described by

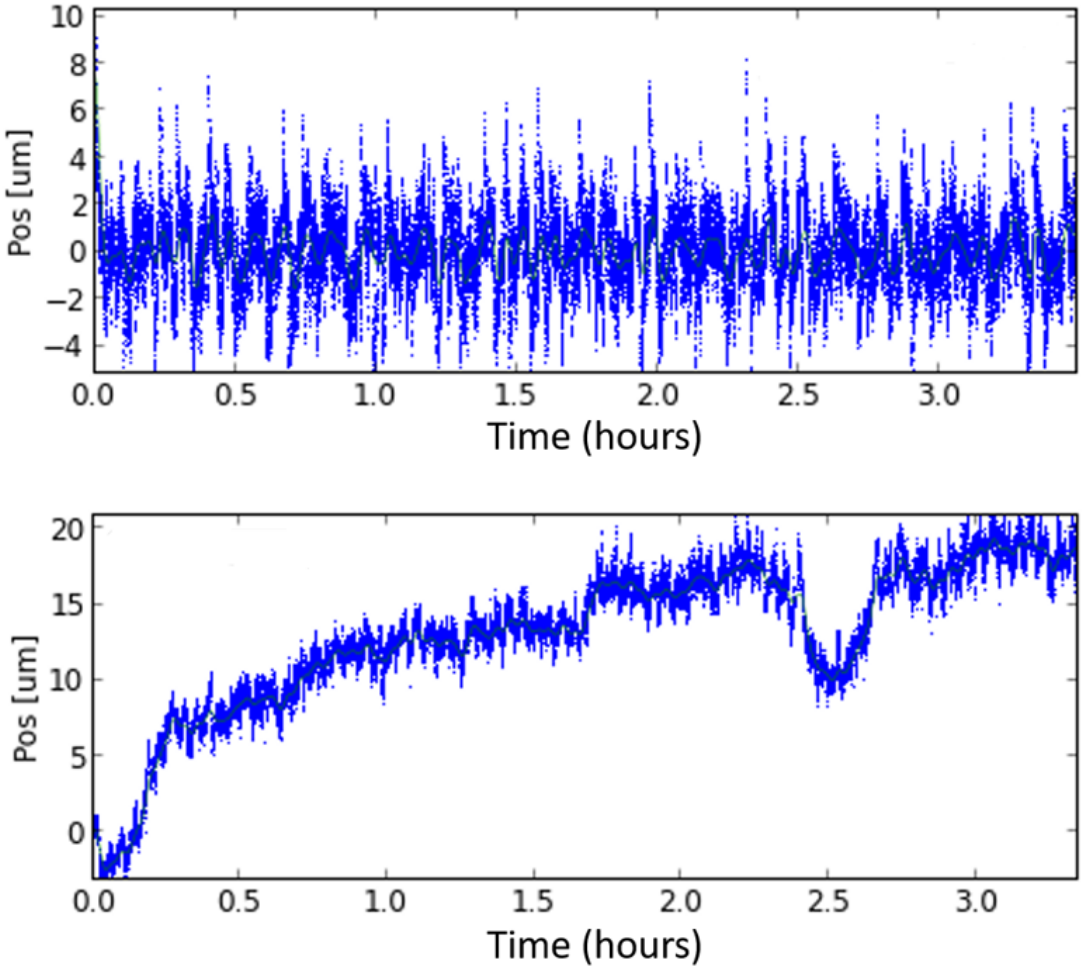

FIGURE 4.3: Vertical beam position (centre of mass) for a single camera during an experiment using active stabilization (top) and without active stabilization (bottom). Whilst short term fluctuations are comparable in magnitude, the long term beam position is much more stable when the stabilization system is running.

$$E_{mn}(x,y,z) = E_0 \frac{w_0}{w} H_m\left(\frac{\sqrt{2}x}{w}\right) H_n\left(\frac{\sqrt{2}y}{w}\right) \exp\left[-(x^2+y^2)\left(\frac{1}{w^2}+\frac{ik}{2R}\right) - ikz - i(m+n+1)\phi_g\right] \tag{4.2}$$

where $H_{m,n}$ are Hermite polynomials. Note that for $n, m = 0$ this reduces to the fundamental Gaussian solution given before, or the TEM_{00} transverse mode. These provide a set of orthogonal modes, and in principle the laser profile can be reproduced by a sum of these modes. Alternatively, we can consider that the combination of modes will increase the overall far field divergence θ by a factor M^2 compared with the 'embedded Gaussian', which is the TEM_{00} mode:

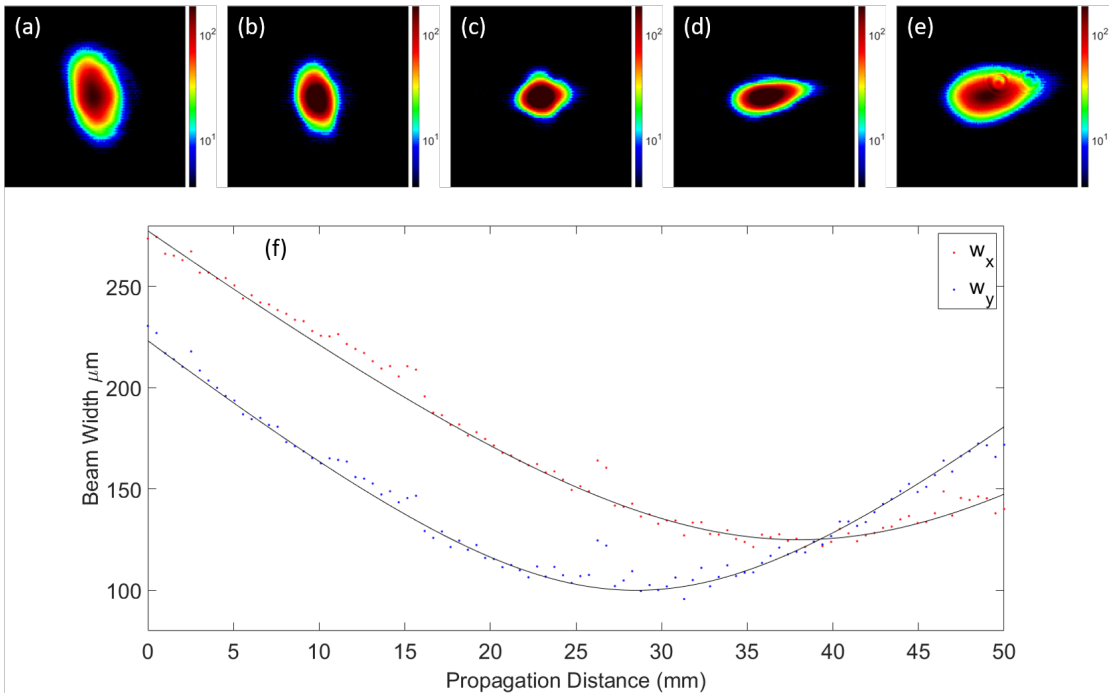

FIGURE 4.4: (a-e) show intensity cross sections of the IR beam measured by a CMOS camera at positions through the focus of 20 mm, 27 mm, 35 mm, 42 mm and 50 mm respectively. A total of 100 images were collected over a range of 50 mm and the horizontal and vertical Gaussian beam widths calculated separately using the second moment method; the values are plotted in (f), with red points corresponding to horizontal widths and blue points to vertical widths. The data was also fit to equation 4.4 as indicated by the black solid lines. The fit values for M^2 were 3.2 in the horizontal direction, and 2.75 in the vertical.

$$\theta = M^2 \frac{\lambda}{\pi w_0} \tag{4.3}$$

If we know the value of M^2, this allows us to consider propagation of the embedded Gaussian only, then we can calculate the actual beam width W at any point along the beam path via $W(z) = Mw(z)$. This is also a simple measure of beam quality, given that higher M^2 values imply a mixture of higher order modes in the beam. A pure TEM_{00} mode will exhibit an M^2 factor of 1.

Measuring the M^2 parameter requires sampling the beam profile through a focus at various z positions along the propagation axis, calculating the beam width at each point, then fitting the widths to the theoretical width:

$$w(z) = w_0 \sqrt{1 + \left(M^2 \frac{z}{z_R} \right)^2} \tag{4.4}$$

Figure 4.4 shows the results of an M^2 measurement for which 100 images were collected by a CMOS camera over a total range of 50 mm along the beam propagation axis. (a-e)

show individual intensity profiles, and (f) is a plot of all the Gaussian horizontal (red points) and vertical (blue points) beam widths, and fits to equation 4.4 (solid black lines). The widths were determined via the second moment definition:

$$\begin{aligned} w_x &= 2\sigma_x \\ &= \frac{\iint (x - x_0)^2 I(x,y)\, dx\, dy}{\iint I(x,y)\, dx\, dy} \end{aligned} \tag{4.5}$$

where x_0 is the centre of mass in x, and the same for w_y. The fit data gives a minimum beam waist of 125 µm in the horizontal and 100 µm in the vertical direction, with an M^2 parameter of 3.2 horizontally and 2.75 vertically. These values are larger than we expect; an M^2 of <2 should be achievable with our system.

4.3 Extreme Ultraviolet Generation

4.3.1 Set-up

The EUV generation set-up is shown in figure 4.5. Light from the amplifier is focused by an 80 cm convex lens onto two alignment mirrors. The transmission through the second mirror is sent to a pair of stabilization cameras, described in 4.2.2. The reflected light passes through a mechanical shutter, which sets the exposure time of the EUV camera in the imaging chamber. After passing through a window at Brewster's angle (to remove horizontal polarization), the beam goes into a copper cell. This cell is within a vacuum chamber at 10^{-4} mbar, and can be filled with argon gas at a controllable pressure. This is kept at around 80 mbar, because the EUV flux increases approximately linearly for lower pressure and starts to decrease at higher pressures due to absorption. The position of the lens can also be adjusted by a translation stage to shift the focus position relative to the cell.

Radiation transmitted by the cell consists of 800 nm light from the amplifier and high order harmonics generated in the gas. This radiation is filtered by two 200 nm thick pieces of aluminium foil, which each attenuate the 800 nm radiation whilst transmitting $\sim 60\%$ of radiation at 29 nm.

The filtered radiation passes into the imaging chamber. The set-up used to analyse the EUV beam is shown in figure 4.6; the same geometry is used for ptychographic imaging. The EUV beam is focused by a spherical MoSi multi layer mirror with 50 cm radius of curvature. This mirror has a central wavelength of 29 nm and a FWHM bandwidth of 4 nm, so acts as a spectral filter to pick out the 27^{th} harmonic of the fundamental

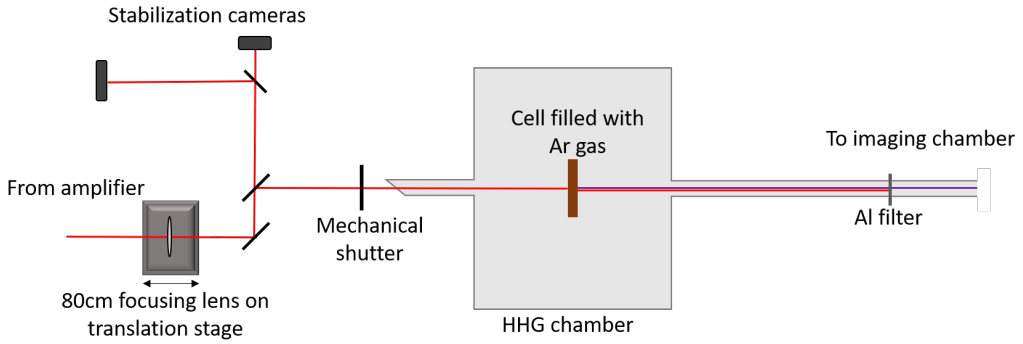

FIGURE 4.5: HHG set-up. Light from the amplifier is focused by an 80 cm focusing lens into a 3mm thick cell filled with Argon gas, which is placed inside a high vacuum. Light transmitted by the cell is filtered by two 200nm thick Aluminium foil filters to remove 800 nm radiation. The mechanical shutter is used to limit the exposure time of the EUV camera in the imaging chamber.

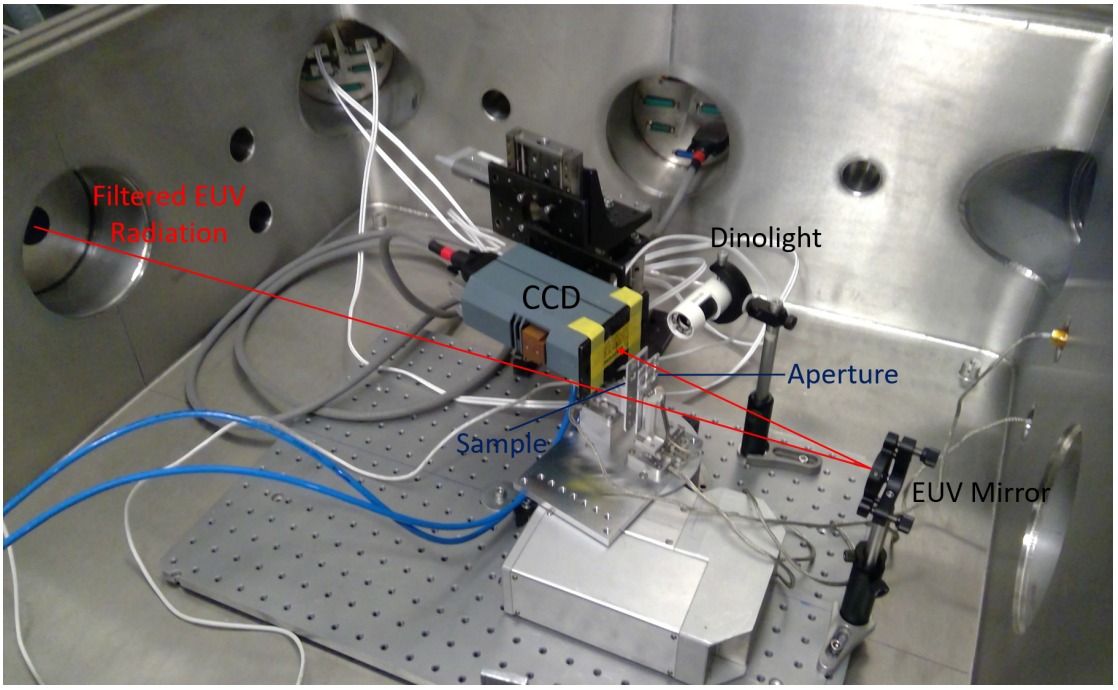

FIGURE 4.6: Photo of the experimental set up used for EUV beam characterization and ptychographic imaging.

laser wavelength. An Andor DX-434 EUV CCD camera is used to measure the incident light. The pinhole and sample stages are controlled by Smaract nanometer precision actuators, and can be removed to observe the EUV profile, or objects such as double slits may be positioned to determine beam characteristics and quality.

4.3.2 Data Collection

The efficiency and reliability of the detector that we use to measure the EUV radiation is useful for beam characterization, and crucial in ptychographic imaging, where there

is an intimate connection between the signal-to-noise ratio (SNR) and the effective resolution of the final image (unlike conventional microscopy). For this reason, the main consideration in choosing a detector is maximizing the SNR, which primarily means reducing sources of noise. This may also be done during post processing of the collected data to some extent as we will see shortly.

4.3.2.1 Detector Types

When considering which type of detector to use for imaging applications, there are two main competitors: charge coupled devices (CCDs) and cameras based on complementary metal oxide semiconductor (CMOS) technology. Both types use an array of silicon pixels to detect light, in which a photon incident on a pixel promotes some number of electrons from the valence band into the conduction band. The electrons are confined to within each pixel by a bias voltage whilst the sensor is exposed to radiation, and can then be converted from an analogue to a digital signal by some electronics. However, this readout process is different for each; a CCD uses a shifting voltage to move the accumulated charge from one pixel to the next along the entire row, where the time that each charge packet arrives determines the pixel that it came from, whereas a CMOS camera converts the charge to a voltage at every pixel.

Whilst there are a number of relevant factors to consider such as cost, CCDs generally provide advantages over CMOS devices for imaging applications in which the SNR is critical. Specifically, the thermal noise is much lower for CCDs, where the large number of sensors on a CMOS camera produce significantly more heat, and operation at very cold temperatures is difficult to achieve. For this reason, a CCD camera was used for this work for all EUV detection. However, CMOS technology has rapidly advanced in recent years, and may eventually outperform CCDs for similar work if the noise levels become acceptable. In particular, the readout of CMOS cameras can be 1-2 orders of magnitude faster, and currently the readout accounts for most of the time taken to run an imaging scan with our set up; the time to read out the full 1024 by 1024 pixels on the camera is around 30 seconds for the lowest readout noise setting. By comparison, the other limiting factor of data acquisition speed for a typical imaging scan with our system is exposure time, for which we generally use a maximum of 10-15 seconds.

To increase the data acquisition speed, our CCD camera allows a variable binning setting b, for which $2^b \times 2^b$ pixels are read together as a single pixel value, and reduces the acquisition time by a factor of $\sim 4^b$, and a cropping value c, for which only pixels within a square region of width $1024/2^c$ around the centre of the sensor are read, reducing the acquisition time by a factor of $\sim 4^c$. For diffractive imaging, we generally use a cropping of 1 to maintain the maximum possible NA and the highest binning setting for which we can maintain sufficient sampling to satisfy the oversampling constraint in ptychography.

4.3.2.2 Noise and Efficiency

The SNR of the collected data depends on the strength of the input signal (or beam intensity, in our case), the sensitivity of the detector, and on the reduction and subtraction of noise. The sensitivity of the detector is determined by its quantum efficiency Q at the wavelength of interest. We can convert the total counts to the original number of photons N incident on a pixel during an exposure of time t via

$$N = \frac{C}{Q \times t \times \text{cpp}} \tag{4.6}$$

where C is the measured counts and cpp is the counts per absorbed photon, which depends on the internal gain setting controlled by the manufacturer and the readout speed. However, for this to be accurate, we first need to carefully estimate the noise and subtract it from the number of counts, which requires an understanding of where noise comes from.

The first type of noise we consider is readout noise. This is created during the process of converting the electrons in the potential well of each pixel into measured counts via analogue to digital conversion and amplification. In the case of a CCD where all of the pixels are read during a single process, the readout noise can be described by a single value. It is also independent of exposure time, so dominates the noise for very short exposures.

Secondly, we consider thermal noise. This arises because the electron energies in a semiconductor follow a Boltzmann distribution, for which the probability that an electron will occupy a state of energy E is proportional to the Boltzmann factor $e^{-\frac{E}{kT}}$, where k is the Boltzmann constant and T the temperature. This means that some fraction of electrons have sufficient energy to be promoted to the conduction band without the presence of an incident photon. This results in a measurement of counts, the magnitude of which depends on the sensor temperature and not the signal level. This grows linearly with exposure time. Also, some number of thermal electrons will be produced during the readout process, which can cause a linear noise build up across the data in the direction that the pixels are read.

The third kind of noise to consider is shot noise. This exists for measurements that involve counting a discrete number of events, and can be approximated by a Poisson distribution for sufficiently large numbers; i.e. for a measurement of N photons the shot noise is approximately $\sqrt{N}$, which means the SNR is also $\sqrt{N}$.

One final type of noise to consider is from the inhomogeneity of the camera, which might be caused by imperfections in the sensor causing variation in band structure that can affect both quantum efficiency and thermal noise, or simply by dirt on the surface

causing different levels of attenuation. Generally this effect is negligible provided the sensor is kept clean.

We can first reduce these sources of noise as much as possible by cooling the camera to reduce thermal electrons, using the slowest available readout speed on the camera to reduce electrons generated during the readout process, and maximizing the signal level for improved SNR of the shot noise. The readout noise can then be estimated by taking a zero second exposure, for which there should be no EUV signal and the thermal noise is minimized. We then take one short and one long exposure, from which the dark noise can be estimated assuming it follows a linear relationship with exposure time. We can then subtract the noise from the data to increase the SNR.

4.3.2.3 High Dynamic Range

We can improve the SNR of our data by taking longer exposures to increase signal strength. However, each pixel in the camera only has a finite well depth, which puts a limit on the dynamic range of a single exposure. Once the charge capacity has been reached, the pixel saturates, and any additional charge that accumulates flows into adjacent pixels. This can also lead to streaking effects in a CCD as the excess charge is shifted along a row of pixels causing further saturation elsewhere, as can be seen in figure 4.7. This is a particular issue in diffraction imaging where the central spot of each collected pattern is usually the brightest by far, perhaps by several orders of magnitude compared with the highest collected spatial frequencies (depending on the object and collection NA). Ideally, we want to maximize the counts to measure the high spatial frequencies without losing the central part of the diffraction pattern to saturation, and this can be done with a high dynamic range (HDR) method.

One way to achieve this is to take one short exposure for which the central spot can be measured below saturation, then take a longer exposure with the central spot blocked to measure the outer part of the diffraction pattern at a higher signal level. The intensity values of the shorter exposure image can then be increased to match the scale of the longer exposure, and the two can be stitched together for a high signal image with an improved dynamic range and no saturation. This is conceptually simple, but relies on precise alignment of a beam block to remove the central part of the pattern and introduction of systematic errors during the stitching process.

Another solution is to deal with saturation by post processing the data. In this case several images are taken with decreasing exposures until no saturation is present. The intensity values are then scaled by exposure time as before, and in the longer exposure images the saturated region is estimated. Finally, the images are stitched together to remove the saturated region. This also introduces systematic errors and increases the computational cost, but does not rely on any additional alignment. An example image

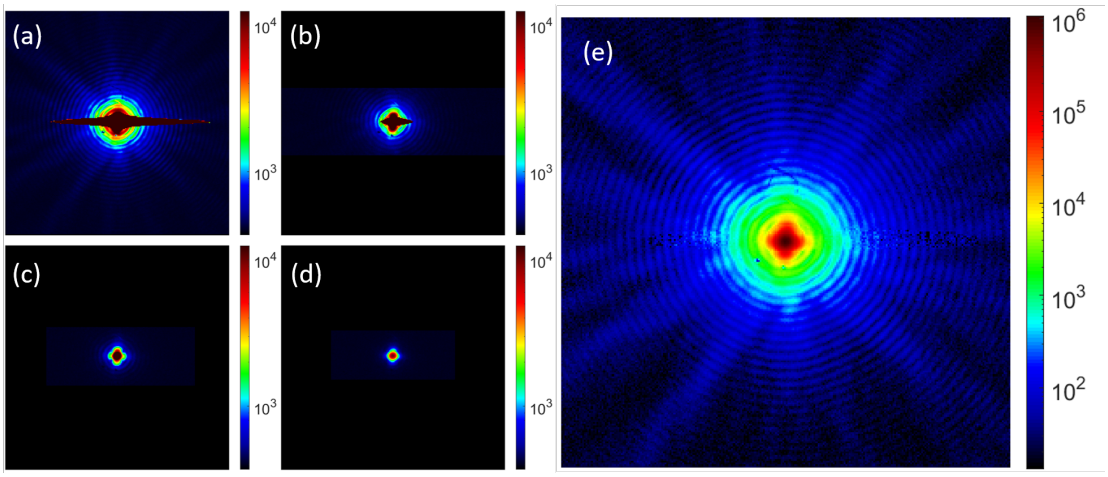

FIGURE 4.7: EUV diffraction through a 10 µm pinhole taken with an exposure time of (a) 2 seconds, (b) 0.0906 seconds, (c) 0.0408 seconds and (d) 0.0269 seconds. The saturated region is very clear at the centre of images (a) and (b), where we can also see the streaking effect the CCD readout has on saturation. The final HDR image stitched together from images (a-d) is shown in (e), where the high spatial frequency information is well defined whilst the saturated area has been removed.

is shown in figure 4.7, where the final HDR image has been stitched together from four images with different exposure times.

4.4 EUV Beam Characterization

The primary objective of this section is to characterize the EUV beam parameters and recognize the variables in the experiment that affect them. However, building a full theoretical model that captures the various mechanisms of HHG and propagation to complement the experiments in this section would be an enormous undertaking. Instead, the focus will be on empirically finding the experimental parameters that get us into a regime of flux and coherence properties in which we can do coherent imaging successfully. The efforts made to measure how these properties depend on generation conditions allow us to choose an EUV mode specifically for imaging experiments; this combined with careful control of EUV beam stability maximizes the chance that ptychographic imaging data will reconstruct. As a result, the work in the following sections plays a key role in the success of imaging experiments in this work.

4.4.1 Transverse Mode

There are several experimental effects that change the spatial profile of the EUV beam produced by our system. Whilst we do not require any particular profile to do coherent imaging successfully, there is an intimate connection between the shape of the transverse EUV mode and the generation conditions that give rise to it. This in turn will affect

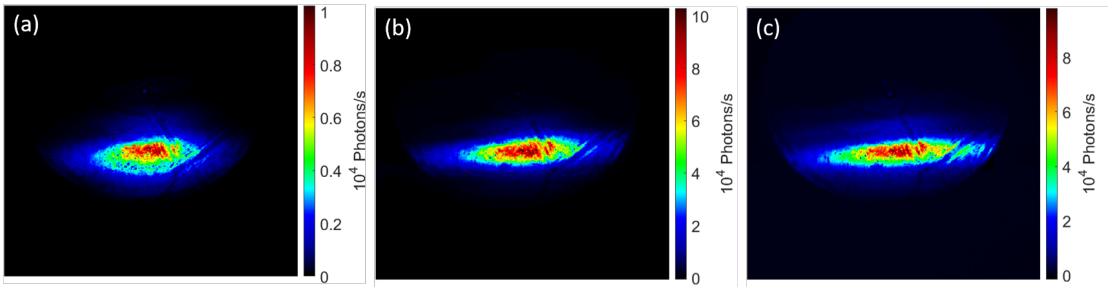

FIGURE 4.8: Far-field EUV beam profile taken before focusing mirror in figure 4.6 at an IR lens position of (a) 49 mm, (b) 47 mm and (c) 45 mm; the input power was 1.4W for each. We note the elliptical beam profile, with an aspect ratio that varies with the generation conditions.

how long and short HHG trajectories contribute. This means that whilst the flux is a simple measurement, we can use the shape of the beam profile to provide an indication for the coherence, which is more difficult to measure directly.

As discussed in 2.2.3, phase matching in HHG depends on a number of factors. In our low gas pressure geometry, the most significant contributions come from the Gouy phase of the fundamental laser as it is focused, and the atomic phase. The latter is defined mainly by the intensity and frequency of our laser, so varies with input power and pulse length. The Gouy phase can be chosen by shifting the focus position relative to the gas cell; this is the most important tool for picking the best EUV mode, because it lets us select the phase matching regime mapped by figure 2.7.

To look at the effect of intensity and Gouy phase variation on the EUV mode, the transverse profile was measured at five different input powers in steps of 0.1W and five different lens positions in steps of 1 mm relative to the gas cell. For reference, the confocal parameter of the IR beam was ∼2 cm, and the IR focus is positioned at the centre of the gas cell when the lens is at 45 mm - here increasing values for lens position means shifting the IR focus counter to the beam propagation direction. Figure 4.8 shows three of the EUV beam profiles at 1.4W input power and lens positions separated by 1 mm each. We can see here that firstly the flux varies significantly as the IR focus position is shifted, indicated by the order of magnitude difference in peak counts between (a) and (b). Secondly, the beam has an elliptical shape that becomes more eccentric close to the IR focus. Both of these effects are investigated in more detail in figure 4.9. In (a), the flux variation with lens position at different powers is shown, from which we can see that for each input power there is a 'sweet spot' for which the flux is maximized at a specific lens position. (b) Shows that the flux continues to increase with input power, suggesting there is negligible fundamental beam depletion and low fraction of ionized gas atoms in the generation volume. However, (c) and (d) show that the aspect ratio, measured as the ratio between the horizontal and vertical FWHM in intensity, and it is clear that the ellipticity gets more extreme at higher input power and closer to the IR focus.

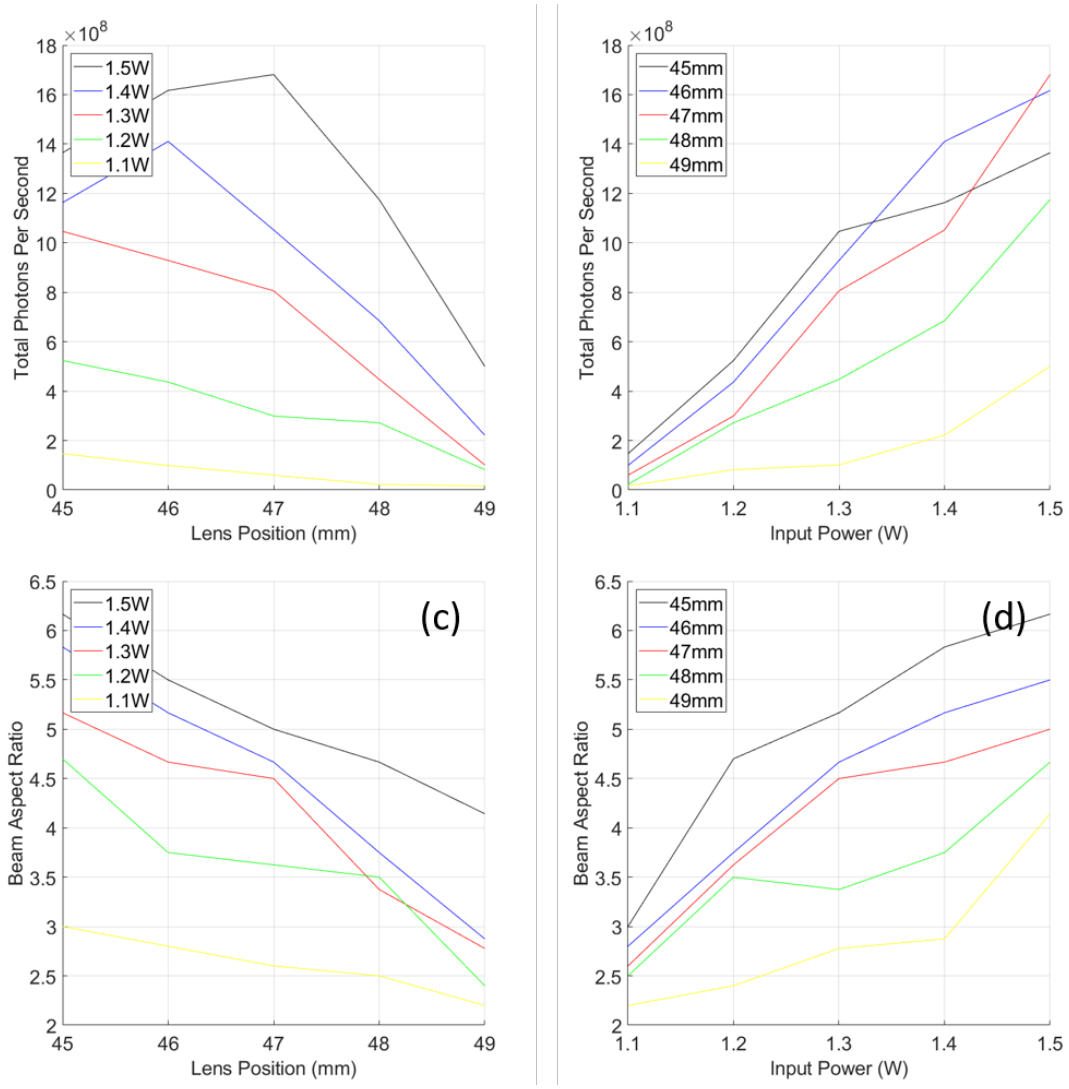

FIGURE 4.9: Top two images are total EUV flux measured on the CCD, showing (a) the effect of lens position at a given input power and (b) the effect of different input power at a given lens position. The bottom two are the ratio of horizontal to vertical FWHM in intensity, showing how this ratio changes with (c) lens position and (d) power.

One possibility is that this beam shape is caused by the IR profile near the focus. The far field IR beam is circular, but as figure 4.4 shows, the minimum beam waist in the horizontal and vertical directions occur at different z positions. If the IR beam at the focus is vertically elliptical as shown in 4.9(b), the generated EUV spot would also be vertically elliptical at the focus, and we might expect the far field high harmonic spot to be horizontally elliptical. However, this would not explain why the EUV aspect ratio increases as the IR focus is brought closer to the gas cell, which is clearly the case.

The non circular IR profile near the focus does not seem to be caused by astigmatism, because it cannot be corrected by tilting the lens. This phenomenon may be better explained by considering higher order TEM modes in the fundamental beam, which we know exist since the M^2 parameter is greater than 1. As we can see from equation

4.2, the Gouy phase shift is increased for higher order TEM modes. As a result, the phase matching regime for higher orders should be closer to the beam waist than the fundamental; this should produce an elliptical beam if there is a large amount of TEM_{01}, for example, and we would expect gain at TEM_{01} to be favourable in the amplifier if the pump beams from each end of the cavity are slightly misaligned. If this is the case, we should expect the coherence to not only be affected by the amount of each HHG trajectory is efficiently phase matched, but also the number of TEM modes that are significant.

4.4.2 Focal Spot

The far field spot can give us some useful information about the state of the EUV beam. However, what we really need to know is the near field profile, which combined with the aperture gives us the EUV probe in imaging experiments. Unfortunately the minimum beam waist of the EUV beam after focusing by the multi-layer mirror is comparable to the CCD camera pixel size, which means we cannot measure the near field profile directly. However, we can use an aperture to look at intensity transmission, convolution and shape of diffraction pattern from which we can extract some information about the beam shape at the focus.

First, we produce a model of the EUV beam to give an idea of what to expect from experimental data. This involves approximating the EUV beam inside the gas cell as a fundamental Gaussian beam described in 2.21 with a flat phase. We then use ABCD matrices to propagate the beam from the cell to the focus in the imaging chamber. This means propagation in free space to the mirror, followed by off-axis focusing, then propagation in free space to the aperture plane. At this stage any aperture can be added, after which the beam can be propagated to the far field via a 2D FFT to calculate the diffraction pattern. This gives us a simulation of the beam in the near and far field to compare with experimental data.

The reason ABCD matrices are required here is to simulate the effect of off-axis focusing. The incidence angle θ of the beam with the spherical mirror reduces the horizontal focal length by a factor of $\cos(\theta)$ and increases the vertical focal length by the same factor. This results in two line foci with a 'circle of least confusion' (CLC) roughly half way between them, where the beam is approximately circular and most intense at small θ, and the wave front is saddle-shaped. Though the angle of incidence in our case is small, $\sim 3.5°$, the effect of off-axis focusing is significant. Figure 4.10 shows the simulated Gaussian beam radius of the EUV beam as it propagates from the gas cell to the focus in the imaging chamber via the off-axis mirror. The input variables were set to match the experimental parameters, with 29.4 nm wavelength and 40 µm spot size to match the IR focus; in reality, we expect the EUV spot size to be much smaller due to the shorter wavelength, the EUV spot size was not directly measured. Also, the purpose

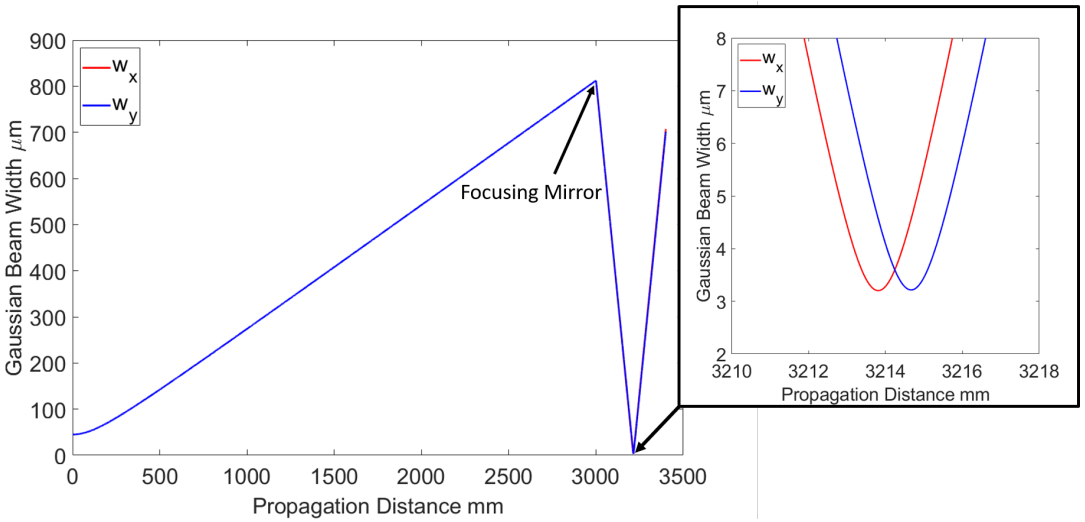

FIGURE 4.10: Simulation of embedded Gaussian EUV beam width in horizontal (w_x) and vertical (w_y) directions as the beam propagates from the gas cell to the focus in the imaging chamber; the inset is a zoomed region to highlight the separate horizontal and vertical beam foci as a result of the off-axis mirror at a 3.5° incidence angle.

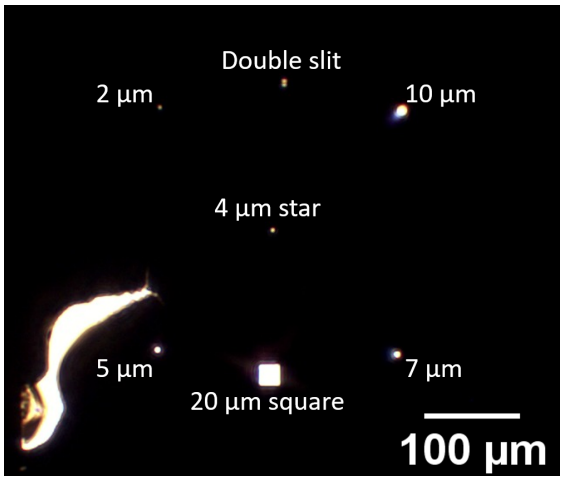

FIGURE 4.11: Optical transmission microscope image of an aperture membrane produced by Stuart Boden at the University of Southampton and used for EUV characterization and ptychographic imaging experiments. This sample has 2 µm, 5 µm, 7 µm and 10 µm diameter circular pinholes, with a 20 µm width square, ∼4 µm diameter star shape and double slit sample with 1x5 µm slits separated by 4 µm. The additional shape in the bottom left is damage caused by the IR laser focus.

of this simulation is to provide an understanding of what happens at the EUV focus due to off-axis mirror effects rather than produce an accurate quantitative model of the EUV characteristics. Given these inputs, there is a separation between the horizontal and vertical foci of ∼1 mm.

The effects of off-axis focusing are also clear in the far field diffraction pattern through a circular aperture. To measure this, a 200 nm Au coating was deposited on a 50 nm thick SiN membrane, and a number of different apertures produced with a focused ion beam (FIB); an optical transmission microscope image of an example aperture membrane

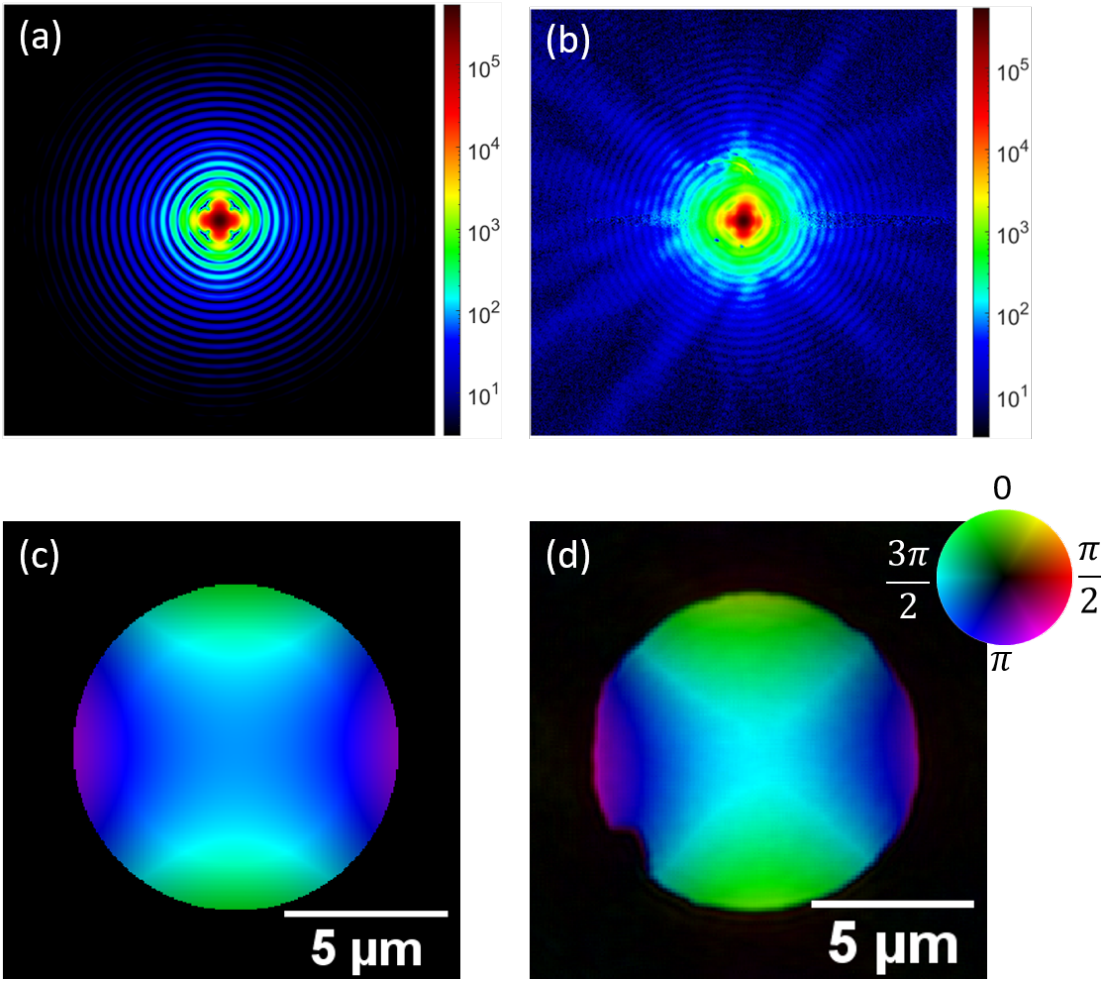

FIGURE 4.12: Comparison between simulated and measured/reconstructed data for the EUV beam propagating through a 10 µm pinhole; (a) shows the simulated far field diffraction pattern, (b) is a real collected diffraction pattern at the same scale, (c) is the simulated near field at the pinhole plane and (d) is a reconstructed probe from ptychographic imaging data. For the probe images in (c) and (d), the image brightness represents electric field amplitude and the colour represents the phase, as indicated by the colour wheel inset in (d).

manufactured by Stuart Boden at the University of Southampton is shown in figure 4.11, with 2, 5, 7 and 10 µm diameter circular pinholes, 20 µm width square, ∼4 µm diameter star shape and double slit with 1x5 µm slits separated by 4 µm. The additional feature in the bottom left of the image is damage caused by the IR laser at the focus during alignment, after the sample was received. This type of membrane was used for beam characterization as well as the aperture for imaging experiments.

Figure 4.12 shows a comparison between simulated and experimental data for the near and far field EUV beam transmission through a 10 µm pinhole; (a) shows the simulated far field diffraction pattern measured by our CCD at a distance of 40 mm away, and (b) shows the real collected data at the same distance for comparison. The other experimental parameters used were the same as used in figure 4.10 to describe the embedded Gaussian, and an M^2 parameter of 5 to reflect the empirically determined beam quality

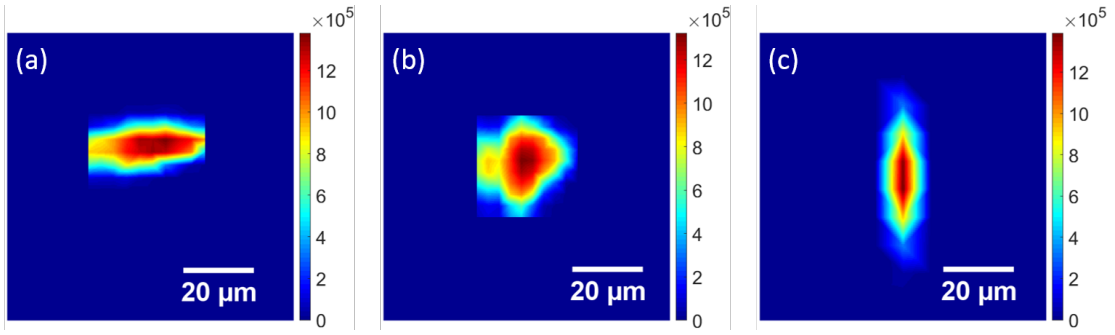

FIGURE 4.13: 2D convolution between the EUV beam and a 10 µm pinhole measured at three axial positions separated by 1 mm each, at (a) the vertical focus, (b) the CLC and (c) the horizonal focus position.

based on knife edge measurements performed by previous student Peter Baksh. The most notable feature is the distinctive cross shape at the centre, which is caused by the saddle phase at the CLC - if the phase were flat the pattern would be radially symmetric. This also provides a useful indication for the optimal pinhole position, since the cross becomes noticeably deformed if the pinhole is axially misaligned with the CLC by $<$100 µm, or transversely misaligned with the beam axis by $\sim$1 µm; by comparison the unstable intensity makes it very difficult to spot changes in power transmission within this level of accuracy.

Also shown in figure 4.12 is the electric field at the aperture plane, with (c) the simulated exit wave through a 10 µm diameter pinhole perfectly aligned with the CLC, and (d) the reconstructed probe from a ptychographic imaging experiment with real data, after numerical back-propagation by 114 µm to the aperture plane. Similar to the EUV ptychography images in chapter 5, the brightness in (c) and (d) represents electric field amplitude and the colour represents phase, as indicated by the colour wheel inset.

A power transmission scan through a 10 µm pinhole was also performed, involving a total flux measurement at each of a 2D array of aperture positions. This builds a 2D convolution between the beam cross section at a given z position and the pinhole, which contains information about the spot size. Also, this can be repeated at different z positions to look at how the beam waist propagates, as is shown in figure 4.13 for three positions each separated by 1 mm. The convolution has a FWHM of 30 µm at the CLC, with 15 µm FWHM along the short axis for each line focus. By comparison, the ABCD simulation predicted a waist of 9 µm at the CLC, and minimum horizontal and vertical beam waists of 7 µm, based on an M^2 parameter of 5, suggesting the actual M^2 factor may be higher for the EUV mode used here - given the complicated relationship between generation conditions and beam quality, this is not unsurprising. Also, the line foci in the simulation are separated by 1 mm, as opposed to the 2 mm we find experimentally. This suggests that one or more parameters used in the model is inaccurate.

In spite of quantitative errors, the model does show good agreement, particularly in the shape of the focal spot and far field diffraction pattern, which provides useful information about what to expect for ideal conditions.

4.4.3 Coherence Measurements

The long and short trajectories in HHG are not mutually coherent, but since they operate along the same axis they cannot be separated after generation (though they are distinguishable by interference experiments [62, 63]). Competition between the two different trajectories limits the spatial coherence of the output beam significantly where radiation from both trajectories overlap. Fortunately, since the regions that give the most efficient conversion for each within the fundamental beam focus are different, it is possible to select only for short trajectories by choosing the position of the generation medium relative to the input beam. In our case, the focusing lens may be translated relative to the gas cell for maximum spatial coherence. Typically, doing this will reduce the flux somewhat as the long trajectory is intentionally suppressed. However, this is necessary for lens-less imaging applications where the coherence condition is critical.

As was discussed in 2.2.4, the spatial coherence can be defined by the visibility of fringes in a two slit diffraction pattern. Figure 4.14 shows (a) the measured diffraction pattern in a two slit experiment, with (b) a fit of the data to the function

$$I = \frac{I_0}{2}\left[1 + \gamma \cos\frac{2\pi S}{\lambda D}(x - x_0)\right] \mathrm{sinc}^2\frac{\pi W}{\lambda D}(x - x_0)\mathrm{sinc}^2\frac{\pi H}{\lambda D}(y - y_0) \tag{4.7}$$

where γ is visibility, S is slit separation, W is slit width, H is slit height, D is camera distance and (x, y) are spatial coordinates with (x_0, y_0) the centre position of the pattern; this is an adaptation of equation 2.35. In this case the slits had a separation of 4 µm, width of 1 µm and height of 5 µm and the camera was 3.8 cm away. The visibility is 0.8 here. An important note is that the fit works well at the centre of the pattern, but fails to accurately describe the intensity further out; this is due to the additional wavelengths present in the illumination, and the fit function assumes a monochromatic source. The spectrum has been previously determined with a double slit spectrometer using a Tikhonov regularization method by our group [30], but is not necessary to measure spatial coherence.

The pattern given in figure 4.14(a) is what we expect when the generation conditions are ideal for imaging and the double slit sample is well aligned to the EUV focus. We find that the visibility of fringes has a complicated relationship with the EUV mode and the position of the slits relative to the beam. This is to be expected, as the spherical EUV mirror effectively images the generated EUV at the gas cell to the EUV focus where the slits are located. This means that as the slits are moved with respect to the beam, we

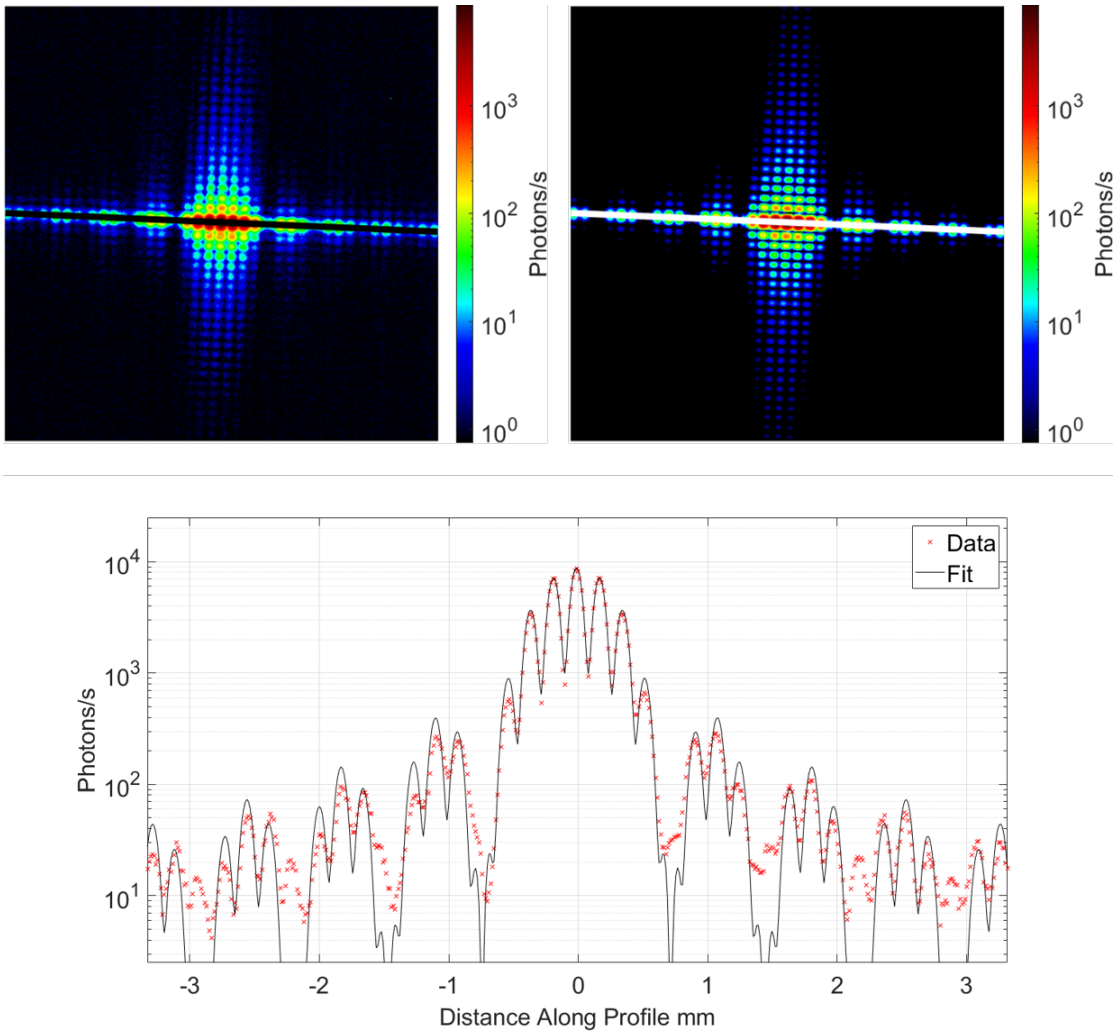

FIGURE 4.14: A two slit visibility measurement of the EUV beam, showing (a) real data and (b) fitted data, with a profile taken along the black line in (a) and white line in (b) plotted in (c).

are sampling a different region in the phase matching map shown in figure 2.7, which also changes with generation conditions.

Though we do not have a rigorous model to fully explain these effects, we find that the spatial coherence is maximized when the EUV mode has the lowest aspect ratio. Figure 4.15 shows three double slit diffraction measurements recorded at a focusing lens position of (a) 49 mm, (b) 47 mm and (c) 45 mm. The data was fit to equation 4.7 for which a visibility of (a) 60%, (b) 29% and (c) 2% was found. Note here that the camera was not cooled for these measurements which has increased the thermal noise background, and we would expect the visibility to be higher than measured here. However, comparing with EUV modes measured at the same lens positions in figure 4.8, it is clear that the spatial coherence gets worse as the beam aspect ratio increases, until the interference fringes have been completely wiped out. This provides a guide for the generation conditions that allow us to image successfully, and has been verified

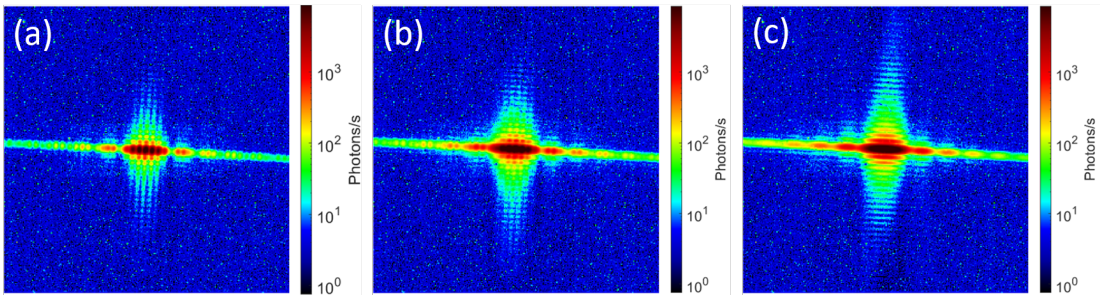

FIGURE 4.15: Double slit diffraction patterns recorded at a lens position of (a) 49 mm, (b) 47 mm and (c) 45 mm, similar to the EUV profiles measured in 4.8. The visibility of each is (a) 60%, (b) 29% and (c) 2%, showing the clear reduction in coherence as the EUV beam aspect ratio increases.

a number of times; if the aspect ratio is too high, reconstructions of the data either become impossible or are greatly reduced in quality.

We also find that the size of the aperture used in ptychography is important, not only for allowing sufficient flux but for removing parts of the beam that do not contribute coherently. Scans taken with a pinhole size of 10 µm or smaller have a high reconstruction success rate with a good EUV mode, but scans start to fail if a larger pinhole is used.

4.4.4 Stability

The short term EUV stability is limited by the position and intensity stability of the IR beam at the gas cell. The position stability is somewhat improved in the EUV beam, because the EUV focus is a demagnified image of the gas cell, with a magnification of ∼1/14. Though the transverse position of the IR focus in the cell shifts across a range of around 10 µm over a few seconds, the near field EUV spot can maintain its position to within 1 µm. However, given the non-linearity of HHG, the intensity fluctuations are amplified; we commonly see intensity variations of 10-15% under optimal conditions.

To measure short term stability, the EUV mode can be measured continuously using vertical binning, from which the horizontal centre of mass position and total flux can be obtained. Figure 4.16 shows such a measurement taken over 60 s; (a) is a continuous vertical binning image of the EUV beam, where each column of pixels is the vertically binned data taken during a 0.1 s exposure, (b) is the total counts in each vertical binning measurement, and (c) is the centre of mass position in each. The cross sections in (a) show the variation of the shape and position of the EUV mode. The total counts in (b) show an intensity variation of 10-15%, and the centre of mass position in (c) shows a variation in the beam position in the range of 6 pixels, or 78 µm. Intensity and position fluctuations in this range are acceptable for imaging. Increased instability can deteriorate the image quality and reduce the chance of a convergence in ptychography;

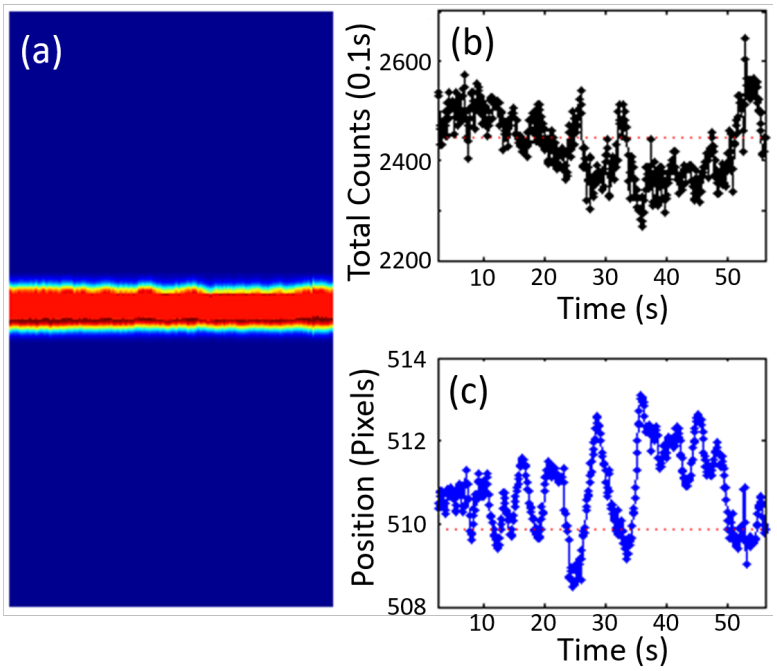

FIGURE 4.16: Far field EUV stability during a 60 s measurement, with (a) a vertically binned image showing summed counts along each column of the CCD which indicates how the shape of the mode changes, (b) total counts during a 0.1s exposure indicating flux variation of 10-15%, and (c) centre of mass position showing position stability within a range of 78 µm.

we have observed intensity fluctuations of ±100% in extreme conditions, which makes beam characterization and imaging impossible.

Over longer time scales, the stability issues can be much more significant. Again the position is related to the IR position, which can be corrected with our active stabilization system. The flux variations are much more problematic and a cause for reduction in image resolution where the flux decreases during a scan. There are two main causes for long term flux decrease. First, the various equipment that needs to run in the lab during an experiment generates heat, and increases the temperature by 2° over several hours. This can double the IR pulse length, which reduces EUV flux by an order of magnitude or more. We find that this can be corrected manually every 10-20 minutes during a ptychography experiment with no adverse effect on image quality. The second cause is a build up of ice on the surface of the cooled CCD from residual water in the vacuum chamber, which attenuates the EUV before detection; this results in a characteristic exponential decrease in scan flux, suggesting a linear build up in thickness of the ice layer. Again, this can cause decrease in flux by an order of magnitude, which can be greatly reduced by decreasing the total surface area of objects in the chamber for water to cling to, and by pumping down for long periods (several days) to lower the water vapour pressure as much as possible.

We can measure long term flux changes by summing the counts on the CCD during an

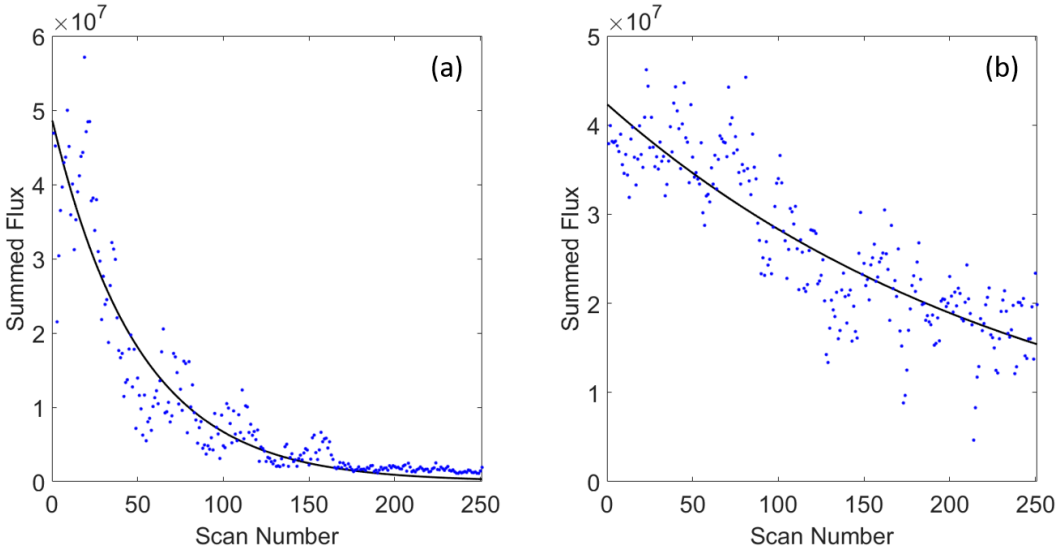

FIGURE 4.17: Comparison of summed counts at each scan position for two ptychography data sets. Each data set consists of 251 scan positions, which took ∼3 hours to collect. The blue dots are the individual data points and the black curve is a fit to an exponential decay.

imaging experiment; whilst the counts will also vary based on object transmission, the effect of EUV intensity decrease is obvious, particularly when imaging sparse samples. Figure 4.17 shows the summed counts at each scan position during a ptychographic imaging experiment for which 251 diffraction patterns were collected over a period of ∼3 hours; the black line in each is a fit to the exponential decay function $y = a\exp(-bx)$. The data in (a) was collected after pumping down for ∼2 hours, compared with pumping down overnight in (b). The effect on flux decrease is obvious; the decay constant b is 5 times larger in (a) illustrating a sharped decline in flux due to the more humid camera environment.

4.5 Summary

In this chapter, the laser system used to generate EUV radiation was described, with various diagnostics used for IR characterization, including pulse length, position stability and M^2 parameter measurements. This is important for HHG, since it is such a highly nonlinear technique, and any lack of stability or quality of the fundamental beam is amplified in the EUV output.

The experimental set-up used both for EUV characterization and ptychographic imaging was outlined, with the equipment used at each stage. In particular, the detector type is discussed, along with the techniques to reduce sources of noise and increase SNR as much as possible and a method for improving the dynamic range. This is significant in lensless imaging applications where the SNR is intimately connected to the available resolution.

Finally, the coherence, stability, flux and mode shape of the EUV beam were measured and their variation with generation conditions examined. From this, a model of the EUV beam propagating through the system was built to examine the shape of the focal wave front and far field diffraction and the effect of off-axis focusing from the EUV mirror, which was compared with empirical results. The main aim of the work in this section was to find a regime of generation conditions that gave rise to an EUV mode with optimal properties to maximize the chance of successful, high quality reconstructions; the success of the results in chapter 5 demonstrate the beneficial outcomes of these efforts.

Chapter 5

Ptychographic Imaging

This chapter details the ptychographic imaging experiments performed with the EUV source developed at the University of Southampton and contains the most impactful research of this project. To the best of our knowledge, the images of biological samples from our group are still the only examples of ptychographic imaging of real rather than man-made samples using a table-top high harmonic source. Though the technique had been successfully demonstrated previously, the quantitative measurements on image correlation and EUV damage is new work that shows great promise for biological imaging applications.

In the following sections, all of the imaging data was collected by myself unless otherwise specified, and reconstruction work performed by Bill Brocklesby and Haoyan Lu from our group, and previous student Michal Odstrcil.

5.1 Imaging Details

The setup used to acquire data for ptychographic imaging has already been discussed in 4.3.1. The aperture is placed at the focus of the EUV beam where it remains for the duration of the scan, and the sample is shifted relative to the aperture to get a diffraction pattern from each probe position along the scan path. We use a spiral path to give the best overlap between probe positions, and we can choose the particular parameters of any scan, including step size to set the overlap ratio based on the pinhole size and scan range to define the extent of the reconstructed object. We can also change the acquisition settings of the camera. It typically takes 2-4 hours to acquire a data set for a single 30 by 30 µm region, so many of the parameters are chosen to reduce the scan time as much as possible whilst meeting the stringent requirements of coherent imaging.

Once the data has been taken, a ptychographic algorithm is used to reproduce an image via the techniques discussed in 3.2.4. It is important to have experimental parameters

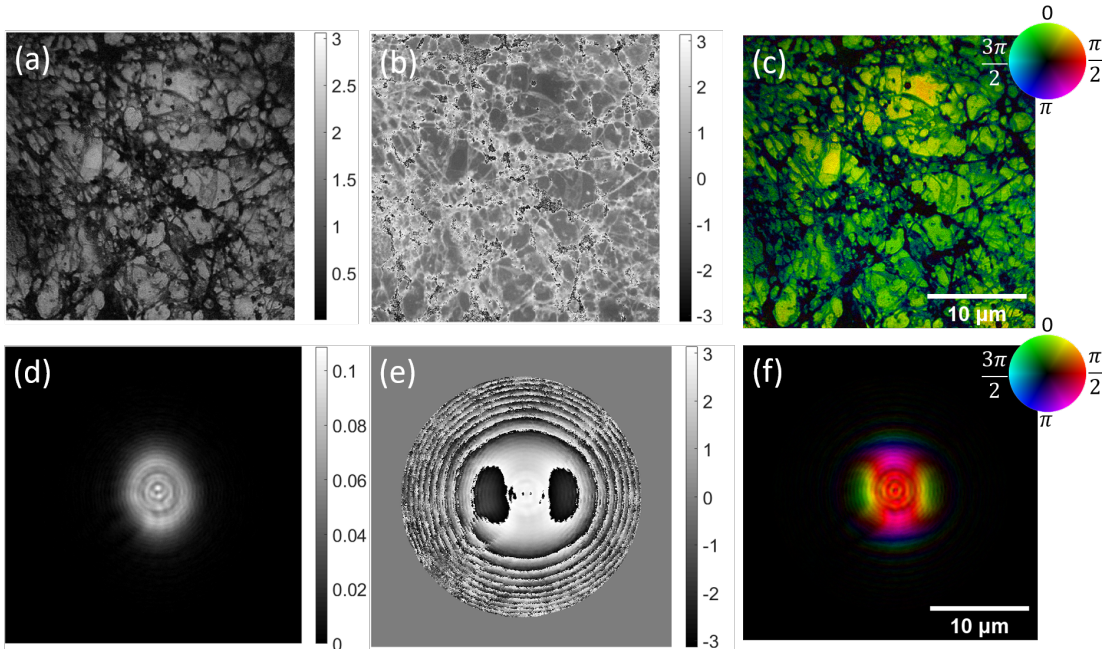

FIGURE 5.1: Demonstration of how ptychographic images are shown in this work; (a) shows object relative amplitude, (b) shows object relative phase and (c) is an HSV image in which brightness represents amplitude and colour represents phase, as indicated by the colour wheel inset. The probe is represented in the same way in images (d-f).

such as probe-to-sample and sample-to-camera distance defined accurately to get the reconstruction process started, after which the scaling factors can be optimized during the algorithm to minimize the error.

Ptychography reconstructs the full electric field of the object, which means we can display the amplitude, phase or intensity in the image. Alternatively, we can use the image brightness to represent amplitude and colour to represent phase, such that the full information is displayed in a single image. An example reconstruction of a neuron sample is given in 5.1, where (a) is the reconstructed amplitude of the object, (b) its phase, and (c) a combined hue saturation value (HSV) image, where brightness shows amplitude and colour shows phase, as indicated by the colour phase inset. Since the electric field is also reconstructed for the illumination, we can also represent the probe in this way, as shown in (d-f).

5.1.1 Choosing a scan region

Once the aperture is aligned to the EUV beam, in order to choose the scan position for an image, we first take an intensity map by measuring the total transmission at each sample position. This is a similar measurement to those done in 4.4.2, and show the convolution between the sample and illumination probe. Figure 5.2(a) shows a visible phase contrast microscope image of a neuron sample, and (b) shows the EUV intensity map on the same scale. Under careful inspection, it is possible to match the features of the transmission

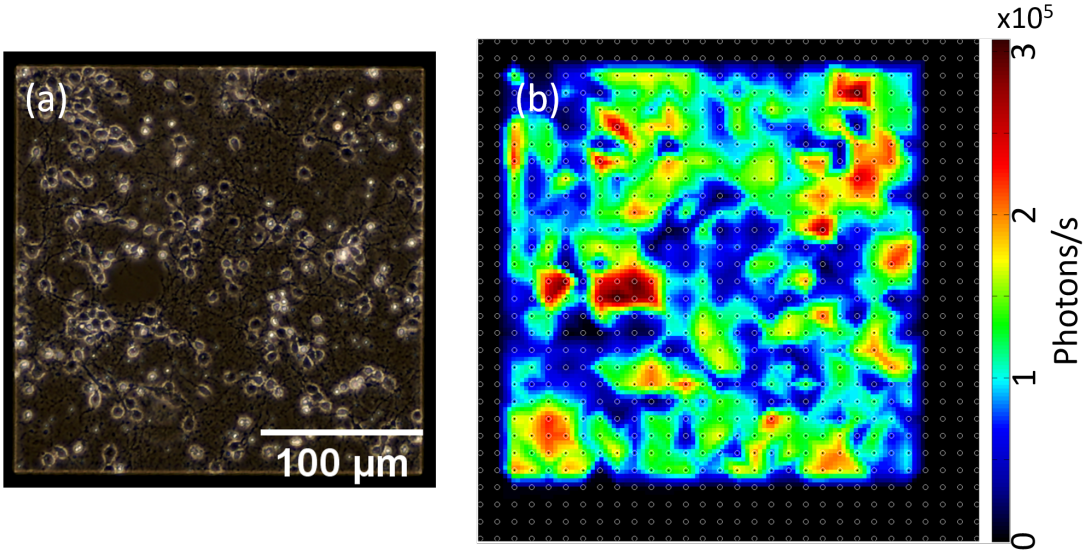

FIGURE 5.2: (a) visible phase contrast image of a neuron sample, with (b) an interpolated EUV transmission intensity map of the same sample, shown on the same scale. The circles on the transmission map show the positions of each intensity measurement during the scan.

map to the features in the microscope image, however this is only possible when the EUV intensity is very stable. Fortunately, the position of the transmitting window is obvious, and provides a simple way to correlate the position of the transmission with the microscope image, provided the orientation is known. This allows us to quickly choose a region of interest on the sample to image with EUV ptychography.

5.2 Test Sample Imaging

All lensless methods that use some iterative algorithm to produce an image rely on the accuracy of the constraints, which implies that not all objects will be equally straightforward to reconstruct. Highly scattering samples provide more diversity in the data, since more information is available at higher spatial frequencies; samples that interact weakly with the illumination or have limited variation or structure are much more difficult to image. Also, samples that have a highly regular or periodic structure across the entire region of interest can cause unique problems, as we will see shortly. For this reason, ideal samples for ptychography exhibit strong scattering and some structural randomness. For a given experimental geometry, we can use an 'easy to image' sample to provide an accurate guess for the probe, which can then be used as an initial guess for other samples to be imaged with the same experimental parameters. Starting with a well-defined probe greatly improves the chance of a convergence as well as quality of the final image.

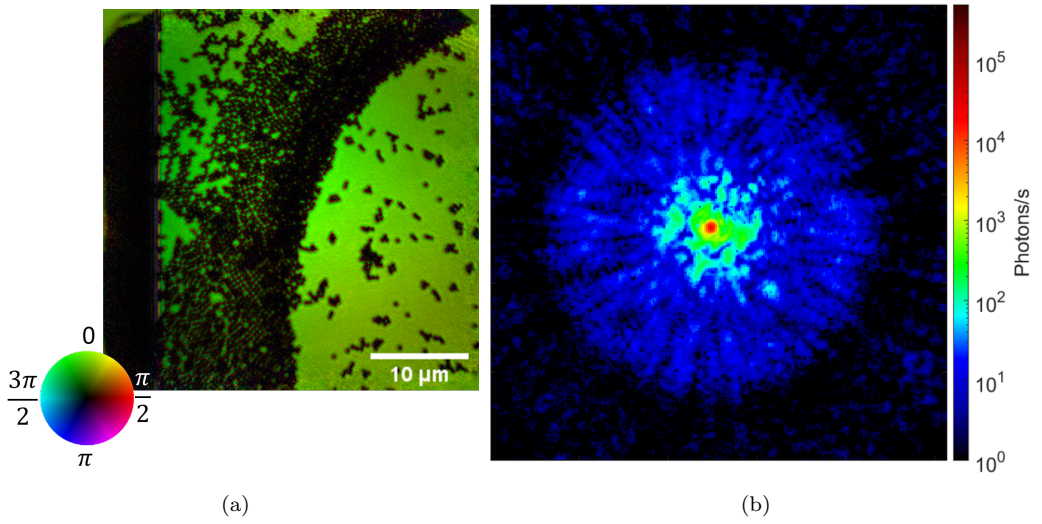

(a) (b)

FIGURE 5.3: (a) Reconstruction of PMMA spheres sample with (b) collected diffraction pattern from a single scan position.

For an ideal and easy to manufacture sample, we deposited a solution of poly(methyl methacrylate) (PMMA) spheres of $\sim 600\,\text{nm}$ diameter onto a 50 nm thick Si_3N_4 support. This allows a controllable density of high contrast features; the attenuation length of Si_3N_4 at 29 nm is less than $0.03\,\mu\text{m}$. Also, the spheres tend to clump together in some regions and spread more sparsely in others, which gives good structural variation. Figure 5.3 is an example reconstruction of a PMMA spheres sample which illustrates the level of amplitude variation across the region of interest, with a single collected diffraction pattern from the scan which shows the high level of scattering that we want for a strong convergence.

5.2.1 EUV Probe

The probe that illuminates each position of the object in a ptychography scan can have a significant effect on the quality of the reconstruction. It should be spatially and temporally coherent, and small enough to fulfill the oversampling constraint. However, there is no strict requirement on its amplitude and phase profile; in fact ptychography has been used for beam characterization in a number of applications, able to recover illumination properties including intensity profile and wave front shape [64, 65], evolution in time [9], spectrum [66], and coherence [59]. This is useful in our case, where the off-axis mirror effects and beam ellipticity mean the amplitude and phase are not well known in advance, and the HHG process results in some lack of stability and coherence.

A more subtle but important aspect of the probe is the roughness of its intensity profile [67, 68], or how highly structured it is. The measured diffraction intensity at a given scattering angle depends on the spatial frequency spectrum of both the object and illumination; using a smooth probe does not fundamentally limit the resolution of the

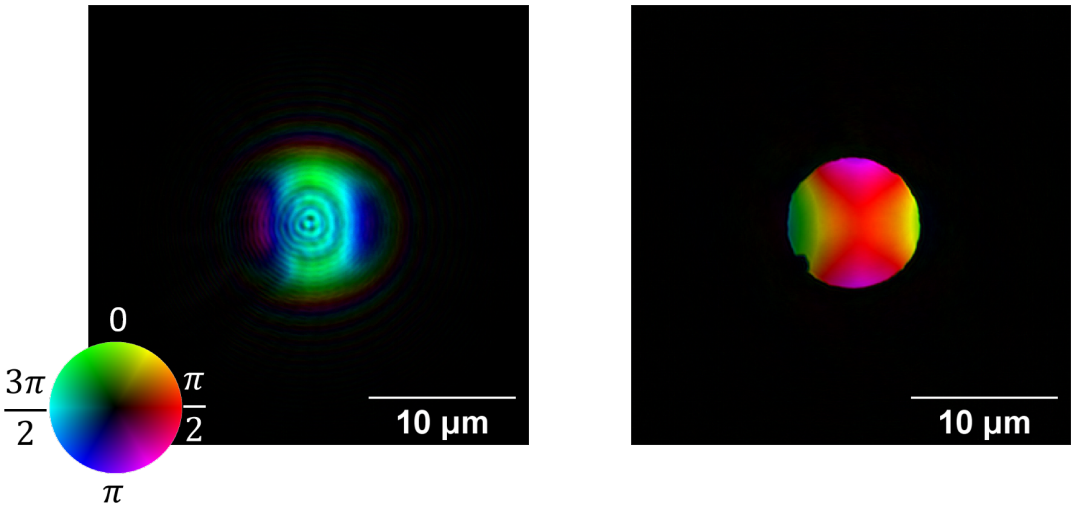

(a) (b)

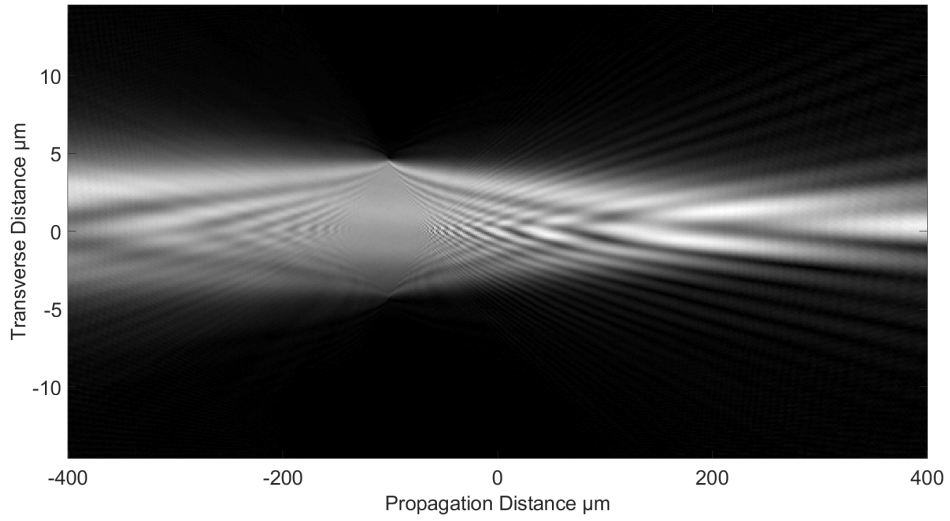

(c)

FIGURE 5.4: Reconstructed EUV probe (a) calculated in the object plane via ptychography and (b) numerically back-propagated by 101 µm to the aperture plane; (c) is a vertical profile of the probe amplitude propagated to various distances, from which the best aperture position can be obtained. The details shown in the fringes in the object plane give an indication that this probe is well defined; this is reflected in both the saddle phase shape and the rough edges of the pinhole in the aperture plane.

final image, but can reduce the SNR at higher collection angles, whereas a structured probe with a wide spread of spatial frequencies can assist the algorithm and increase the confidence of the reconstruction at the higher spatial frequencies.

We find that a 10 µm circular pinhole placed at the EUV focus restricts the beam enough to meet the spatial coherence requirement. Using a smaller pinhole further improves coherence, but reduces the total transmitted intensity and requires a smaller step size to achieve the same overlap ratio; both of these result in longer scan times, since the exposure must be increased to maintain the SNR and more diffraction patterns must be collected within the same scan range. Also, the probe exhibits sufficient structure provided the aperture-to-sample distance is short enough; 100 µm is a good target distance.

Figure 5.4 shows a reconstructed EUV probe. Also shown in this figure is the same probe numerically back-propagated to the aperture plane, which was 101 µm away, and a cross section of the probe propagated forwards and backwards within a range of 800 µm, from which the aperture position is clear. The phase variation and fringe detail gives an indication of the reconstruction quality, along with the sharpness of the back-propagated probe. The saddle phase shape also provides information about how well the pinhole was aligned to the beam during data collection.

5.2.2 Limitations of the Algorithm

Ptychographic imaging relies on the ability of the algorithm to reconstruct both the probe and the object. In some extreme cases, the structure (or lack of structure) in the sample can cause issues that make it very difficult to image with this method.

Figure 5.5 is a reconstruction of a very low density sample of mouse hippocampal neurons that were only grown for a single day. In this case, the lack of variation across the object means that there is minimal variation in the measured diffraction patterns, and limited information to find a convergence with. Also, instabilities in the EUV beam intensity and profile can be incorrectly attributed to variation in the object transmission. There are clear aberrations in the object where the reconstruction has failed, reflected in the back-propagated probe where there is intensity outside of the aperture. Generally, the failure is in a lack of information across a wide spread of spatial frequencies; this could be potentially be improved by increasing the structure of the probe or object, for example by using a diffusing optic at the probe or by depositing scattering elements such as the PMMA spheres used as a test sample onto the object.

A different problem is encountered for samples with a highly regular structure, as is illustrated in figure 5.6, which is a reconstruction of a meta material grid manufactured by Dr Bruce Ou at the Optoelectronics Research Centre [69], with an SEM image of the same sample region for comparison. Similar to the issue of sparse objects, the problem seems to be a difficulty in distinguishing between object and probe. In this case, the same

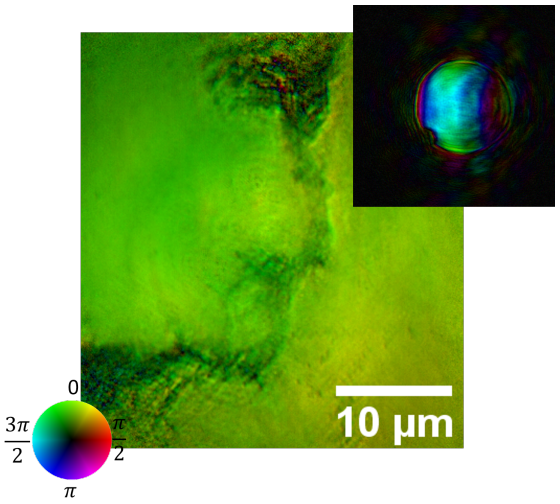

FIGURE 5.5: Reconstruction of a sparse neuron sample with EUV probe numerically propagated to the aperture plane shown on the same scale.

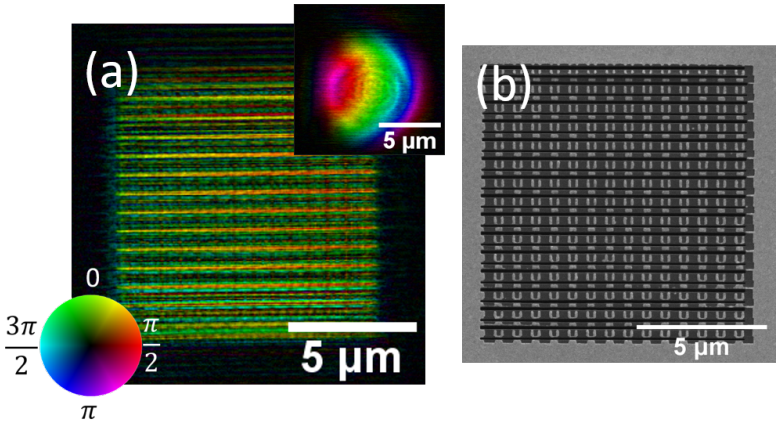

FIGURE 5.6: (a) is a reconstruction of a meta material grid with numerically back-propagated probe inset; (b) shows is an SEM image of the same sample region.

structure exists in the sample region at every collected diffraction pattern with some relative shift, which is incorrectly attributed to the structure in a wobbling probe. Both cases produce artifacts in the final image due to failure to obtain a good convergence.

5.3 Imaging of Hippocampal Neurons

5.3.1 Sample Preparation

The samples examined in the following sections are hippocampal neurons isolated from embryonic day 17 mice, prepared by Dr Katrin Deinhardt from the Biological Sciences department at the University of Southampton. To image these cells with our system, they needed to be dried and fixed to a very thin membrane for vacuum compatibility and to reduce EUV attenuation. To achieve this, 50 nm thick Si_3N_4 membranes were

sterilized and then coated by poly-L-lysine. The neurons were grown in neuronal media for a number of days in vitro (DIV) before being fixed with 4% paraformaldehyde followed by 100% methanol. The sample shown in figure 5.5 was grown for 1 day, but most of the samples we looked at were grown for 7, 14 or 21 days and exhibit a higher density of connections as a result. A fraction of the samples were stained with fluorescent markers, specifically an anti-tubulin antibody and phalloidin, to highlight actin and tubulin structures with fluorescence microscopy.

5.3.2 Image Correlation

Though imaging of biological samples has been previously demonstrated by our group, a simple but significant development in this work is the ability to image a predetermined region of interest with high precision. This has allowed useful collaboration with the Biological Sciences department at the University of Southampton, where a sample may be prepared, a list of potentially interesting regions identified on a wide field fluorescence/optical microscope image, then a number of EUV images of those regions generated. It also allows direct comparison of our technique with more standard methods to highlight specific benefits.

Figure 5.7 shows a wide field fluorescence overview of one neuron sample and overlaid EUV images of three 30 by 30 µm areas, with correlated position, scaling and rotation. The precision stage coordinates allow us to accurately map each EUV image to the transmitting membrane, and here we can see the scale on which we operate compared with standard fluorescence/optical microscopy; in principle data from more scan positions could be taken to provide EUV images with the same field of view, but the time taken to collect data means that in practice we are confined to examine much smaller areas.

5.3.2.1 Object Structure Comparison

The extra detail available from the EUV images is immediately apparent, and is particularly evident when directly comparing similar regions in the object. This is illustrated in figure 5.8, where the EUV transmission intensity is compared with fluorescence microscope images. Here (a) shows the EUV intensity with actin (green) and tubulin (red) fluorescence images superimposed; (b) and (c) are the individual fluorescence images. The resolution is much higher, as an expected consequence of the shorter wavelength illumination. Also demonstrated here is the power of using EUV microscopy to assist in the interpretation of fluorescence images. This can be seen in the red tubulin image in (c), which gives the appearance of a continuous horizontal structure (indicated by the dashed white rectangle); the EUV image clearly shows that this object is much more complex and certainly not continuous.

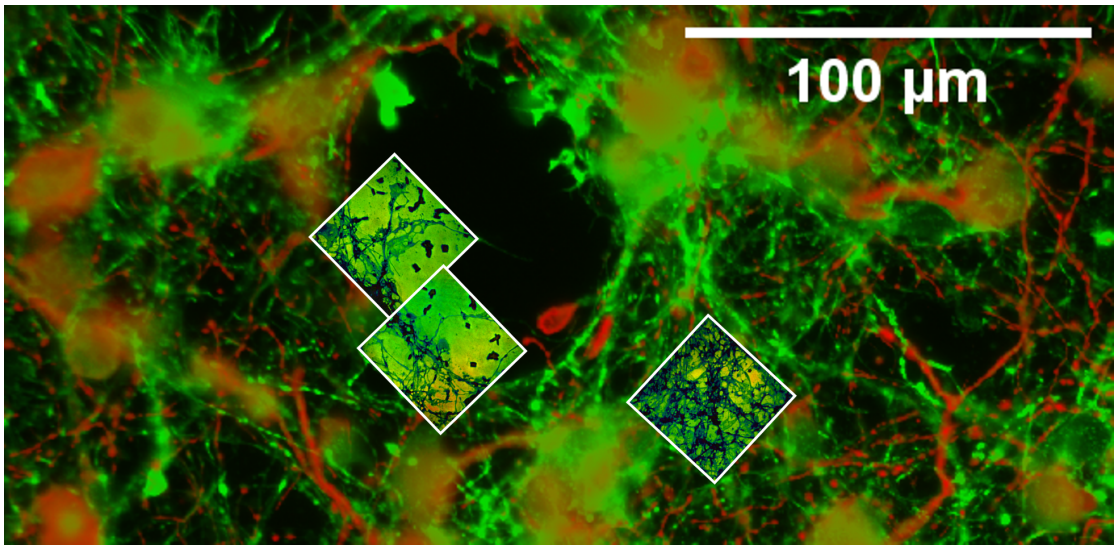

FIGURE 5.7: Comparison of EUV and fluorescence images of DIV7 neurons. The background is a wide field fluorescence image of actin (green) and tubulin (red), and the three smaller images are from EUV ptychography with correlated position, scaling and rotation.

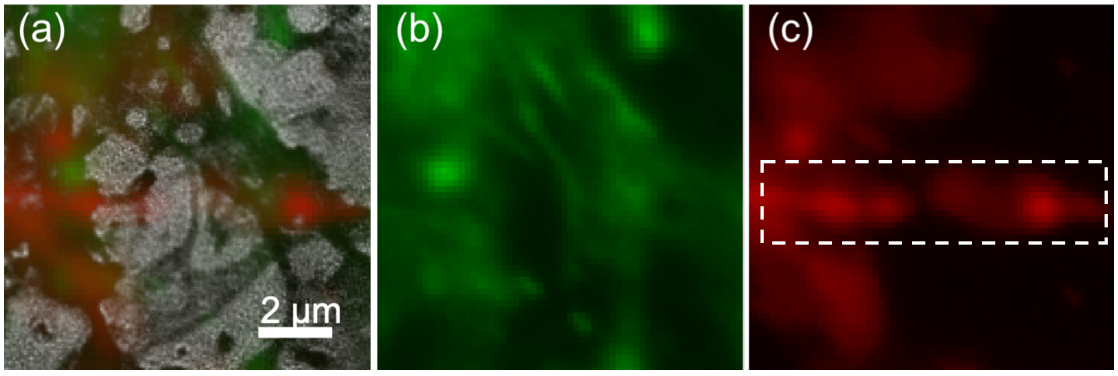

FIGURE 5.8: Comparison of EUV ptychography and wide field fluorescence images of a single region of DIV7 neurons. Image (a) is EUV transmission intensity with superposed actin (green) and tubulin (red); (b) and (c) are the individual fluorescence images. The structure highlighted by the dashed white rectangle in (c) might appear as a single continuous structure; the EUV image clearly shows that it is not. This image was used in [10].

5.3.2.2 Super Resolution Images

There is an increasing availability of super resolution fluorescence techniques that offer impressive resolution improvement beyond the diffraction limit. To compare one of these methods with our techniques, some of the DIV7 neuron samples were imaged using a SIM set up with the OCTOPUS imaging cluster at the central laser facility. This system offers a standard optical and wide field fluorescence imaging set-up with a transverse resolution of ∼200 nm, with optional SIM capability that can allow improvement in resolution of fluorescence images down to ∼100 nm; comparable to the best resolution achievable within the diffraction limit of EUV ptychography at 29 nm.

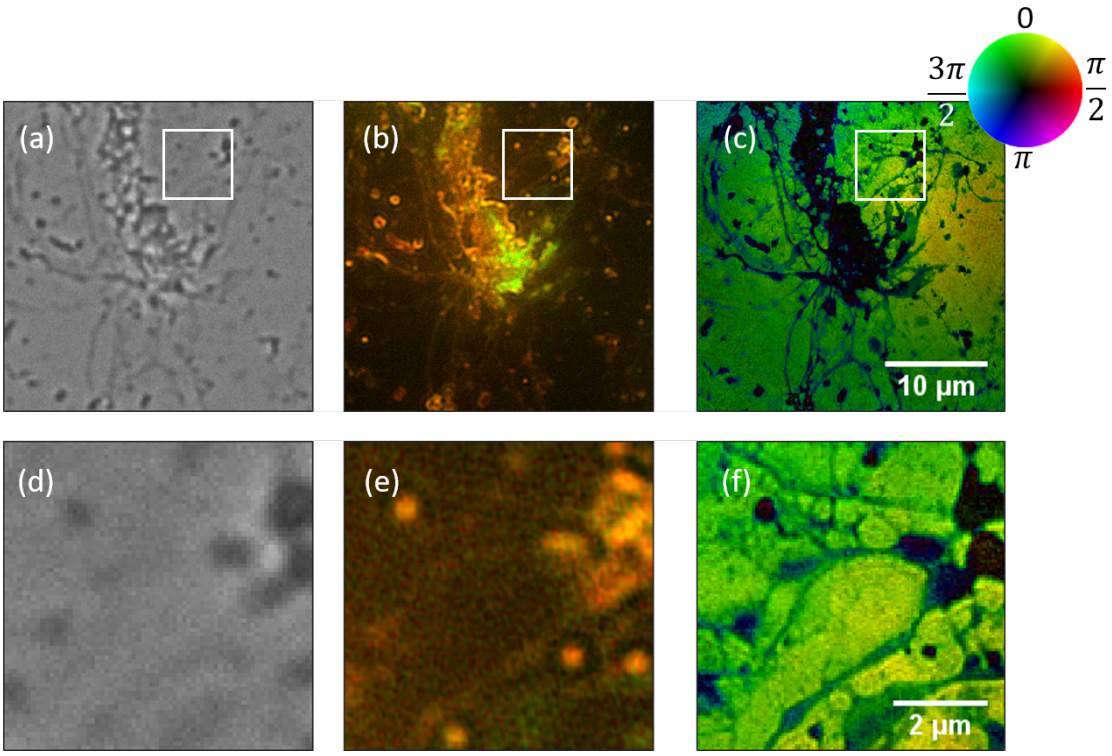

FIGURE 5.9: Comparison of the same region of DIV7 neurons using (a) optical transmission, (b) SIM and (c) EUV imaging; the white boxes indicate smaller areas shown in the corresponding images (d-f). The red and green channels in the SIM images indicate emission intensity from tubulin and actin markers respectively.

A comparison of the optical and SIM fluorescence images from this microscope with an EUV image of the same sample region is shown in figure 5.9; the SIM images were taken with help from senior link scientist Dr Lin Wang at the OCTOPUS facility. The extra detail of our EUV image compared with the standard optical microscope indicates an obvious advantage in resolution. When compared with the SIM image, the issue of fluorescence background is highlighted more clearly than in the previous wide field comparisons, where very thin structures that do not exhibit strong emission due to a lack of fluorophores are lost to background levels. We note that this is a problem common to all fluorescence methods, and introduces the complication of finding the correct density of markers during the sample preparation process. Clearly the same issue does not apply in the EUV, and we see high contrast for even thin features.

5.3.3 Transverse Resolution Estimation

The Abbe limit gives us a quick calculation for the smallest resolvable object, but this theoretical limit may not be reached; a more accurate characterization of an imaging system is given by the PSF, which fully describes how an examined object will appear in the image. However, obtaining the PSF can be a painstaking process, and may not always be possible. This provides a motivation for finding other ways to estimate the

resolution, which could be a simple comparison with a higher resolution image from which a mutual transfer function can be calculated [8], or imaging of a man-made test sample with well defined object shapes and sizes [30, 70]. However, these approaches cannot be used in our case, where we are imaging biological samples with unknown features with no higher resolution reference, and it is therefore preferable to find a self-consistent measurement. A common method is knife-edge [70, 71], for which a sharp feature in the image is fitted to a sigmoid function to estimate the resolution. However, this requires the presence of sharp features in the object, and can give misleading results; for example a sharp feature can have a higher intensity gradient if the image is out of focus. A key point here is that the intimate connection between SNR and resolution means that test objects do not tell the full story, since they can be manufactured to provide strong scattering over any range of spatial frequencies acceptable by the NA of the imaging system, and in general real samples do not.

5.3.3.1 Fourier Ring Correlation

For our imaging system, the best indicator of resolution is Fourier ring correlation (FRC) [72, 73], which is the 2D equivalent of Fourier shell correlation [74] used in x-ray and electron microscopy. This has a close relation to the modulation transfer function, which is the modulus of the OTF. In a ptychographic reconstruction, both the experimental SNR and the reconstruction quality affect the OTF, which determines how information from each spatial frequency component in the object is transferred to the final image, and therefore sets the resolution limit. The principle of FRC is to compare the spatial frequencies between two statistically independent data sets to assess whether a cut-off frequency exists above which no reliable information is available, from which the image resolution can be calculated.

In this method, two images of the same object region are obtained from separate data sets, and their 2D Fourier transforms Ψ_1 and Ψ_2 computed. We then consider a number of concentric rings centred on the zero frequency, and sum the correlation between the two images at each pixel i that falls within ring R_n. The FRC function is defined as

$$\mathrm{FRC}(R_n) = \frac{\sum_{i \in R_n} \Psi_1(i) \Psi_2^*(i)}{\sqrt{\sum_{i \in R_n} |\Psi_1(i)|^2 \sum_{i \in R_n} |\Psi_2(i)|^2}} \tag{5.1}$$

We can see that if the two images are identical, this function is 1 for every ring; in this case the spatial frequencies correlate perfectly up to the Nyquist limit, and the resolution is simply given by the pixel size. In practice, there will always be a decline in correlation at higher frequencies, and we must define a criterion to determine the cut-off point where the FRC drops below some value. A few different criteria have been proposed; we have used the half bit criterion [75] defined as

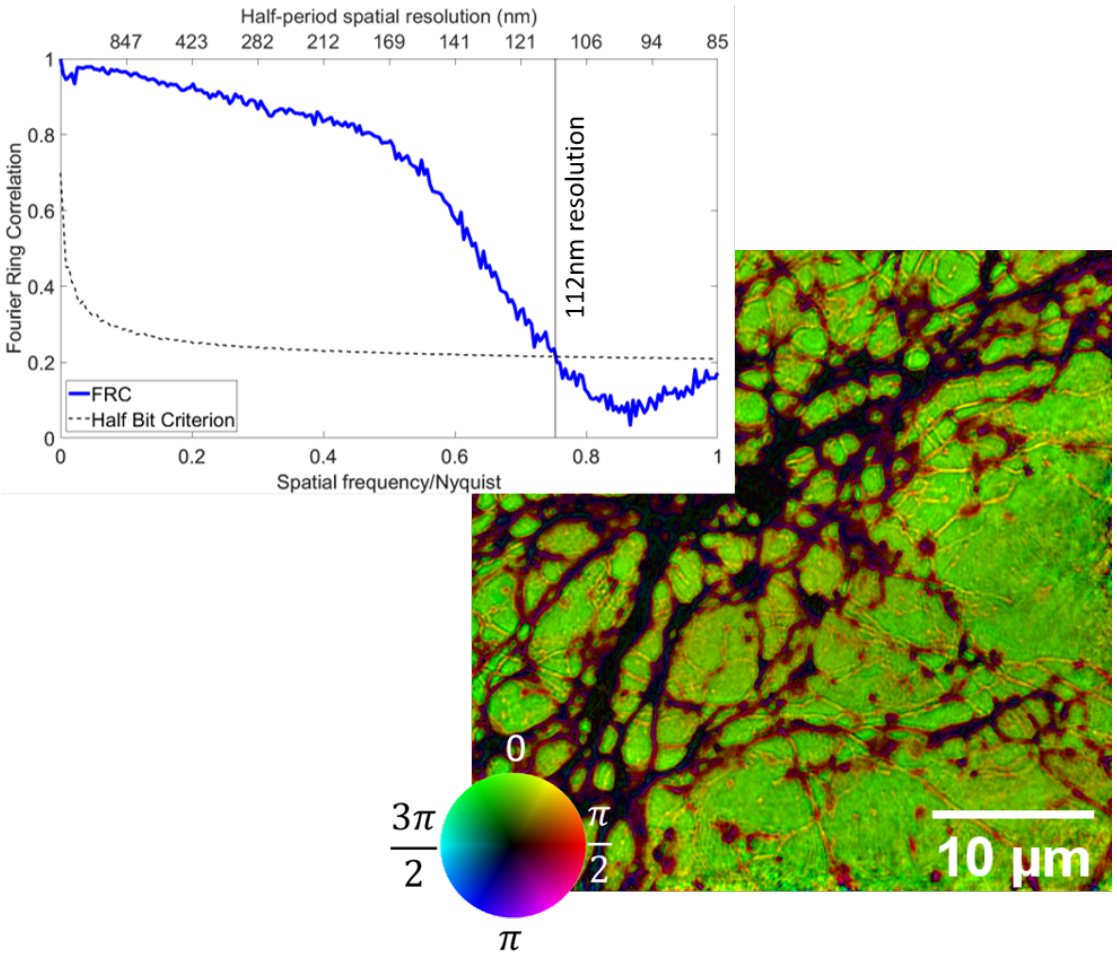

FIGURE 5.10: One of two reconstructions of DIV7 neurons obtained by two independent data sets, and the FRC between them. The calculated pixel size in the image is 85 nm, and the intercept with the half bit criterion is 0.75 of the Nyquist limit, suggesting a transverse resolution of 112 nm.

$$T_{1/2}(R_n) = \frac{a + (2\sqrt{a} + 1)\,/\sqrt{N_p(R_n)}}{1 + a + 2\sqrt{a}/\sqrt{N_p(R_n)}} \tag{5.2}$$

where N_p is the number of pixels within each ring and $a = \frac{1}{\sqrt{2}} - \frac{1}{2}$ in the half bit case.

An FRC can be taken between two reconstructions of the same data with a different random initial object phase, or even on a single image by splitting the pixels into image pairs [76], though this would be more a test of the reconstruction process than the imaging system as a whole. For a faithful representation of the actual resolution capability of our system, there can be no correlation between the underlying systematic errors of each image; for example if the same collected diffraction patterns are used to generate two separate reconstructions the instability of the illumination will be identical for both, and the experimental limitations are somewhat neglected. The best way to ensure this is to take two independent data sets of the same sample region and reconstruct each, then calculate the FRC of the two resulting images; figure 5.10 shows the FRC between

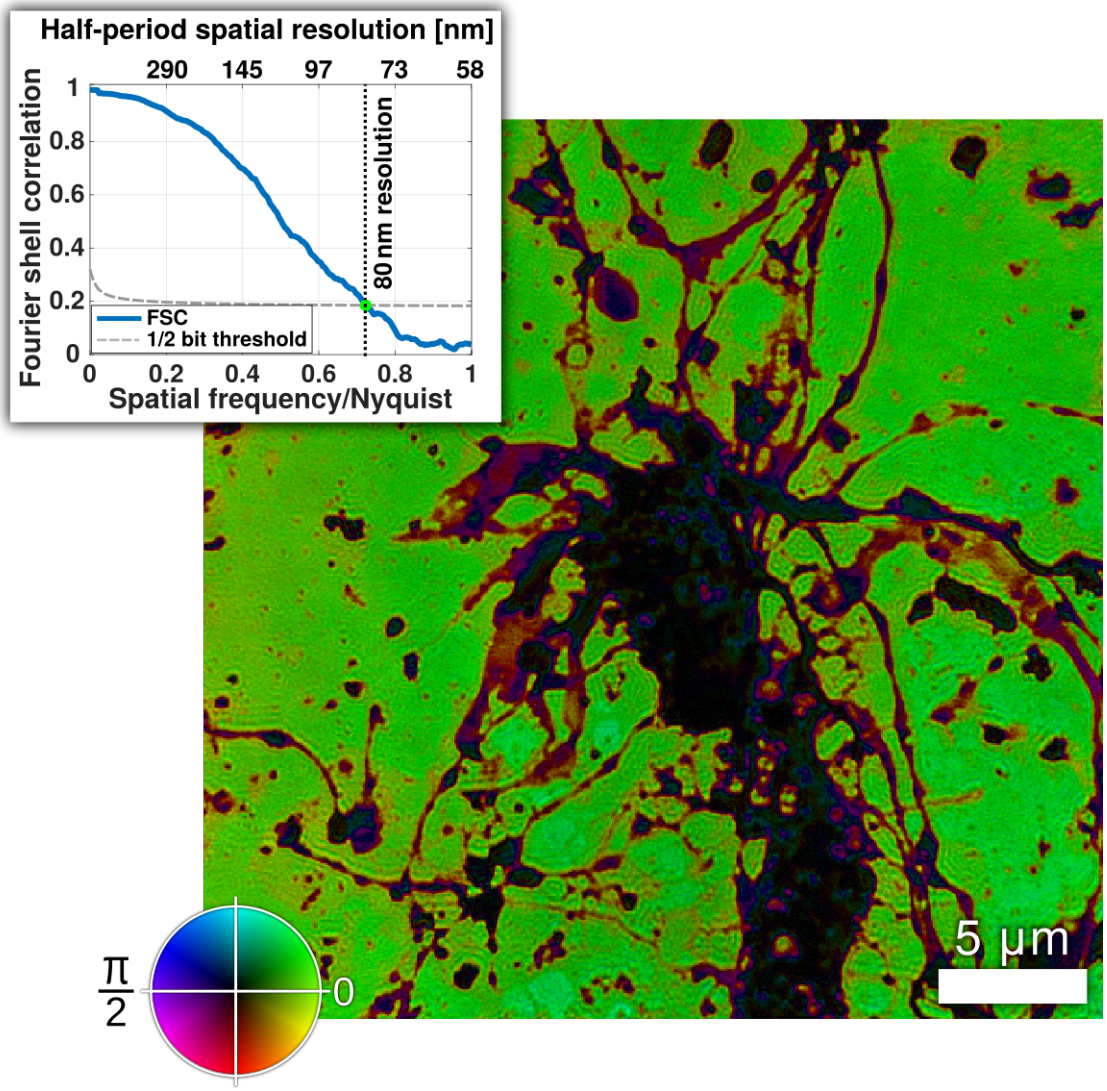

FIGURE 5.11: Image of a region of DIV7 neurons with FRC inset. In this case, a pair of images were reconstructed two data sets created artificially from a single data set by putting collected diffraction patterns from alternating probe positions into each. The calculated pixel size here is 58 nm and the effective resolution is 80 nm. This figure was used in [10].

two images of DIV7 neuron cells, which were reconstructed from two data sets of the same region taken on different days. The NA in the experimental geometry set the pixel size at 85 nm for both of the reconstructions, and the value at which the FRC first falls below the half bit criterion is 0.75 of the Nyquist limit, suggesting an effective resolution of 112 nm in this case.

The long scan times for each image mean it is not always viable to take multiple data sets to estimate the reconstruction quality. An alternative is to artificially create two data sets by splitting the collected diffraction patterns, assigning data from alternating probe positions into each. In this way the two data sets will not share short term illumination fluctuations and random noise. However, this effectively increases the step

size between scan positions and reduces the overlap ratio, and this method does not work for all images. An example FRC from artificially created data sets is given in figure 5.11; here the half bit resolution is 80 nm. We find very similar FRC curves from real and artificial data sets, suggesting this is also an acceptable way to estimate resolution provided the data is robust enough to handle the reduced overlap. Generally we find an intercept in the range of 0.7-0.8 of the Nyquist frequency, which sets the scale of the resolution we achieve compared to the diffraction limit, and is somewhat independent of the experimental NA within the geometries that have been used.

5.3.4 Thickness Measurements and Axial Resolution

Remembering that the reconstructed field of the object O is simply the complex transmission of the sample, related to the refractive index $n = 1 - \delta + i\beta$ and thickness Δz at each transverse position

$$O = \exp\left[ik(\delta + i\beta)\Delta z\right] \tag{5.3}$$

we can see that the real and imaginary parts contribute separately to the attenuation $\frac{I}{I_0}$ and relative phase shift ϕ by

$$\frac{I}{I_0} = \exp(-\mu\Delta z) = \exp\left(-2\left(\frac{2\pi}{\lambda}\beta\right)\Delta z\right) \tag{5.4}$$

$$\phi = -\frac{2\pi}{\lambda}\delta\Delta z \tag{5.5}$$

These equations can be manipulated to eliminate Δz, such that though we cannot directly measure the real and imaginary components of the refractive index independently of the thickness, the ratio δ/β can be determined, which allows some insight into the sample composition. Alternatively, with some prior knowledge about sample composition, we can use expected values for δ and β to provide two independent measurements for the sample thickness, which can be compared with each other.

Figure 5.12 shows thickness measurements calculated from two images of different DIV7 neuron samples. (A) shows a monochrome image of EUV transmission intensity from a ptychographic reconstruction, with wide field fluorescence emission signal from tubulin (red) and actin (green) markers overlaid. (B) is a magnified image of the region within the white rectangle in (A), in which a neurite that is rich in tubulin as indicated by the bright fluorescence signal in (A) is more closely inspected. (C) shows the sample thickness cross section along the dotted white line in (B). These were derived from

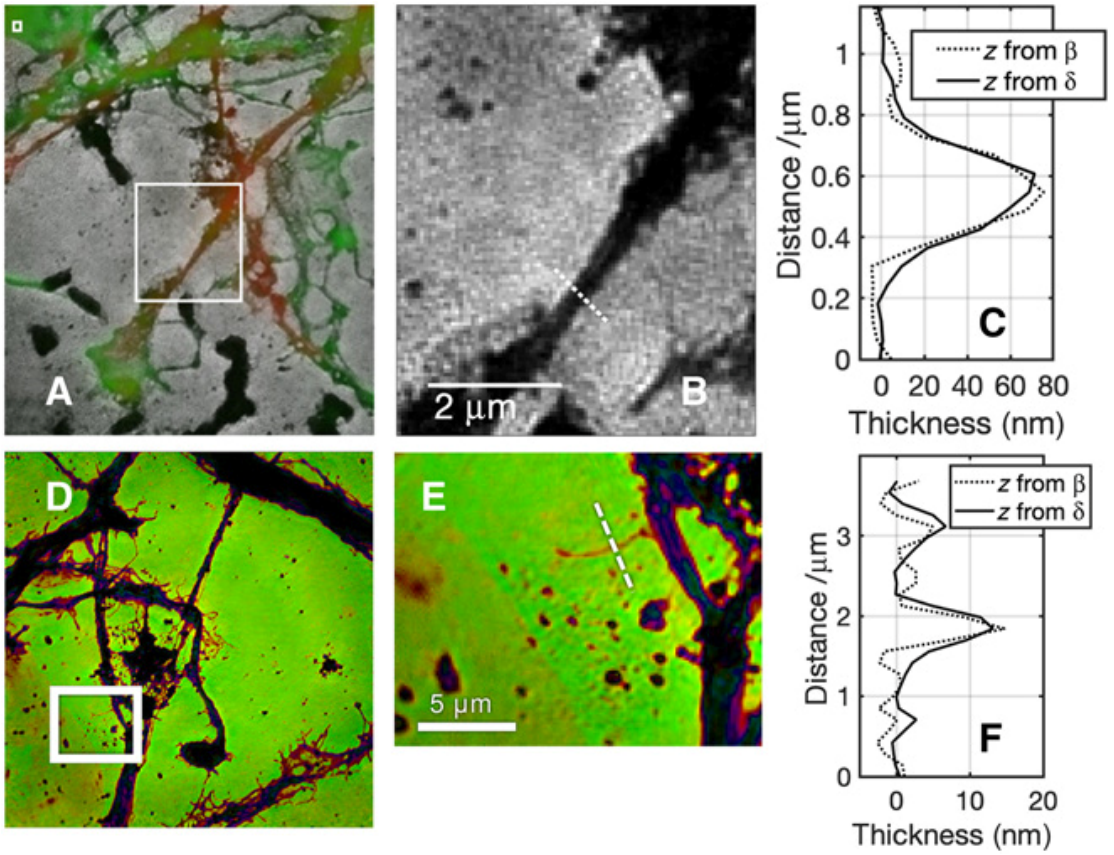

FIGURE 5.12: (A) Transparent grey scale image is the transmitted EUV intensity of a DIV7 neuron sample. The red and green colour channels are correlated wide field fluorescence images showing emission intensity of tubulin and actin markers respectively. (B) EUV intensity only of the region indicated by the white rectangle in (A). (C) Thickness cross sections taken along the white dotted line in (B), calculated based on the amplitude and phase in the EUV image, assuming the refractive index of tubulin. (D) Reconstruction of an unstained DIV7 neuron sample. (E) Region indicated by the white rectangle in (D). (F) Thickness cross sections taken along the white dotted line in (E) calculated from the amplitude and phase of the EUV image, assuming the refractive index of generic protein. This image was used in [10]. The ptychography data in (A) and (B) was taken by myself; the data in (D) and (E) was collected by Peter Baksh.

the complex EUV transmission, where the values used for δ and β are mouse tubulin, based on the molecular formula [77] and density [78]. Comparing the values for sample thickness calculated independently from δ and β, the values agree to within 8%.

Images (D-F) are of an unstained sample. (D) shows the complex EUV transmission, (E) is a magnified image of the region within the white rectangle in (D), and (F) shows the thickness cross sections based on expected δ and β. Here the material is assumed to be composed of protein, as no direct information about its composition from fluorescence imaging was available. Comparison of thicknesses calculated from δ and β in this case shows agreement to within 12%, which supports the assumption that the dendrite is made of protein. If a large sample area (at least 10x10 µm) containing no neurons is examined to correct the background, the root mean square (RMS) noise levels are 3.3%

in intensity, which suggests an axial sensitivity capable of distinguishing a 1.3 nm protein layer through such thickness measurements, and 0.02 radians in phase, equivalent to a 0.8 nm layer.

5.3.5 Radiation Damage

Damage to biological samples has become an accepted consequence for high energy illumination methods, and generally sets the main limitation on image resolution in cryo-electron [79] and hard x-ray microscopy [78]. Introduction of ionizing radiation causes a number of interactions that can ultimately lead to structural degradation. The incident radiation breaks molecular bonds, as well as producing electrons and free radicals via ionization. This can have a knock on effect as the generated electrons bombard other molecules and the free radicals exchange electrons with neighbouring molecules. The chemical reactions caused by these interactions can liberate hydrogen from various hydrocarbons present in biological specimens to produce gas and drive further deformations. Finally, the various interactions invariably dump energy in the form of heat, which can often produce temperatures exceeding the damage threshold of the materials present.

These mechanisms cause a complex cascade of effects that can be difficult to characterize; correspondingly there a number of studies dedicated to describing them [80, 81]. These provide numerous considerations for reducing the damage as much as possible for different energy regimes and sample types, for example by cooling to cryogenic temperatures. Alternatively, the effects of damage are simply accepted, and the image is formed before the majority of damage has occurred. This may be done by using ultrashort pulses in the illumination, such as those produced by an x-ray free electron laser (XFEL) [82]; though damage still occurs, some of which may be present in the final image [83].

To assess the level of radiation that is expected to cause damage, the radiation dose is defined as a useful parameter, and is the energy deposited in the sample per unit mass. In our case, the dose per second used during an imaging experiment can be expressed using the incident intensity I_0 and object attenuation $4\pi\beta/\lambda$

$$D = \frac{I_0}{\rho}\frac{4\pi\beta}{\lambda} \tag{5.6}$$

for a sample with density ρ. The unit for dose is Gray (Gy), equivalent to $\mathrm{J\,kg^{-1}}$

Typically, during data collection for a single reconstructed image, a neuron sample will receive a dose of $\sim 10^7$ Gy. After imaging the same regions on these samples, there is no observable change to sample structure at 42 eV. This is in sharp contrast to imaging these samples using a synchrotron source at 7.3 keV, for which significant damage was observed at a dose of $\sim 10^5$ Gy [13]. This suggests that the mechanisms that cause

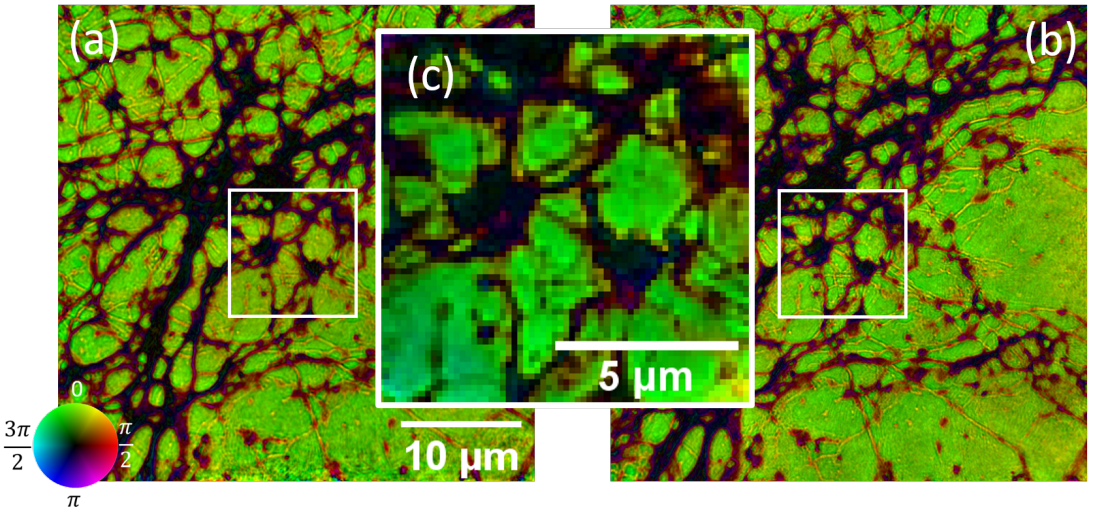

FIGURE 5.13: Comparison of the same region of DIV7 neurons (a) before, (b) after and (c) during attempt to damage the sample with 42eV EUV radiation.

damage which are significant for hard x-ray illumination are not noticeable in the EUV. Another difference in the illumination that may have an effect is the pulse length, where the sample is exposed to EUV for less than 40 fs in each 1 ms interval, compared with the continuous bombardment from synchrotron radiation; in various applications it is observed that changing the pulse length can impact the resulting damage significantly [84].

To put a limit on the radiation dose we can use before causing resolution limiting damage, we looked at a specific area on a DIV7 neuron sample. A 40x40 µm region was scanned, then the following day a 10x10 µm area within this region was scanned at a higher exposure and shorter step size, then the original 40x40 µm region was scanned a second time to compare the sample structure; figure 5.13 shows the results of this experiment. The dose for each of the regular images shown in (a) and (b) was the normal $\sim 10^7$ Gy used in the majority of experiments. The white box indicates the area within which the higher exposure was used, with a reconstruction of this data set shown in (c). Here the dose used was 50 times higher than for the other two images, with no observable damage. This suggests that we are operating in a regime where the photon energy is not high enough for the dose to be a useful parameter to set a limit to prevent damage, and intensity may be the limiting factor in this case.

5.4 Summary

In this chapter, the way we display the combined amplitude and phase information in a single HSV image was described, as well as some details about typical imaging runs and how we use intensity maps to choose the sample region.

The diversity of the data was discussed with its relation to the success of the reconstruction process; the structure of both the probe and the object is important here, and some failed scan data is shown. This illustrates an important obstacle in coherent imaging with a high harmonic source that is reflected in the literature, where there are many examples of man made test sample images, but to the best of our knowledge no examples of reconstructions of unknown objects aside from those produced by our group.

Some of the images of mouse hippocampal neurons were shown, alongside direct comparisons with wide field fluorescence images, showing the scale at which we operate and the clear improvement in image resolution, and the potential for EUV ptychography to assist in the interpretation of fluorescence images. A comparison of EUV ptychography and SIM images was also shown, where the resolution was comparable but the high contrast in the EUV highlighted thin features that were invisible to the super resolution fluorescence technique.

The transverse resolution was estimated using FRC, where it was shown that features down to 80 nm in size were resolved. The FRC intercept with the half bit criterion within the range of 0.7-0.8 of the Nyquist spatial frequency has been shown to be consistent with different NA values for varying experimental geometries, and consistent with real and artificially split data sets. The amplitude and phase information was also used to perform thickness measurements based on expected sample composition, both by assuming the sample material and by correlation with fluorescence measurements, with an estimated axial sensitivity of $\sim$1 nm based on noise levels.

Finally, the samples were subjected to an EUV radiation dose 50 times higher than regularly used for imaging to test for damage. Direct comparison of the targeted area with the reconstructed images before and after the exposure showed no sign of structure deformation or resolution decrease, in sharp contrast to what is expected from synchrotron/XFEL radiation at higher energies, suggesting that the biological samples are very robust to radiation in the EUV spectral range and can be imaged repeatedly with no noticeable object deterioration.

Chapter 6

Conclusions and Future Work

6.1 Conclusion

The HHG conditions for 29 nm generation from an 800 nm input beam have been optimized for use in ptychographic imaging, and the importance of careful input beam characterization and stabilization shown. The efforts to improve the short and long term position stability as well as maintain a stable pulse length are reflected in the stability of the EUV output. The EUV photon detection was carefully considered, with an emphasis on identifying sources of noise and reducing them as far as possible in both the experiment and post processing. The dynamic range of the camera was also artificially increased by our HDR method. These experimental and numerical techniques are crucial for improving the SNR, which plays a vital role in lensless imaging by maintaining high data diversity over a range of spatial frequencies to assist the reconstruction process and maximize the final image resolution.

The properties of the EUV beam have been measured with relation to how the generation conditions affect the shape of the EUV spatial profile. A model of the EUV beam propagated from the gas cell to the CCD camera via an off-axis mirror and aperture at the EUV focus was used as a guide to explain the shape of the near field wave front observed in the EUV probe determined by ptychography and the far field diffraction pattern, and compared with convolution spot size measurements; the disagreement between simulation and real data suggests a higher M^2 parameter in the EUV beam than expected. The coherence was determined via double slit diffraction measurements fitted to a partially coherent intensity model to measure the fringe visibility, for which the EUV beam shape provides a reference for the generation conditions that maximize spatial coherence.

The properties of the EUV source were tested in ptychographic imaging experiments, where the chance of a successful reconstruction is largely influenced by the EUV spatial

coherence and stability, as well as the diversity of information in the object and probe. This illustrates a key obstacle specific to imaging with a high harmonic source, which has been overcome in this work in outputting high quality images consistently, both for test samples and unknown objects.

Successful reconstructed images of mouse hippocampal neurons were shown, and correlated with wide field and super resolution fluorescence microscope images of the same sample regions for direct comparison, from which a there is a clear advantage in resolution for EUV ptychography over wide field fluorescence and optical microscope images. The object structure comparison also motivates the use of our technique to assist in the interpretation of fluorescence images. The comparison with SIM imaging indicates that even though the transverse resolution may be comparable, the high absorption at EUV wavelengths provides significant benefits for imaging very thin ($\sim$ 100 nm) structures. The lack of fluorophores in thin structures means these features are lost to the fluorescence background, whereas high contrast is still observed in the EUV. Again, this provides motivation to use our technique to complement fluorescence microscopy, where features on the scale of 100 nm are well highlighted in the EUV, but the limited transmission through objects at $>1\,\mu$m means that SIM is favourable for imaging thick objects.

The transverse resolution was estimated by FRC, with a minimum resolved object size of 80 nm, and the consistency of the FRC intercept with the half bit criterion at 70-80% of the Nyquist limit at various experimental NAs for both real and artificially split data sets suggests that better resolution may be achievable with a different collection geometry. The amplitude and phase information available from reconstructed data was used to measure the sample thickness based on expected sample composition. Based on RMS noise levels, we estimate the axial sensitivity to be $\sim$1 nm, which is due to the strength of the light matter interaction in the EUV spectral region.

Finally, an assessment of the effects of radiation damage to biological samples was made. We observe no radiation damage to the sample despite using a dose of 50 times higher than is necessary for a standard imaging experiment. This is in sharp contrast to what has been observed using 7.3 keV radiation from a synchroton, and what is generally expected from soft/hard x-ray imaging. This indicates that the damage mechanisms that are significant at higher energies are not notable at EUV energies, and that intensity may be a more important parameter for anticipating sample damage than radiation dose in this photon energy range.

6.2 Future Work

6.2.1 Imaging of Transfected Neuron Samples

The biological images shown in this thesis are of mouse hippocampal neurons, and aside from the effect of drying and fixing during the sample preparation, the various structures should be representative of the structures present in healthy cells. Currently, there is a significant research effort towards better understanding the underlying causes of neurodegenerative conditions such as Alzheimer's disease and Pick's disease. The cause of these conditions has been linked to the formation and propagation of abnormal assemblies due to misfolded tau protein, which is responsible for the stability of microtubule structures.

Recent work in cryo-electron microscopy [85, 86, 87] has shown some of the specific orientations that the protein folds into, and studies on larger scales [88] have shown the impact this has on neuron function; figure 6.1 shows a fluorescence comparison of a control (red) and transfected (green) axon with e14 mutant tau. The undulation shown in the transfected axon image indicates an accumulation of protein, which affects the neuron response.

Though the mechanisms for misfolding are well characterized by cryo-electron microscopy, and the resulting tau accumulation is observed in fluorescence imaging, the relationship between initial misfolding and consequential propagation across neuronal connections is not well understood. The high resolution and contrast available with EUV ptychography that has been demonstrated on neuron samples may allow better characterization of the structures formed by misfolded tau protein on a scale in between the fluorescence and electron studies, which could in turn shed light on the propagation of neurodegenerative diseases, with obvious impact on biological research.

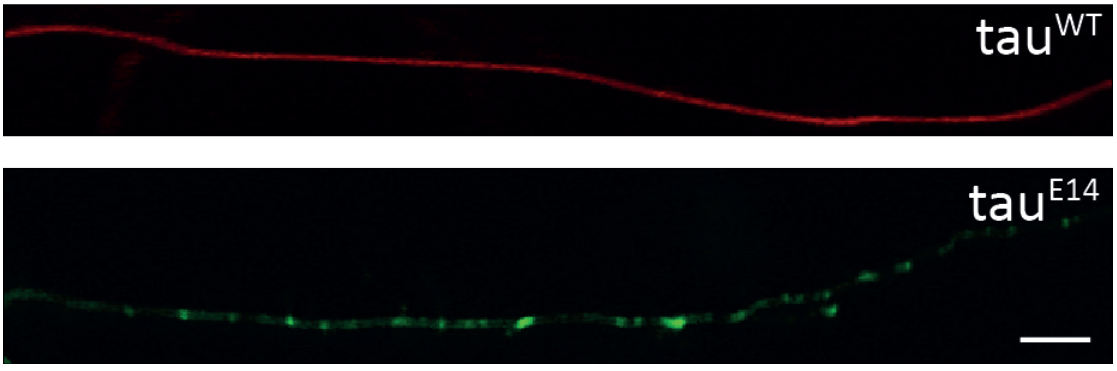

FIGURE 6.1: Fluorescence microscope image of a control (red) and mutant tau transfected (green) axon, showing the aggregation of protein into clusters that affect neuron response. The scale bar is 10 µm. Image taken by Dr Katrin Deinhardt from the Biological Sciences department at the University of Southampton.

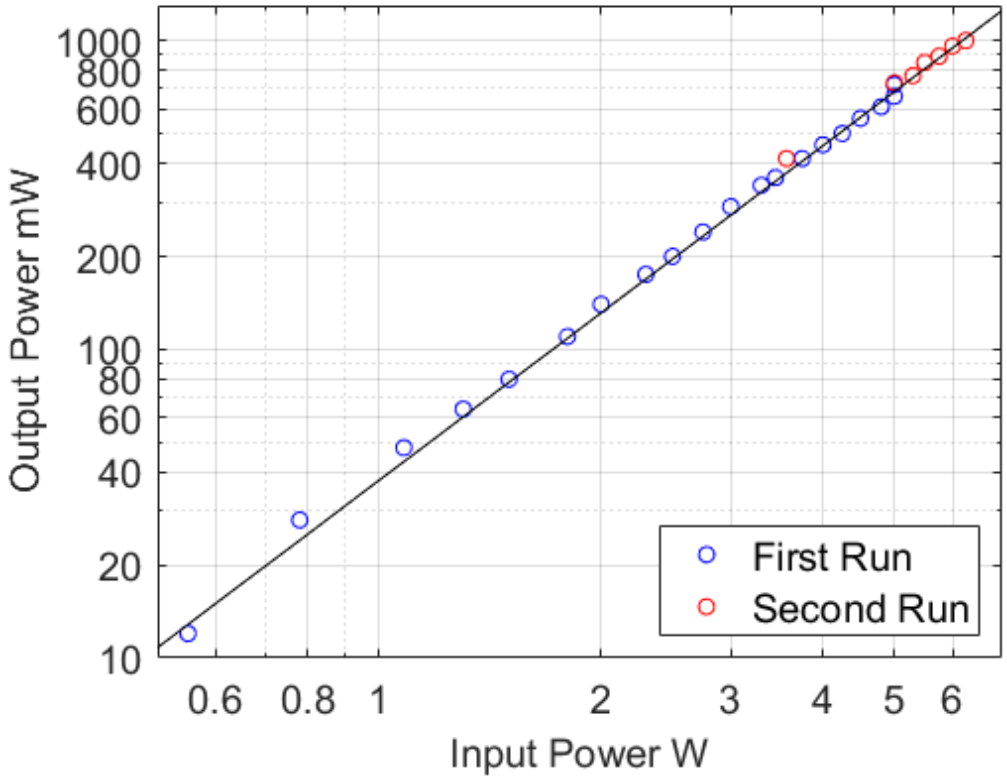

FIGURE 6.2: Logscale base ten plot of SHG power vs input power for two separate trial runs; the crystal position was re-optimized before starting the second, higher power run. The black line is a fit to the equation $y = kx^{1.8}$

6.2.2 Short Wavelength High Harmonic Generation

It is clear from the cut-off energy in equation 2.12 that the shortest possible wavelength generated in HHG scales inversely with the square of the fundamental wavelength λ. However, the HHG flux has been predicted to vary between λ^{-5} and λ^{-6} [89], and experimentally found to vary with an even higher exponent in the input beam wavelength range of 800-1850 nm [90]. This provides some motivation to study the effect of high harmonics generated after a low order frequency conversion; for example if the wavelength can be halved by SHG, the HHG conversion efficiency could be increased by 60 times.

However, this is also subject to the conversion efficiency of the low order process, in particular to maintain an acceptable cut-off energy. Some preliminary experiments were performed on the Artemis laser system at the Central Laser Facility (CLF). This system was similar to the laser at the University of Southampton, providing 800 nm, 40 fs pulses at 1 kHz repetition rate, but up to 10 mJ pulse energy compared with the 3 mJ available with our laser. Figure 6.2 shows the SHG power vs IR input power for single pass transmission through a BBO crystal during two separate trial runs, taken in a development week on the Artemis system. The data was collected by myself and Bill

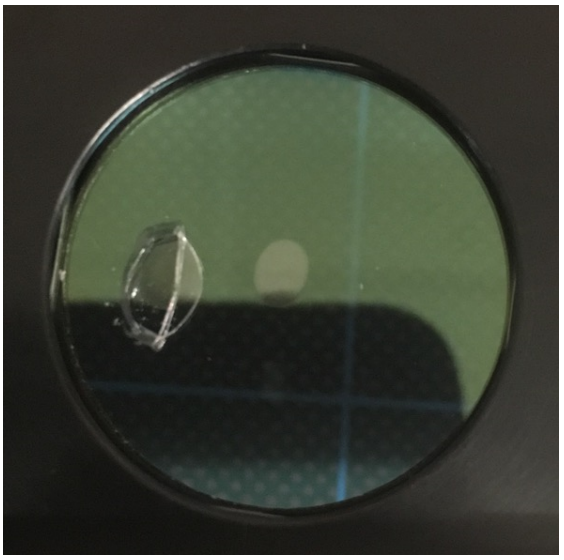

FIGURE 6.3: A photo of the BBO crystal after using an input laser intensity that exceeded the damage threshold, twice.

Brocklesby, and Artemis senior scientists Richard Chapman and Adam Wyatt. This shows a maximum conversion efficiency of 16%, with 1 W of 400 nm power measured, corresponding to 1 mJ pulses. The data points are fit to the equation $y = kx^{1.8}$, for which the exponent is expected to be 2 for SHG corresponding to the square relationship of the second order polarization response with input field. This may be caused by significant depletion of the fundamental beam.

The SHG output from this experiment was used to generate high order harmonics, which were not properly characterized but showed high brightness for a lower detector gain setting than would usually be used to measure HHG at this facility, which opens the possibility for further study here. An important note is that the limit for SHG conversion efficiency is the damage threshold of the SHG crystal, which was exceeded during this run, as shown in figure 6.3. Clearly the intensity of the input beam at the crystal should be carefully calculated before performing such a study.

6.2.3 A Dynamic Meta-Material Experiment

Meta materials (MMs) use fabricated nano-scale structures to exhibit a desired response to an incident field, and are an exciting prospect in photonics research since they allow engineering of optical properties, such as refractive index, that are otherwise reliant on the existence of a suitable medium. Mechanical MMs allow dynamic control of the material properties by variation of the MM structure, which subsequently affects the optical interaction.

A MM must necessarily be made from structures much smaller than the illumination wavelength in order to behave as a homogeneous material. As a result, the structures in

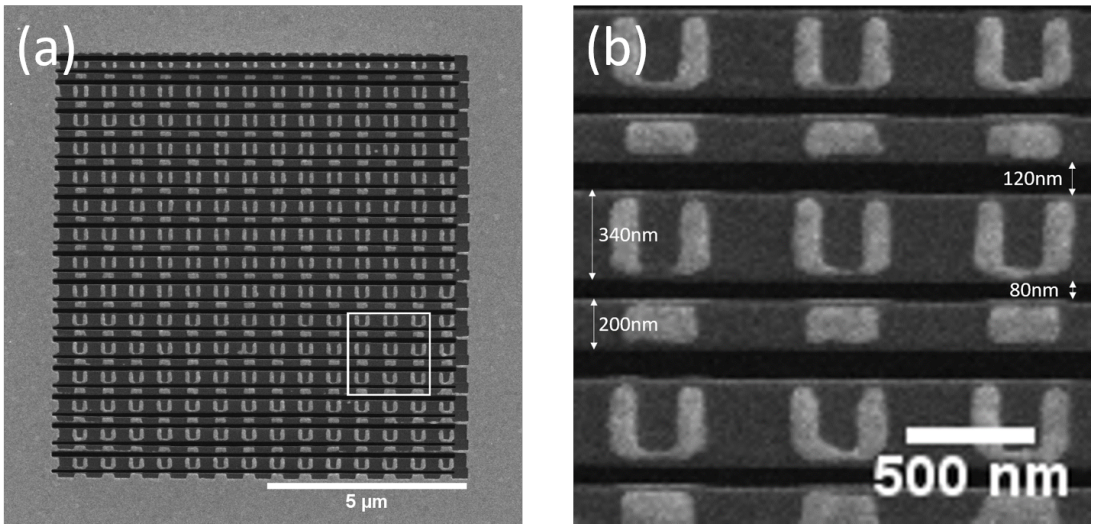

FIGURE 6.4: SEM images of MM sample; (a) shows the full grid, (b) is a zoomed image of the white box in (a) with additional labels to show distance scales.

such materials designed to control optical properties in the visible or near infrared regime cannot be imaged using conventional visible light microscopy. Whilst these materials can be studied via electron microscopy to obtain high resolution images of fine structures, the observation of dynamics at short time scales is limited by the speed of the detector.

Our EUV source can be used to explore such fast dynamics with a 'pump-probe' experiment, where a laser pulse referred to as the 'pump' is used to induce a response from the sample, and a second shorter wavelength 'probe' pulse is used to study the effect of the response by observing changes in the probe beam. By varying the delay time between the pump and probe pulses, the dynamic evolution of the response may be measured with a time resolution that is limited by the probe pulse duration, without the need for a fast detector. In our case, the probe is the EUV source, which consists of ultrashort pulses on the order of 10 fs in duration at 29 nm, and the pump is a modulated diode laser at 1470 nm with a pulse duration greater than a microsecond; this was chosen as an available source at a wavelength that can induce a useful mechanical response in the MM sample.

The sample under investigation was a mechanical MM fabricated by Bruce Ou (Optoelectronics Research Centre); an SEM image is shown in figure 6.4. The sample is a 10 µm×10 µm grid of split ring resonators suspended on silicon nitride strips with alternating widths of 200 nm and 340 nm, and alternating spacings of 80 nm and 120 nm; (a) shows the full grid and (b) shows a zoomed region to indicate the scale of MM structures. It was fabricated with a focused ion beam from a 50 nm thick silicon nitride membrane covered by 50 nm of gold. This section considers a pump-probe style experiment performed on this sample where the MM response is studied via variation in the diffraction patterns at the detector and by ptychographic imaging; an example of the diffraction by this grid is shown in figure 6.5.

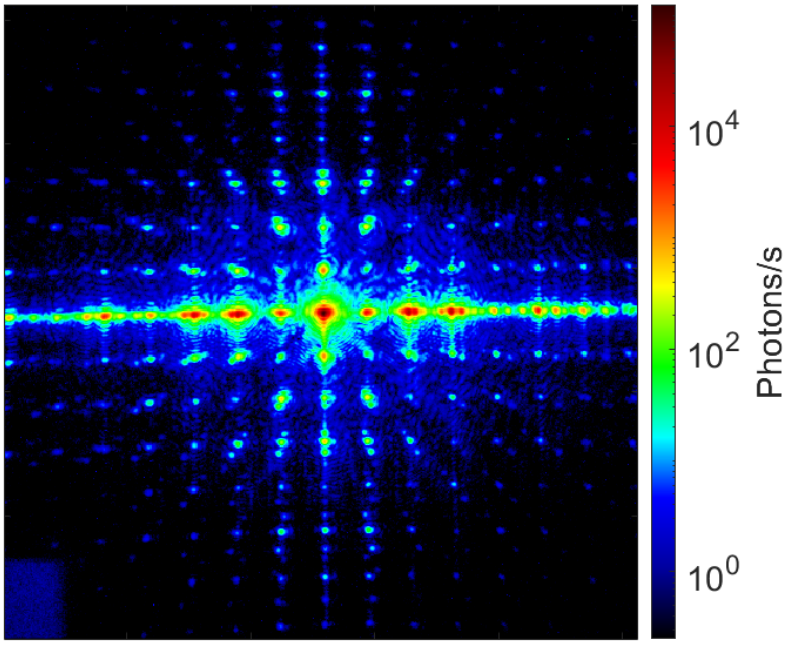

FIGURE 6.5: Far field diffraction of our EUV source transmitted through the MM sample.

In order to simulate the effect of the MM sample on a probe field, we must first consider how the sample is expected to respond under excitation; the expected optical interaction of this sample is described in [69]. An illuminating electromagnetic wave induces moving charges in the gold nanostructures. This results in optical forces within the MM plane between neighbouring strips due to dipole interactions, and Lorentz forces normal to the surface from interaction between moving charges and the incident wave's magnetic field.

At the same time, light induced heating causes the strips to deform due to thermal expansion and bend out of the MM plane. Narrow strips bend more at the same temperature as a result of a higher fraction of each strip that is covered in gold, since the thermal expansion coefficient of gold is ∼5 times higher than that of silicon nitride. These effects may be examined by using the EUV beam as a probe during excitation with an IR pump beam, since the nanostructures are larger than the EUV wavelength.

In the simulation, the silicon nitride strips were considered as two separate diffraction gratings, one for odd and one for even strips, that attenuate radiation completely. The effects of transmission and phase shift by the strips and diffraction by gold nanoparticles were ignored for simplicity; though these effects do impact the diffraction pattern, information about how the pattern changes can be obtained without including them in

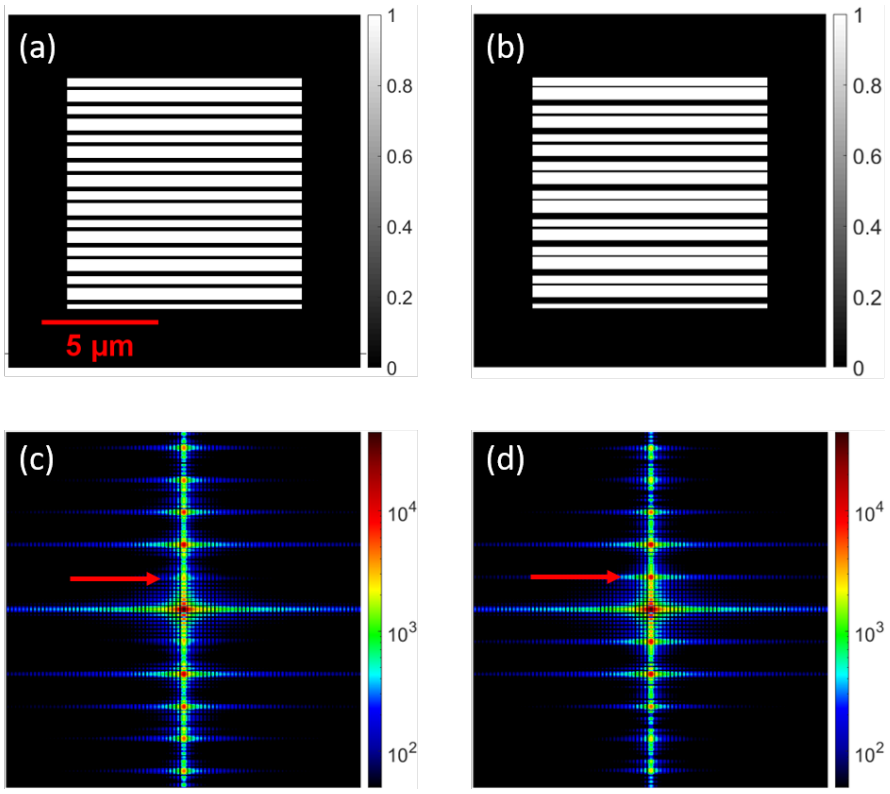

FIGURE 6.6: Simulation of diffraction through a MM grid; (a) shows the exit wave through a simple grid with similar dimensions to the MM sample, (b) is the same grid with the thin pillars shifted down by 100 nm relative to the thick pillars, and (c) and (d) show the corresponding field amplitudes in the Fourier plane. The odd diffraction orders show an increase in relative amplitude when the grid has been shifted, as indicated in the first order by the red arrows.

the model. The in-plane effects were then considered as a relative shift of one grating with respect to the other, perpendicular to the direction of propagation.

The effect of in-plane forces is demonstrated in figure 6.6. Here, the thin strips were shifted vertically (downwards) relative to the thick strips, and a 2D Fourier transform taken to propagate to the detector plane. The intensity at the detector clearly exhibits additional diffraction peaks upon excitation of the MM, as indicated by the red arrows in (c) and (d), whereas other previously prominent peaks become attenuated. The magnitude of the change in the diffraction pattern depends on the size of the shift.

The effect of the motion of the MM during excitation from a laser pulse can be studied by a pump-probe experiment, as mentioned above. In this experiment, a modulated diode laser operating at 1470 nm is used as a pump pulse to drive the MM and induce shift of some strips relative to others, as discussed in the simulations. The 29 nm EUV beam will then be introduced as a probe pulse after a known delay time with respect to the pump, and diffraction patterns measured as a function of delay time. The pump is modulated such that the repetition rate of the pump and probe pulses are the same, and the delay time between them is the same for every pulse. In order to acquire enough

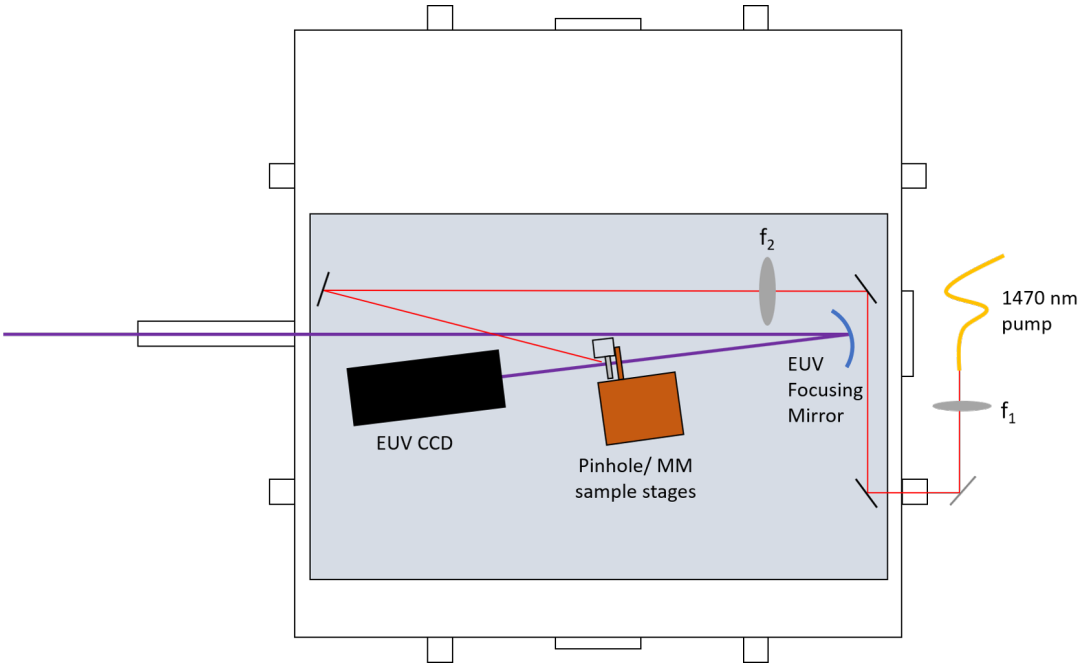

FIGURE 6.7: Schematic of the proposed set up for a pump-probe MM experiment using our system.

contrast to make quantitative measurements, the intensity measured at the detector will be from a number of probe pulses.

The set up for the experiment is shown in figure 6.7. Our 1470 nm modulated source is collimated by a lens of focal length f_1 after it exits an optical fiber. It is then coupled into the chamber via a filter to remove any visible radiation and focused onto the back of the MM sample by a second lens with focal length f_2. The focal lengths for these lenses are selected to set a peak intensity of $10\,\mu W\mu m^{-2}$ on the sample, which is sufficient to induce a response without exceeding the sample damage threshold.

The magnitude of the in-plane movement is expected to increase with the amplitude of the pump pulse, then quickly disappear as the pump drops off. Any fast variations in the MM, for example from vibrations in the strips, will be averaged out in the diffraction patterns, as the intensity measured at the detector is a result of diffraction from many pulses. However, the magnitude of the movement can be obtained from the diffraction patterns, and this could be confirmed by ptychography.

Currently, the issue with such an experiment is the reduction in SNR due to scattering by the IR pump used to induce the material response. Also, the issues with imaging a regular grid sample are discussed in 5.2.2. In future work, either the IR pump scattering would need to be reduced or a different mechanism to induce the MM response used. Imaging the grid successfully using ptychography may require the introduction of additional constraints to distinguish the object from the probe.

Bibliography

[1] N. H. Burnett, H. A. Baldis, M. C. Richardson, and G. D. Enright. Harmonic generation in CO2 laser target interaction. *Applied Physics Letters*, 31(3):172, 8 2008.

[2] A. McPherson, G. Gibson, H. Jara, U. Johann, T. S. Luk, I. A. McIntyre, K. Boyer, and C. K. Rhodes. Studies of multiphoton production of vacuum-ultraviolet radiation in the rare gases. *Journal of the Optical Society of America B*, 4(4):595, 1987.

[3] M Ferray, A L'Huillier, X F Li, L A Lompre, G Mainfray, and C Manus. Multiple-harmonic conversion of 1064 nm radiation in rare gases. *Journal of Physics B: Atomic, Molecular and Optical Physics*, 21(3):L31–L35, 1988.

[4] Richard L. Sandberg, Ariel Paul, Daisy A. Raymondson, Steffen Hädrich, David M. Gaudiosi, Jim Holtsnider, Ra'anan I. Tobey, Oren Cohen, Margaret M. Murnane, Henry C. Kapteyn, Changyong Song, Jianwei Miao, Yanwei Liu, and Farhad Salmassi. Lensless Diffractive Imaging Using Tabletop Coherent High-Harmonic Soft-X-Ray Beams. *Physical Review Letters*, 99(9):098103, 8 2007.

[5] Bosheng Zhang, Daniel E. Adams, Dennis F. Gardner, Elisabeth R. Shanblatt, Henry C. Kapteyn, Margaret M. Murnane, and Matthew D. Seaberg. Tabletop nanometer extreme ultraviolet imaging in an extended reflection mode using coherent Fresnel ptychography. *Optica, Vol. 1, Issue 1, pp. 39-44*, 1(1):39–44, 7 2014.

[6] S. Roy, D. Parks, K. A. Seu, R. Su, J. J. Turner, W. Chao, E. H. Anderson, S. Cabrini, and S. D. Kevan. Lensless X-ray imaging in reflection geometry. *Nature Photonics 2011 5:4*, 5(4):243–245, 2 2011.

[7] Bosheng Zhang, Daniel E. Adams, Dennis F. Gardner, Eric Gullikson, Farhad Salmassi, Henry Kapteyn, Leigh S. Martin, Margaret Murnane, and Matthew D. Seaberg. High numerical aperture reflection mode coherent diffraction microscopy using off-axis apertured illumination. *Optics Express, Vol. 20, Issue 17, pp. 19050-19059*, 20(17):19050–19059, 8 2012.

[8] Bosheng Zhang, Dennis F Gardner, Matthew D Seaberg, Elisabeth R Shanblatt, Henry C Kapteyn, Margaret M Murnane, and Daniel E Adams. High contrast 3D

imaging of surfaces near the wavelength limit using tabletop EUV ptychography. *Ultramicroscopy*, 158:98–104, 2015.

[9] M. Odstrcil, P. Baksh, S. A. Boden, R. Card, J. E. Chad, J. G. Frey, and W. S. Brocklesby. Ptychographic coherent diffractive imaging with orthogonal probe relaxation. *Optics Express*, 24(8):8360, 2016.

[10] Peter D Baksh, Michal Ostrčil, Magdalena Miszczak, Charles Pooley, Richard T Chapman, Adam S Wyatt, Emma Springate, John E Chad, Katrin Deinhardt, Jeremy G Frey, and William S Brocklesby. Quantitative and correlative extreme ultraviolet coherent imaging of mouse hippocampal neurons at high resolution. *Science Advances*, 6(18), 2020.

[11] M. A. O'Keefe, C. J.D. Hetherington, Y. C. Wang, E. C. Nelson, J. H. Turner, C. Kisielowski, J. O. Malm, R. Mueller, J. Ringnalda, M. Pan, and A. Thust. Sub-Ångstrom high-resolution transmission electron microscopy at 300keV. *Ultramicroscopy*, 89(4):215–241, 11 2001.

[12] Bonnie O. Leung and Keng C. Chou. Review of super - Resolution fluorescence microscopy for biology. *Applied Spectroscopy*, 65(9):967–980, 2011.

[13] Peter Baksh, Michal Odstrcil, Aaron Parsons, Jo Bailey, Katrin Deinhardt, John E Chad, William S Brocklesby, and Jeremy G Frey. Quantitative Evaluation of Hard X-ray Damage to Biological Samples using EUV Ptychography. *Journal of Physics: Conference Series*, 849:12034, 6 2017.

[14] Elsa Garmire. Nonlinear optics in daily life. *Optics Express*, 21(25):30532, 2013.

[15] Amnon Yariv. Quantum Electronics, 1975.

[16] A. L'Huillier, D. Descamps, A. Johansson, J. Norin, J. Mauritsson, and C. G. Wahlström. Applications of high-order harmonics. *European Physical Journal D*, 26(1):91–98, 2003.

[17] K. J. Schafer, Baorui Yang, L. F. Dimauro, and K. C. Kulander. Above threshold ionization beyond the high harmonic cutoff. *Physical Review Letters*, 70(11):1599–1602, 3 1993.

[18] Jeffrey L. Krause, Kenneth J. Schafer, and Kenneth C. Kulander. High-order harmonic generation from atoms and ions in the high intensity regime. *Physical Review Letters*, 68(24):3535–3538, 6 1992.

[19] P. B. Corkum. Plasma perspective on strong field multiphoton ionization. *Physical Review Letters*, 71(13):1994–1997, 1993.

[20] M. Lewenstein, Ph Balcou, M. Yu Ivanov, Anne L'Huillier, and P. B. Corkum. Theory of high-harmonic generation by low-frequency laser fields. *Physical Review A*, 49(3):2117–2132, 1994.

[21] Timm Bredtmann, Szczepan Chelkowski, and André D. Bandrauk. Monitoring attosecond dynamics of coherent electron-nuclear wave packets by molecular high-order-harmonic generation. *Physical Review A - Atomic, Molecular, and Optical Physics*, 84(2):021401, 8 2011.

[22] Philippe Balcou, P Salieres, A LHuillier, Maciej Lewenstein, Anne L Huillier, and Pascal Salie. Generalized phase-matching conditions for high harmonics: The role of field-gradient forces. 55(4):3204–3210, 4 1997.

[23] Pascal Salières, Anne L'Huillier, and Maciej Lewenstein. Coherence control of high-order harmonics. *Physical Review Letters*, 74(19):3776–3779, 1995.

[24] S Kazamias, F Weihe, D Douillet, C Valentin, T Planchon, S Sebban, G Grillon, F. Augé, D. Hulin, and Ph Balcou. High order harmonic generation optimization with an apertured laser beam. *European Physical Journal D*, 21(3):353–359, 2002.

[25] S. Kazamias, D. Douillet, C. Valentin, Th Lefrou, G. Grillon, G. Mullot, F. Augé, P. Mercère, Ph Zeitoun, and Ph Balcou. Optimization of the focused flux of high harmonics. *European Physical Journal D*, 26(1):47–50, 2003.

[26] MacIej Lewenstein, Pascal Salières, and Anne Lhuillier. Phase of the atomic polarization in high-order harmonic generation. *Physical Review A*, 52(6):4747–4754, 1995.

[27] T. Ditmire, E. T. Gumbrell, R. A. Smith, J. W.G. Tisch, D. D. Meyerhofer, and M. H.R. Hutchinson. Spatial coherence measurement of soft x-ray radiation produced by high order harmonic generation. *Physical Review Letters*, 77(23):4756–4759, 1996.

[28] X. Zhang, A. R. Libertun, A. Paul, E. Gagnon, S. Backus, I. P. Christov, M. M. Murnane, H. C. Kapteyn, R. A. Bartels, Y. Liu, and D. T. Attwood. Highly coherent light at 13 nm generated by use of quasi-phase-matched high-harmonic generation. *Optics Letters*, 29(12):1357, 2004.

[29] R. A. Bartels, A. Paul, M. M. Murnane, H. C. Kapteyn, S. Backus, Y. Liu, and D. T. Attwood. Absolute determination of the wavelength and spectrum of an extreme-ultraviolet beam by a Young's double-slit measurement. *Optics Letters*, 27(9):707, 2002.

[30] M. Odstrčil, P. Baksh, H. Kim, S. A. Boden, W. S. Brocklesby, and J. G. Frey. Ultra-broadband ptychography with self-consistent coherence estimation from a high harmonic source. *X-Ray Lasers and Coherent X-Ray Sources: Development and Applications XI*, 9589(September 2015):958912, 2015.

[31] T. Ditmire, J. W. G. Tisch, E. T. Gumbrell, R. A. Smith, D. D. Meyerhofer, and M. H. R. Hutchinson. Spatial coherence of short wavelength high-order harmonics. *Applied Physics B*, 65(3):313–328, 1997.

[32] Michael J Sanderson, Ian Smith, Ian Parker, and Martin D Bootman. Fluorescence microscopy. *Cold Spring Harbor protocols*, 2014(10):pdb.top071795, 10 2014.

[33] Stefan W Hell and Jan Wichmann. Breaking the diffraction resolution limit by stimulated emission: stimulated-emission-depletion fluorescence microscopy. *Opt. Lett.*, 19(11):780–782, 6 1994.

[34] Giuseppe Vicidomini, Paolo Bianchini, and Alberto Diaspro. STED super-resolved microscopy. *Nature Methods*, 15(3):173–182, 2018.

[35] M. G.L. Gustafsson. Surpassing the lateral resolution limit by a factor of two using structured illumination microscopy. *Journal of Microscopy*, 198(2):82–87, 2000.

[36] Antoine G Godin, Brahim Lounis, and Laurent Cognet. Super-resolution Microscopy Approaches for Live Cell Imaging. *Biophysical Journal*, 107(8):1777–1784, 2014.

[37] Michael J Rust, Mark Bates, and Xiaowei Zhuang. Sub-diffraction-limit imaging by stochastic optical reconstruction microscopy (STORM). *Nature methods*, 3(10):793–795, 10 2006.

[38] Ulrike Endesfelder and Mike Heilemann. Direct Stochastic Optical Reconstruction Microscopy (dSTORM). In Peter J Verveer, editor, *Advanced Fluorescence Microscopy: Methods and Protocols*, pages 263–276. Springer New York, New York, NY, 2015.

[39] Gleb Shtengel, James A. Galbraith, Catherine G. Galbraith, Jennifer Lippincott-Schwartz, Jennifer M. Gillette, Suliana Manley, Rachid Sougrat, Clare M. Waterman, Pakorn Kanchanawong, Michael W. Davidson, Richard D. Fetter, and Harald F. Hess. Interferometric fluorescent super-resolution microscopy resolves 3D cellular ultrastructure. *Proceedings of the National Academy of Sciences of the United States of America*, 106(9):3125, 3 2009.

[40] D. Axelrod. Cell-substrate contacts illuminated by total internal reflection fluorescence. *The Journal of Cell Biology*, 89(1):141, 1981.

[41] Makio Tokunaga, Naoko Imamoto, and Kumiko Sakata-Sogawa. Highly inclined thin illumination enables clear single-molecule imaging in cells. *Nature Methods 2008 5:2*, 5(2):159–161, 1 2008.

[42] Shigeharu Tamura. Multilayer Fresnel Zone Plate with High-Diffraction Efficiency: Application of Composite Layer to X-Ray Optics. In *Metal, Ceramic and Polymeric Composites for Various Uses*. InTech, 7 2011.

[43] Syue Ren Wu, Yeukuang Hwu, and Giorgio Margaritondo. Hard-X-ray Zone Plates: Recent progress. *Materials*, 5(10):1752–1773, 2012.

[44] David A. Shapiro, Young Sang Yu, Tolek Tyliszczak, Jordi Cabana, Rich Celestre, Weilun Chao, Konstantin Kaznatcheev, A. L.David Kilcoyne, Filipe Maia, Stefano Marchesini, Y. Shirley Meng, Tony Warwick, Lee Lisheng Yang, and Howard A. Padmore. Chemical composition mapping with nanometre resolution by soft X-ray microscopy. *Nature Photonics*, 8(10):765–769, 2014.

[45] J. W. Goodman. *Introduction to Fourier Optics McGraw-Hill Series in Electrical and Computer Engineering*. Roberts and Company Publishers, 2005.

[46] D GABOR. A New Microscopic Principle. *Nature*, 161(4098):777–778, 1948.

[47] R W Gerchberg and W O Saxton. A practical algorithm for the determination of phase from image and diffraction plane pictures. *Optik*, 35(2):237–246, 1972.

[48] J. R. Fienup. Reconstruction of an object from the modulus of its Fourier transform. *Optics Letters*, 3(1):27, 1978.

[49] A M Maiden, M J Humphry, and J M Rodenburg. Ptychographic transmission microscopy in three dimensions using a multi-slice approach. *J. Opt. Soc. Am. A*, 29(8):1606–1614, 8 2012.

[50] H. NYQUIST. Certain Topics in Telegraph Transmission Theory. *Transactions of the American Institute of Electrical Engineers*, 47(2):617–644, 1928.

[51] R. H. T. Bates and W. R. Fright. Composite two-dimensional phase-restoration procedure. *Journal of the Optical Society of America*, 73(3):358, 3 1983.

[52] J. C.H. Spence, U. Weierstall, and M. Howells. Coherence and sampling requirements for diffractive imaging. *Ultramicroscopy*, 101(2-4):149–152, 2004.

[53] J M Rodenburg and R H T Bates. The theory of super-resolution electron microscopy via Wigner-distribution deconvolution. *Philosophical Transactions of the Royal Society of London. Series A: Physical and Engineering Sciences*, 339(1655):521–553, 1992.

[54] J. M. Rodenburg and H. M.L. Faulkner. A phase retrieval algorithm for shifting illumination. *Applied Physics Letters*, 85(20):4795–4797, 2004.

[55] Andrew M. Maiden and John M. Rodenburg. An improved ptychographical phase retrieval algorithm for diffractive imaging. *Ultramicroscopy*, 109(10):1256–1262, 2009.

[56] V. Elser, I. Rankenburg, and P. Thibault. Searching with iterated maps. *Proceedings of the National Academy of Sciences of the United States of America*, 104(2):418–423, 2007.

[57] Oliver Bunk, Martin Dierolf, Søren Kynde, Ian Johnson, Othmar Marti, and Franz Pfeiffer. Influence of the overlap parameter on the convergence of the ptychographical iterative engine. *Ultramicroscopy*, 108(5):481–487, 2008.

[58] A. M. Maiden, M. J. Humphry, M. C. Sarahan, B. Kraus, and J. M. Rodenburg. An annealing algorithm to correct positioning errors in ptychography. *Ultramicroscopy*, 120:64–72, 2012.

[59] Pierre Thibault and Andreas Menzel. Reconstructing state mixtures from diffraction measurements. *Nature*, 494(7435):68–71, 2013.

[60] Louis de Broglie. XXXV. A tentative theory of light quanta. *The London, Edinburgh, and Dublin Philosophical Magazine and Journal of Science*, 47(278):446–458, 1924.

[61] Bin Li, Haiqian Wang, Jinlong Yang, and J. G. Hou. High-resolution scanning tunneling microscopy for molecules. *Ultramicroscopy*, 98(2-4):317–334, 1 2004.

[62] M Bellini, C Lyngå, A Tozzi, M B Gaarde, T W Hänsch, A L'huillier, and C.-G Wahlström. Temporal Coherence of Ultrashort High-Order Harmonic Pulses. Technical report, 1998.

[63] C. Lyngå, M. B. Gaarde, C. Delfin, M. Bellini, T. W. Hänsch, A. L' Huillier, and C. G. Wahlström. Temporal coherence of high-order harmonics. *Physical Review A - Atomic, Molecular, and Optical Physics*, 60(6):4823–4830, 1999.

[64] Pierre Thibault, Martin Dierolf, Oliver Bunk, Andreas Menzel, and Franz Pfeiffer. Probe retrieval in ptychographic coherent diffractive imaging. *Ultramicroscopy*, 109(4):338–343, 3 2009.

[65] Manuel Guizar-Sicairos and James R. Fienup. Phase retrieval with transverse translation diversity: a nonlinear optimization approach. *Optics Express*, 16(10):7264, 2008.

[66] Darren J. Batey, Daniel Claus, and John M. Rodenburg. Information multiplexing in ptychography. *Ultramicroscopy*, 138:13–21, 3 2014.

[67] Manuel Guizar-Sicairos, Mirko Holler, Ana Diaz, Joan Vila-Comamala, Oliver Bunk, and Andreas Menzel. Role of the illumination spatial-frequency spectrum for ptychography. *Physical Review B - Condensed Matter and Materials Physics*, 86(10), 2012.

[68] Michal Odstrčil, Maxime Lebugle, Manuel Guizar-Sicairos, Christian David, and Mirko Holler. Towards optimized illumination for high-resolution ptychography. *Optics Express*, 27(10):14981, 5 2019.

[69] Jun Yu Ou, Eric Plum, Jianfa Zhang, and Nikolay I. Zheludev. Giant Nonlinearity of an Optically Reconfigurable Plasmonic Metamaterial. *Advanced Materials*, 28(4):729–733, 2016.

[70] Matthew D. Seaberg, Daniel E. Adams, Ethan L. Townsend, Daisy A. Raymondson, William F. Schlotter, Yanwei Liu, Carmen S. Menoni, Lu Rong, Chien-Chun Chen, Jianwei Miao, Henry C. Kapteyn, and Margaret M. Murnane. Ultrahigh 22 nm resolution coherent diffractive imaging using a desktop 13 nm high harmonic source. *Optics Express*, 19(23):22470, 2011.

[71] Przemyslaw W Wachulak, Andrzej Bartnik, and Henryk Fiedorowicz. Sub-70 nm resolution tabletop microscopy at 13.8 nm using a compact laser-plasma EUV source. *Opt. Lett.*, 35(14):2337–2339, 7 2010.

[72] M Van Heel, W Keegstra, W Schutter, and EJF Van Bruggen. Arthropod hemocyanin structures studied by image analysis, 1982.

[73] W O Saxton and W Baumeister. The correlation averaging of a regularly arranged bacterial cell envelope protein. *Journal of Microscopy*, 127(2):127–138, 1982.

[74] George Harauz, Lisa Borland, Gunter F. Bahr, Elmar Zeitler, and Marin van Heel. Three-dimensional reconstruction of a human metaphase chromosome from electron micrographs. *Chromosoma*, 95(5):366–374, 1987.

[75] Marin Van Heel and Michael Schatz. Fourier shell correlation threshold criteria. *Journal of Structural Biology*, 151(3):250–262, 2005.

[76] Sami Koho, Giorgio Tortarolo, Marco Castello, Takahiro Deguchi, Alberto Diaspro, and Giuseppe Vicidomini. Fourier ring correlation simplifies image restoration in fluorescence microscopy. *Nature Communications*, 10(1), 2019.

[77] Elisabeth Gasteiger, Alexandre Gattiker, Christine Hoogland, Ivan Ivanyi, Ron D Appel, and Amos Bairoch. ExPASy: the proteomics server for in-depth protein knowledge and analysis. *Nucleic Acids Research*, 31(13):3784–3788, 2003.

[78] M. R. Howells, T. Beetz, H. N. Chapman, C. Cui, J. M. Holton, C. J. Jacobsen, J. Kirz, E. Lima, S. Marchesini, H. Miao, D. Sayre, D. A. Shapiro, J. C.H. Spence, and D. Starodub. An assessment of the resolution limitation due to radiation-damage in X-ray diffraction microscopy. *Journal of Electron Spectroscopy and Related Phenomena*, 170(1-3):4–12, 3 2009.

[79] R Henderson, J M Baldwin, T A Ceska, F Zemlin, E Beckmann, and K H Downing. Model for the structure of bacteriorhodopsin based on high-resolution electron cryo-microscopy. *Journal of Molecular Biology*, 213(4):899–929, 1990.

[80] Elspeth F Garman and Martin Weik. X-ray radiation damage to biological samples: recent progress. *Journal of Synchrotron Radiation*, 26(4):907–911, 7 2019.

[81] Lindsay A. Baker and John L. Rubinstein. *Radiation damage in electron cryomicroscopy*, volume 481. Elsevier Masson SAS, 2010.

[82] Henry N. Chapman, Carl Caleman, and Nicusor Timneanu. Diffraction before destruction. *Philosophical Transactions of the Royal Society B: Biological Sciences*, 369(1647), 2014.

[83] Karol Nass. Radiation damage in protein crystallography at X-ray free-electron lasers. *Acta Crystallographica Section D*, 75(2):211–218, 2 2019.

[84] M. D. Shirk and P. A. Molian. A review of ultrashort pulsed laser ablation of materials. *Journal of Laser Applications*, 10(1):18, 6 1998.

[85] Anthony W.P. Fitzpatrick, Benjamin Falcon, Shaoda He, Alexey G. Murzin, Garib Murshudov, Holly J. Garringer, R. Anthony Crowther, Bernardino Ghetti, Michel Goedert, and Sjors H.W. Scheres. Cryo-EM structures of tau filaments from Alzheimer's disease. *Nature*, 547(7662):185–190, 7 2017.

[86] Benjamin Falcon, Wenjuan Zhang, Alexey G Murzin, Garib Murshudov, Holly J Garringer, Ruben Vidal, R Anthony Crowther, Bernardino Ghetti, Sjors H W Scheres, and Michel Goedert. Structures of filaments from Pick's disease reveal a novel tau protein fold. *Nature*, 561(7721):137–140, 2018.

[87] Benjamin Falcon, Jasenko Zivanov, Wenjuan Zhang, Alexey G Murzin, Holly J Garringer, Ruben Vidal, R Anthony Crowther, Kathy L Newell, Bernardino Ghetti, Michel Goedert, and Sjors H W Scheres. Novel tau filament fold in chronic traumatic encephalopathy encloses hydrophobic molecules. *Nature*, 568(7752):420–423, 2019.

[88] Grace I. Hallinan, Mariana Vargas-Caballero, Jonathan West, and Katrin Deinhardt. Tau Misfolding Efficiently Propagates between Individual Intact Hippocampal Neurons. *The Journal of neuroscience : the official journal of the Society for Neuroscience*, 39(48):9623–9632, 11 2019.

[89] J. Tate, T. Auguste, H. G. Muller, P. Salières, P. Agostini, and L. F. Dimauro. Scaling of wave-packet dynamics in an intense midinfrared Field. *Physical Review Letters*, 98(1):1–4, 2007.

[90] A. D. Shiner, C. Trallero-Herrero, N. Kajumba, H. C. Bandulet, D. Comtois, F. Légaré, M. Giguère, J. C. Kieffer, P. B. Corkum, and D. M. Villeneuve. Wavelength scaling of high harmonic generation efficiency. *Physical Review Letters*, 103(7):1–4, 2009.